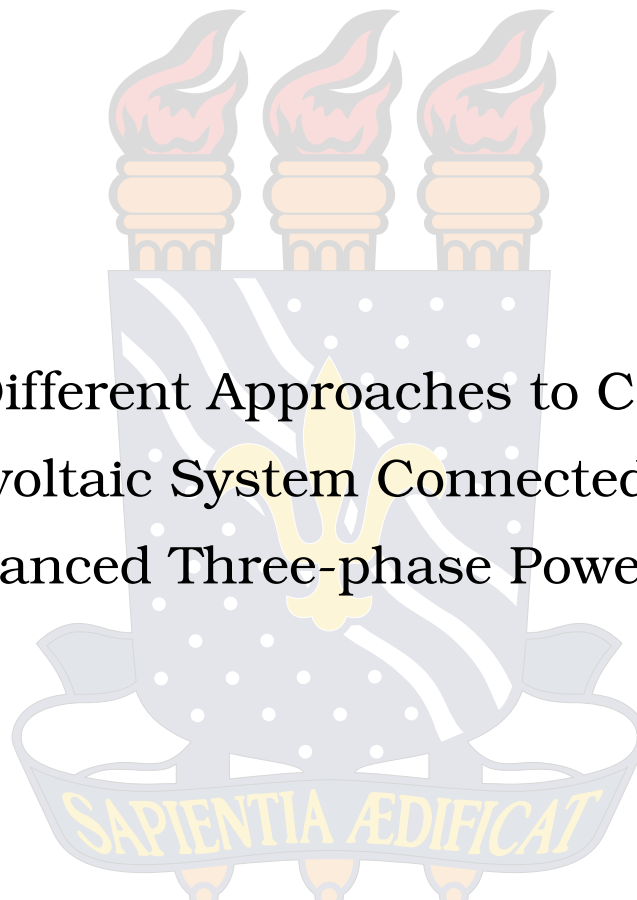# FEDERAL UNIVERSITY OF PARAIBA
CENTER FOR ALTERNATIVE AND RENEWABLE ENERGY
GRADUATE PROGRAM IN ELECTRICAL ENGINEERING

Master Thesis

Three Different Approaches to Control a Photovoltaic System Connected to an Unbalanced Three-phase Power Grid

Lamarck Alves da Cunha

João Pessoa, Brazil

January 2023

Lamarck Alves da Cunha

THREE DIFFERENT APROACHES TO CONTROL A PHOTOVOLTAIC SYSTEM CONNECTED TO AN UNBALANCED THREE-PHASE POWER GRID

Thesis presented to the Graduate Program in Electrical Engineering, from the Federal University of Paraíba, as a partial requirement to obtain the master's degree in Electrical Engineering.

Advisor: Prof. Nady Rocha, Dr.
Co-advisor: Prof. Rogério Gaspar de Almeida, Dr.

João Pessoa, Brazil

January 2023

UNIVERSIDADE FEDERAL DA PARAÍBA – UFPB

CENTRO DE ENERGIAS ALTERNATIVAS E RENOVÁVEIS – CEAR

PROGRAMA DE PÓS-GRADUAÇÃO EM ENGENHARIA ELÉTRICA – PPGEE

A Comissão Examinadora, abaixo assinada, aprova a Dissertação

**THREE DIFFERENT APPROACHES TO CONTROL A PHOTOVOLTAIC SYSTEM
CONNECTED TO AN UNBALANCED POWER GRID**
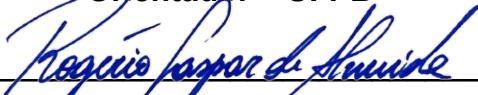
Elaborada por

LAMARCK ALVES DA CUNHA

como requisito parcial para obtenção do grau de

Mestre em Engenharia Elétrica.

COMISSÃO EXAMINADORA

_____

PROF. DR. NADY ROCHA
Orientador – UFPB

_____

PROF. DR. ROGÉRIO GASPAR DE ALMEIDA
Coorientador – UFPB

_____

PROF. DR. FABIANO SALVADORI
Examinador Interno – UFPB

_____

PROF. DR. FELIPE VIGOLVINO LOPES
Examinador Externo – UFPB

João Pessoa/PB, 23 de novembro de 2022

RESUMO

Este trabalho aborda sobre controle para um sistema fotovoltaico com inversor trifásico conectado à rede elétrica trifásica desbalanceada. São propostas três estratégias de controle alicerçadas no Referencial Síncrono Duplo, que se utiliza de duas estruturas capazes de controlar de forma independente as componentes positivas e negativas da corrente que é injetada na rede pelo sistema fotovoltaico. Cada uma das estratégias tenta atuar em uma grandeza elétrica, melhorando alguma característica destas, sendo que a estratégia 1 objetiva a eliminação da componente de sequência negativa da corrente, as estratégias 2 e 3 objetivam a mitigação das oscilações das potências ativa e reativa, respectivamente. As simulações foram realizadas com uma rede elétrica composta por 7 barras utilizando o software de simulação Matlab/Simulink®, onde foram analisados e avaliados os desempenhos das três estratégias. A rede encontra-se desequilibrada devido a distribuição irregular de cargas entre suas fases, além de que foi considerado afundamentos de tensão oriundos de faltas elétricas. Foram apresentados os resultados das simulações, com os quais foi possível observar e comparar os desempenhos dos controles na atenuação dos desequilíbrios das correntes e oscilações nas potências ativa e reativa. Além disso, foi realizada uma comparação entre as estratégias utilizando dois índices, sendo esses o fator de desequilíbrio das tensões da rede e as perdas elétricas na linha. Através da análise dos resultados desses índices foi determinado que a estratégia 2 diminui os desequilíbrios de tensão na barra, e as perdas são menores quando a estratégia 3 é aplicada ao sistema FV.

Palavras-chave: DSRF, Sistema Fotovoltaico, Controle de inversor trifásico, Rede elétrica desequilibrada.

ABSTRACT

This work deals with control for a photovoltaic (PV) system with a three phase inverter connected to an unbalanced three phase electrical grid. Three control strategies are proposed based on the Double Synchronous Referential, which uses two structures capable of independently controlling the positive and negative components of the current injected into the grid by the PV system. Each one of the strategies tries to act on an electrical quantity, improving some characteristics of these. Thus, strategy 1 targets eliminate the negative sequence symmetrical components of the current, and strategies 2 and 3 aim to mitigate the oscillations of active and reactive powers, respectively. The simulation model is a power grid composed of 7 buses, which is executed using Matlab/Simulink® as the simulation software, where the performance of the three strategies is analyzed and evaluated. The grid is unbalanced due to the uneven distribution of loads between its phases, and its primary voltages are determined by voltage sags arising from electrical faults. The results of the simulations are presented, making it possible to observe and compare the performances of the controls in attenuating the current unbalances and oscillations in active and reactive power. Besides, a comparison is made between the strategies using two indices: the unbalance factor of the grid voltages and the electrical line losses. Through the analysis of the results of these indices, it was determined that strategy 2 reduces voltage unbalances in the grid voltages, and losses are lower when strategy 3 is applied to the PV system.

Keywords: DSRF, Photovoltaic system, Three phase inverter control, Unbalanced power grid.

LIST OF FIGURES

LIST OF TABLES

1 INTRODUCTION

1.1 PHOTOVOLTAIC SOLAR ENERGY

Environment-friendly energy sources are at the center of the attention of technological development research because of their great potential to reduce aggression to the environment. Consequently, these sources are increasing their role in electric energy generation, focusing on solar and wind energy. Besides, this increase in the use of green sources makes it necessary to study the impacts of the insertion of these sources in the utility grid (AAMRI et al., 2015; ELAVARASAN et al., 2019; KUCEVIC et al., 2020; YANG et al., 2014).

Solar energy is indirectly responsible for giving rise to other energy sources, such as wind, hydraulic, fossil fuels etc. Also, this energy can be straightly used to heat spaces and fluids, and for electric energy generation, which can be done by the photovoltaic (PV) or thermoelectric effect (BRASIL, 2008).

Modern PV technology had its first steps in the mid-19th century when the French scientist Edmond Becquerel immersing metallic plates in an electrolytic solution, noticed that a difference of eletric potential appeared when they were exposed to some light source. At that time, the first report of the PV effect came out, and it can be considered as the first step towards what it is known today as PV cells that use this effect to generate electricity directly from sunlight (VALLÊRA; BRITO, 2006).

The first PV cell was officially presented to the world in the annual meeting of the National Academy of Science that took place in Washington, 1954. However, the cost only allows applying the technology in some particular areas at that time, such as space applications. The first major investment was made precisely during the space race in the 1960s, which had the United States and the Soviet Union as the main participants. Back then, the PV cells became a fundamental power source to satellites, because of the power to weight ratio. Besides, another massive investment occurred in the 1973 oil crisis, which encouraged the great nations to finance researches to reduce the cells' price. Some relevant innovations emerged from the financial support, such as the application of multicrystalline silicon in the cells' construction (VALLÊRA; BRITO, 2006; MUKUND, 1999; GREEN, 2005; PERLIN, 2004).

The financing continues even with the overcoming of the oil crisis, mainly due to the concern about environmental degradation and climate changes caused by man's actions. The '90s were led by the growing concern for the environment and it was during this time that some barriers related to PV cell technology were broken. For instance, in 1997, the 20% efficiency mark for multicrystalline silicon PV cells was surpassed, in addition to breaking the 24.7% efficiency record the following year for monocrystalline cells (VALLÊRA; BRITO,

2006; GREEN, 2005). Nevertheless, several marks have been overpassed through time with the constant investment in research in the PV area, mainly motivated by the need to diversify the energy matrix as well as the issues of environmental preservation. To demonstrate this fact, a team at the National Renewable Energy Laboratory (NREL) in 2020 achieved the 47.1% efficiency mark of a multijunction PV cell tested with concentrated lighting, which is capable of reaching a 50% mark according to the researchers.

An atom structure incorporates a positively charged nucleus composed of protons and neutrons, and this nucleus is surrounded in different layers by electrons, which have a negative charge. Also, there is a positively charged particle for every negative charge in the nucleus, which makes the atom electrically neutral. The electrons present in the valence band, which is the outermost shell of the atom, are the ones that have the large facility to leave it, as the electrostatic attraction force is smaller than other layers because they are further away from the nucleus and have higher energy. Thus, it only takes a small amount of energy to make these electrons free, thus creating a conduction band, making them able to move through the material. These free electrons produce the electrical current, as shown in Figure 1.1 (MARQUES; CRUZ; JÚNIOR, 2012).
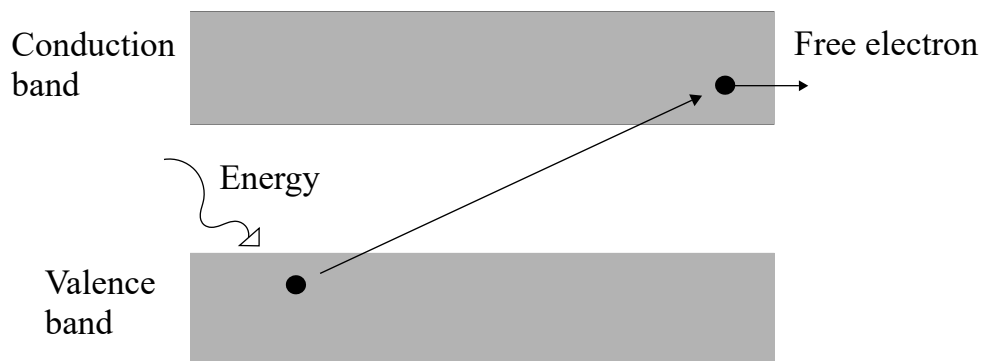
Figure 1.1 – Free electrons, valence and conduction bands (Source: Adapted from (MARQUES; CRUZ; JÚNIOR, 2012))

There is a band gap between the conduction and valence bands where the electrons can not stay, which is responsible for the material's electric characteristics. Semiconductor materials lie between conductors and insulators as they have a small energy gap, so their valence electrons need to perform a small energy jump. However, they require more energy than the electrons of conductive materials, which have virtually no bandpass. On the other hand, insulators have a long distance between the valence and conduction bands, preventing their electrons from performing an energy jump (MARQUES; CRUZ; JÚNIOR, 2012). Thus, a consequence of electron migration from one band to other is the appearance of a hole that gives rise to a meaningful term known as electron-hole pair.

Silicon is an example of a semiconductor whose initial characteristics doesn't allow sunlight into electrical energy conversion, even so, is the most used element in the manufacture of PV cells. This semiconductor element does not have electrons free and has

only four electrons in its last energetic shell. Thus, one way to make this material capable of producing electrical current is through doping, which consists of adding impurities to the material, inducing a process of covalent bonding of the pure semiconductor to the adulterating element. When the bond is performed with a pentavalent element, such as phosphorus, the N-type element will appear, which will have an excess of electrons with a negative charge, whereas it is made with a trivalent element, such as boron, the P-type element will rise and carry excess positively charged holes. Besides, it is through these two doped elements that the PN junction is created, whose duty is producing an internal electric field in charge of consolidating the PV effect (MARQUES; CRUZ; JÚNIOR, 2012; Villalva; Gazoli; Filho, 2009; SEDRA; SMITH, 2015; MALVINO; BATES, 2016). Figure 1.2 shows the PN junction configuration.
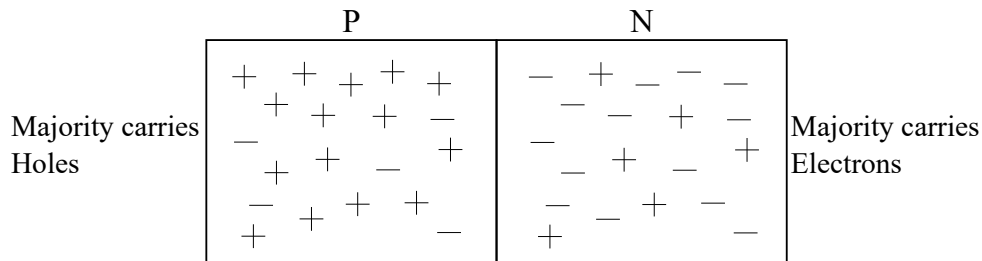
Figure 1.2 – PN junction (Source: Adapted from (MARQUES; CRUZ; JÚNIOR, 2012))

The following phenomenon occurs at the PN junction and, hence, as well as at the PV cell which can be taken as a PN diode: the N-type doped region has an excess of electrons while the P-type region lacks electrons, so when these two regions are connected, the electrons are attracted and occupy the place of the holes, thus giving rise to two diffusion currents, responsible for carrying a large amount of charge from one side of the junction to the other, and as a consequence, there is an accumulation of electrons in the P region and a reduction in the N region. These shifted charges create a potential barrier in the transition region, called the depletion region. Finally, the equilibrium state happens when the electric field formed is strong enough to prevent the traffic of remaining free electrons in the N channel. Nevertheless, the balance is undone at the light presence, such as solar, once the energy of the light photons causes a charge motion at the PN junction, thus resulting in a potential and electrical current, and typifying the PV effect (MARQUES; CRUZ; JÚNIOR, 2012; MALVINO; BATES, 2016).

Figure 1.3 shows the structure of a PV cell, whose function is directly converting solar radiation into electrical energy thanks to the PV effect. In addition, construction is based on semiconductor materials (mainly silicon).

Silicon cells represent about 80% to 90% of the world market, but other materials can be used in the manufacture of cells and, therefore, have different applications, efficiencies, costs, etc. Therefore, PV cells can be classified according to their generation, which takes into account, among other things, the maturity of the technology employed (CHOUBEY;
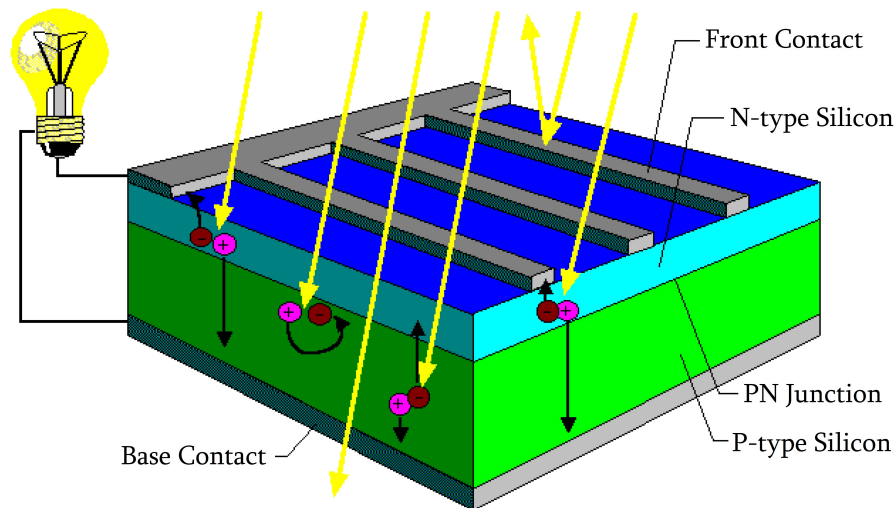
Figure 1.3 – PV cell structure (Source: (SOLAR, 2006))

OUDHIA; DEWANGAN, 2012; PINHO; GALDINO et al., 2014; SAMPAIO; GONZÁLEZ, 2017; BAGHER; VAHID; MOHSEN, 2015).

Starting with the first generation silicon-based cells which are the most popular because of their high efficiency despite the relatively high cost, and are also the oldest. Within this category of silicon wafer-based cells, there are two subgroups, one formed by monocrystalline silicon (m-Si) and the other by polycrystalline (p-Si) (CHOUBEY; OUDHIA; DEWANGAN, 2012; PINHO; GALDINO et al., 2014; SAMPAIO; GONZÁLEZ, 2017; BAGHER; VAHID; MOHSEN, 2015). The differences between the two categories start with the production process, in which polycrystalline silicon has an advantage for having a simpler and cheaper process, but it loses when it comes to efficiency, which can reach 23%. The m-Si cells can reach an efficiency of 26% (NREL, 2022).

The second generation contains thin-film cells, which have greater structural flexibility than the first generation thus allowing its application in various areas, such as solar tiles manufacturing, but it lacks efficiency. The most common elements used in this technology are amorphous silicon, cadmium telluride, in addition to Copper-Indium-Selenide (CIS) and Copper-Indium-Gallium-Diselenide (CIGS) (CHOUBEY; OUDHIA; DEWANGAN, 2012; PINHO; GALDINO et al., 2014; SAMPAIO; GONZÁLEZ, 2017; BAGHER; VAHID; MOHSEN, 2015).

On the other hand, the third generation has the rawest technologies, as they are still in earlier stages when compared to the ones before it, but some show great potential. This generation is characterized by having multijunction and concentration cells, dye-sensitized solar cell (DSSC) and organic PVs (OPV) (PINHO; GALDINO et al., 2014; SAMPAIO; GONZÁLEZ, 2017; BAGHER; VAHID; MOHSEN, 2015).

PV cells have capacity disadvantages due to their small size, producing low voltages ranging from 0.5 V to 1.5 V, despite the ability to convert solar energy into electrical

energy. Therefore, the association in parallel or series of these cells is necessary to obtain a higher voltage or current, since most applications require high values of this electrical quantity. Figure 1.4 shows the cell's association in parallel and series, which result in the sum of the cells' currents and voltages, respectively. Also, the entire set is called a PV module (ZILLES et al., 2012).
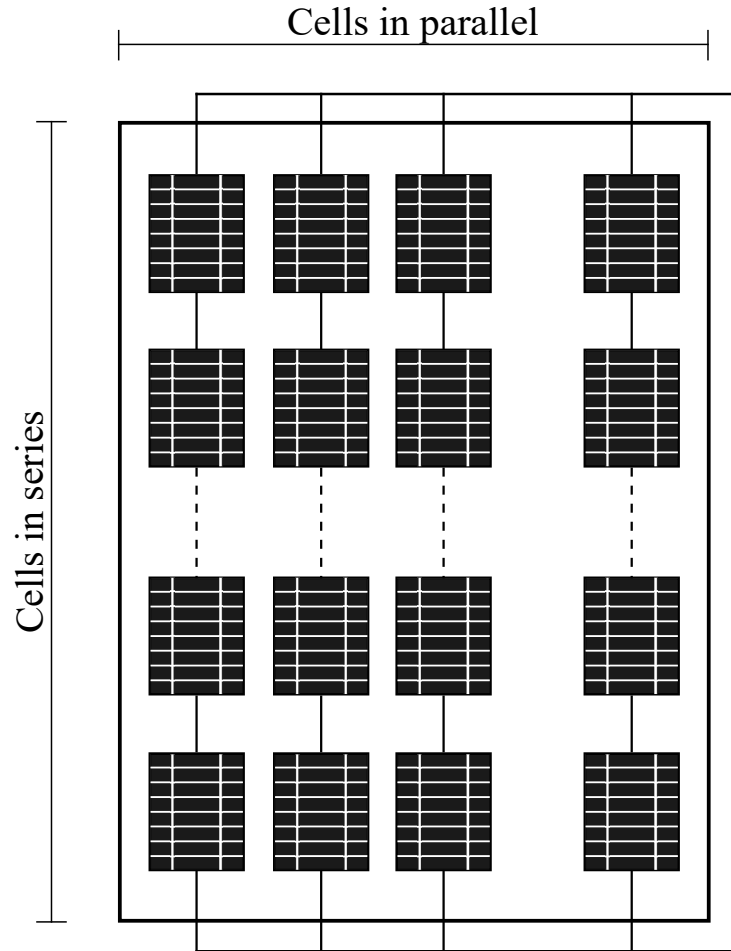
Figure 1.4 – Parallel and series cell's association (Source: Adapted from (ZILLES et al., 2012))

In addition to enabling the association of cells, the PV module has the function of protecting these cells against weather, electrically insulating them from external contacts, and providing mechanical rigidity. In Figure 1.5, an example of a PV module based on crystalline silicon cells can be seen, in which the encapsulation consists of an aluminum frame to provide resistance to the assembly, and inside there is a tempered glass of high transparency, ethyl vinyl acetate (EVA) stabilized for ultraviolet radiation, PV cells, stabilized EVA, and an insulating backsheet (PINHO; GALDINO et al., 2014).

1.1.1 PV systems

According to (PINHO; GALDINO et al., 2014), PV systems can be classified as isolated and connected to the electricity grid. Furthermore, such systems can operate alone or in conjunction with other energy sources, such as wind, in which case they are called
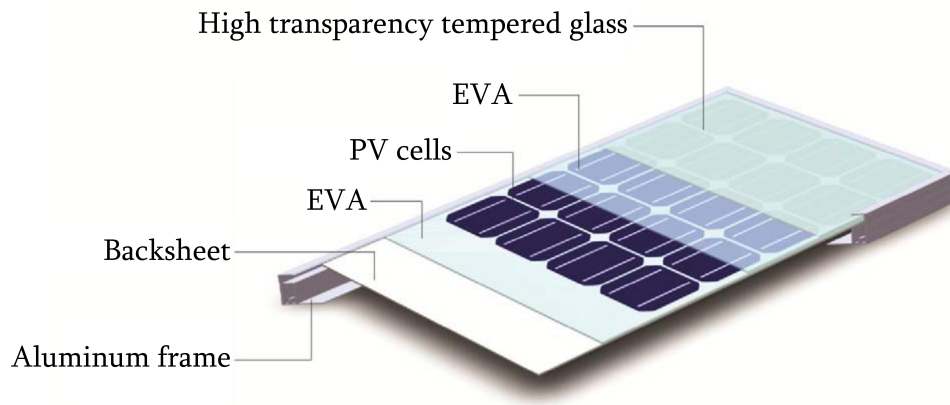
Figure 1.5 – PV module configuration (Source: (PINHO; GALDINO et al., 2014))

hybrid systems. The use of each of these systems varies depending on the application required. For example, isolated systems are more suitable for remote areas without access to the electricity grid, despite the need to use an energy storage system, such as a battery bank, for times when the PV system is not generating. Hybrid systems also fit this usage profile, but their control is much more complex.

There are some similarities between the mentioned systems, mainly regarding their composition, as some components are used in both. In these systems, there will be the action of an inverter, which is responsible for converting the constant amount of power in alternating power, if the loads or the grid operate with alternating energy (the frequency in Brazil is 60 Hz). Also, this equipment has high efficiency, maintaining the optimized operating point (PINHO; GALDINO et al., 2014; MUKUND, 1999).

Off-grid or autonomous systems are characterized by not being connected to the electricity grid. Thus, the use of batteries might be necessary, as they will be responsible for storing the energy generated to supply the consumer load. This system is either applied in individual loads or microgrids (PINHO; GALDINO et al., 2014). Microgrids are small-scale systems and are more flexible than individually serviced power systems as they are monitored and operated by software. In addition, these micro-grids can integrate sources based on renewable and conventional energies, loads, and batteries (LIU; WANG; LOH, 2011; KATIRAEI; IRAVANI; LEHN, 2005). Figure 1.6 shows an individual off-grid PV system.

The system in Figure 1.6 is composed of a PV power source, a charge controller that is responsible for controlling the energy accumulated in the storage system (batteries), thus preventing it from being improperly discharged or charged, a DC-AC Converter or Inverter that transform Direct Current (DC) input into Alternating Current (AC) output, and loads.

The base of a PV system connected to the grid (on-grid) is composed of PV panels and a DC-AC (direct current-alternating current) inverter, which is responsible for
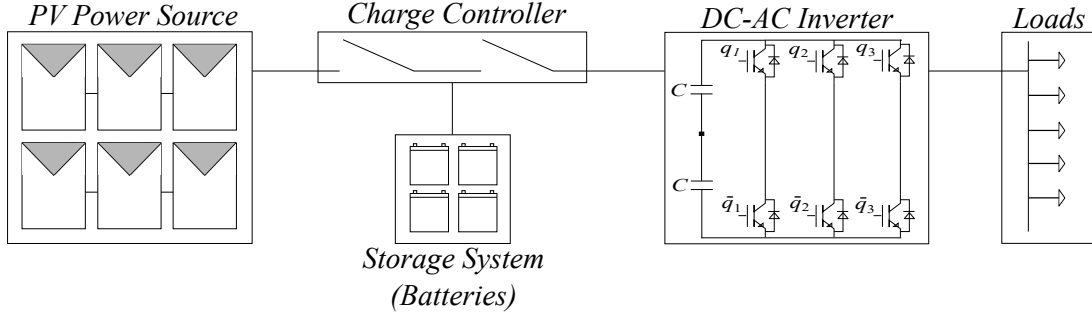
Figure 1.6 – Off-grid PV system diagram

converting the DC power generated by the panels into AC power. However, due to the intermittent nature of solar energy, which influences the performance of panels because of the shading and the influence of temperature (ZAPATA et al., 2019; CHOI et al., 2015), a DC-DC stage is necessary to apply a Maximum Power Point Tracking (MPPT) technique, to stabilize the input voltage and extract the maximum power from the PV system (JAIN; SINGH, 2017; KOURO et al., 2010). In addition, there is the need for this DC-DC stage even for large-scale applications, and some DC-AC inverters for specific power ranges (up to $20kW_p$) already have integrated this stage (CHOI et al., 2015; ZAPATA et al., 2019). An example of a PV system connected to the grid utility is shown in Figure 1.7.
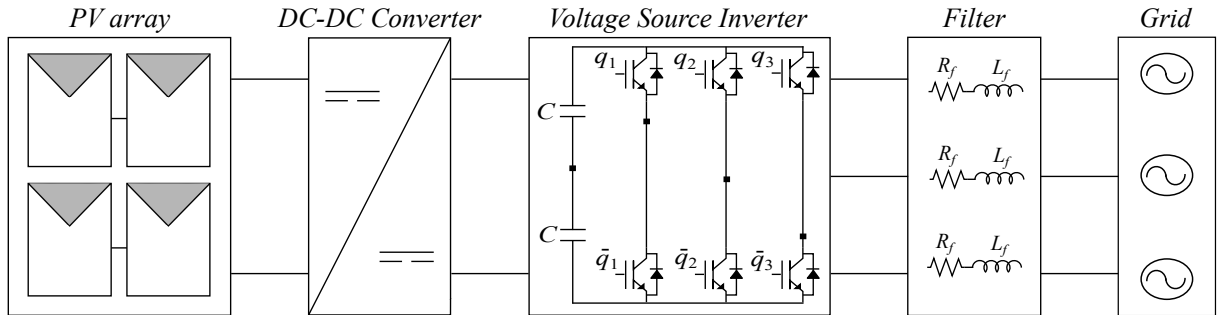
Figure 1.7 – Scheme of the studied system

In Brazil, the electric energy compensation model for on-grid PV systems was introduced by the National Electric Energy Agency (ANEEL) through the Normative Resolution (NR) N°482 of 2012 and updated with the NR N°687 of 2015. This model suggests a generation of credits for consumer units connected to the distribution network. Credits are obtained through the injection of excess electrical energy not consumed by the consumer units, which might be applied to offset the energy consumed from the utility grid in periods when PV generation is not enough to meet the demand. Furthermore, these credits are valid for up to 5 years.

1.1.2 PV energy panorama

In the last decades, there has been a considerable increase in investments in renewable energy driven by the need to diversify electricity generation and the decrease in

environmental degradation caused by traditional generation based on fossil fuelsthat still being the principal global source. In 1990, the PV source represented only 0.00076% of the world's electrical matrix, as it was during that time that this technology would still develop. However, there was a huge leap in the contribution of this source in 2019, which came to represent 2.52% of electricity generation in the world with about 680.952 TWh, as shown in Figure 1.8 whose graph represents the world electricity matrix in the year of 2019.
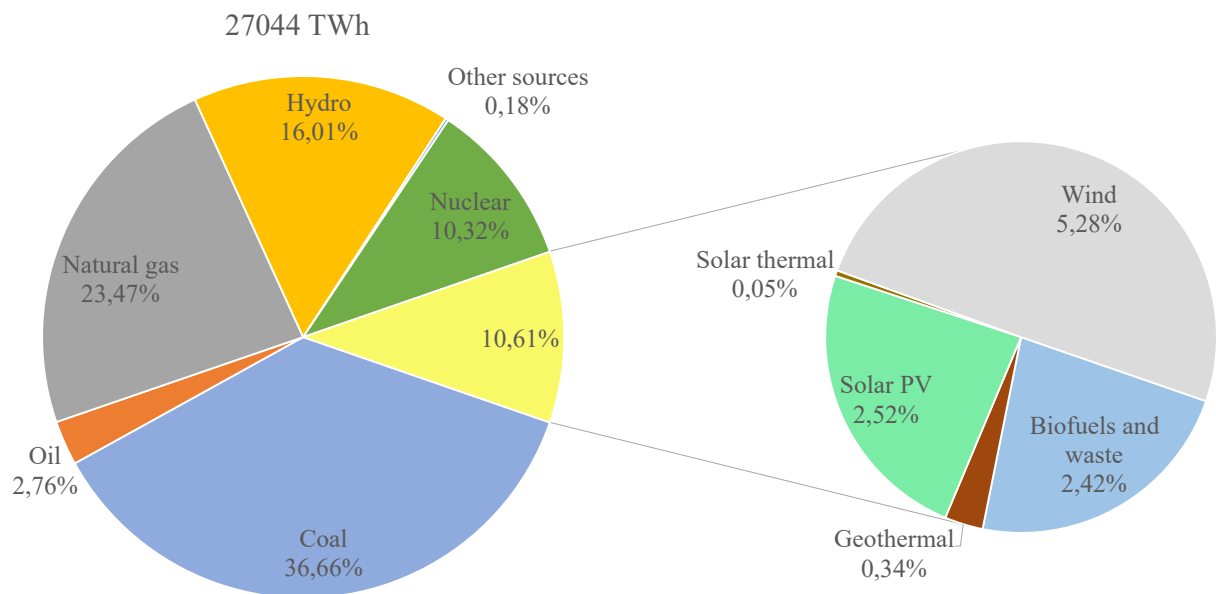
Figure 1.8 – World electricity matrix in 2019 (Source: (AGENCY, 2022))

Among the forms of renewable sources, solar energy has the greatest potential. PV generation is one of the most efficient ways to use the energy from the sun. In addition to being a clean source of energy, PVs promote an increase in the reliability of the electrical service provided and have the possibility of being used in remote areas (CHOWDHURY; SAWAB, 1996; JIA et al., 2020; HACHIM; DAHLIOUI; BARHDADI, 2018).

The installed capacity of PV systems is the fastest growing among renewable energies. And this is a relevant fact that indicates the worldwide concern to diversify the electrical matrix, which makes the electrical system more reliable and electrical generation less harmful to the environment. Figure 1.9 shows the installed capacity and additions per year for PV systems from 2011 to 2021, implying a boost from 70 GW to 942 GW, thus, an increase of 13.45 times in the installed capacity of PV systems. Also, there is a tendency to increase capacity year by year, as shown in the graphs, highlighting the last year of 2021, which showed a 24% jump. Furthermore, all continents played a considerable role in increasing installed capacity, and some countries already have a significant contribution from PV systems in their electricity matrixes, such as Honduras with 10.7%, Italy with

8.6%, Greece with 8.3%, Germany with 8.2% and Chile with 8.1%.
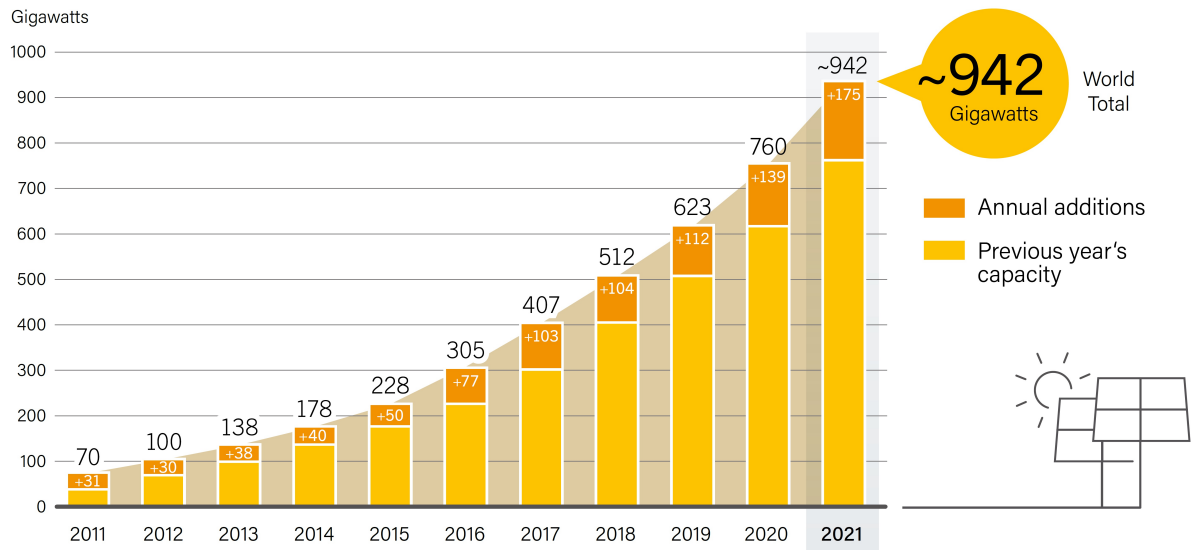
Figure 1.9 – PV installed capacity worldwide and annual additions (Source: (REN21, 2020))

Brazil has an essentially renewable electricity matrix, with hydro as the main one that corresponds to 55.3% of internal supply (Figure 1.10). Besides, renewable sources are responsible for 76.8% of the total supply, making the country one of the world leaders in this segment. At first, these data point to a good situation in Brazil regarding its electricity generation, which is largely renewable. On the other hand, they also indicate to a country that usually bases its generation on just one primary source, water, which in turn is subject to climatic variations, being greatly affected by the scarcity of rain, which reduces the generation capacity of hydroelectric plants. As a consequence of this reduction, it is necessary to activate thermoelectric plants, which, in addition to promoting an increase in energy tariffs, cause an increase in environmental pollution, because they require the burning of fuels to start operating (SILVEIRA et al., 2018). Therefore, it is necessary to focus on the use of other renewable energy sources, such as solar and wind energies, particularly the former, as it has the greatest potential.

Daily, the Sun provides enough energy to the Earth's atmosphere to supply the entire planet 10,000 times, making it an inexhaustible alternative energy source (CRESESB, 2008). This source has enormous potential for use, being able to impact not only environmentally, but also socially, serving the various communities that are isolated and deprived of electricity feeding, through the installation of PV systems. Proof of this is the federal project Luz Para Todos, which already uses this technology and aims to bring electricity to rural, needy, and isolated communities (GOMES, 2012).

Much of the Brazilian territory takes place near the equator, which makes Brazil a privileged country, given that this proximity causes minor variation in solar duration throughout the day (ANEEL). In addition, Brazil stands out for having a high annual
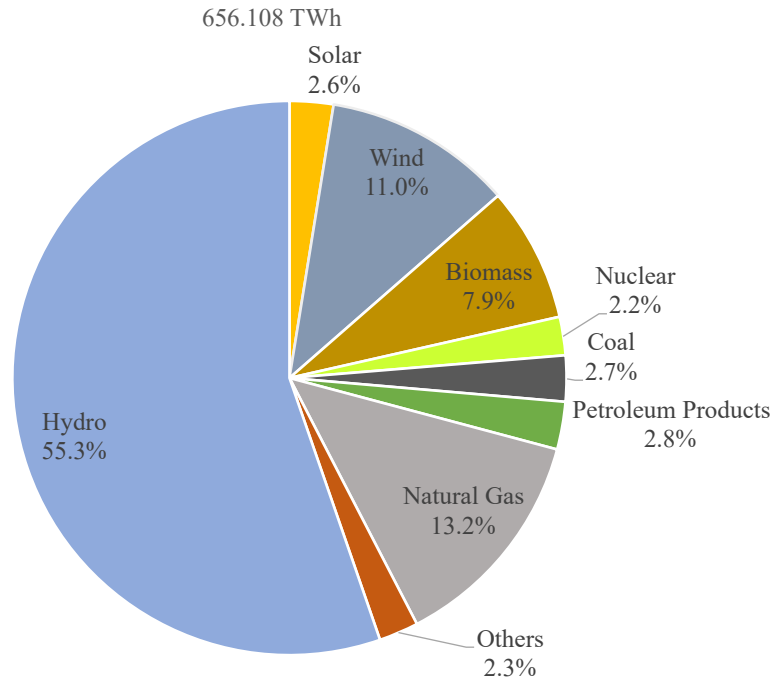
Figure 1.10 – Brazil electricity matrix in 2021 (Source: (EPE, 2022))

average of global irradiation, which presents good uniformity, with relatively high averages throughout the Canarian territory. Germany, Spain, Italy, Portugal, and France have one of the most consolidated PV technology but have lower rates than Brazil, whose solar irradiation in any region lies within $1,500$-$2,500\,\mathrm{Wh/m^2}$ (MARTINS et al., 2017).

The still small use of solar technology in Brazil becomes even less justifiable when the favorable conditions for the growth of this source in the country are verified. According to EPE (2012), in addition to having high levels of solar irradiance, the Brazilian nation has substantial reserves of quality quartz. This commodity is fundamental to guarantee a competitive advantage concerning high-purity silicon production and, hence, cells and solar modules that are high-added value devices. Thus, a massive investment is needed, mainly in high technology industries, to explore these natural reserves and contribute to the dissemination of PV systems in the country and its consequent sustainable development.

1.2 THE POWER GRID

The electricity grid in Brazil is divided into generation, transmission, and distribution. As the name suggests, the first is the initial part of the entire electrical energy cycle, where the conversion of some form of energy supply (hydro, wind, solar, etc.) to electrical energy takes place. Transmission is responsible for transporting electricity between generating plants and distribution, the latter being responsible for bringing electricity to the final consumer.

According to (ABRADEE, 2021), the electricity distribution grid is mixed with

the topography of cities, intending to physically connect the transmission system, or even medium and small generating units, to the final electricity consumers. The connections of distributed generations occur in this system, including PV solar systems.

Distribution grids are significant for the electrical system as they usually provide power to the final users. One way to classify these grids is through their operating voltage levels as follows: low voltage grids if they operate with values up to 1 kV; medium voltage with operating values between 1 kV and 69 kV; or high voltage if their operating range comprises 69 kV and 230 kV.

Low and medium voltage systems are easy to observe on streets and avenues throughout cities, constantly composed of overhead wires supported by wooden backing on concrete poles, with low voltage wires located at a height lower than the medium voltage wires. Although they are located in the same structure, it is the low voltage grid that reaches homes and small businesses/industries, with voltages that can vary between 110 and 440 V. However, medium-sized companies tend to use medium grid voltage as the energy supplier, and these companies are responsible for converting voltage levels to lower values, and this is necessary because most equipment that requires electrical energy works with low voltages (ABRADEE, 2021).

The distribution grids have their origin in the so-called distribution substations that give rise to another classification, in which these grids can be called primary or secondary. The primary distribution grids include those that operate at medium voltage, for example, this voltage is 13.8 kV in the State of Paraíba in Brazil. In this way, step-down transformers are equipment responsible for lowering the voltage of the primary grids, and from them originate the secondary grids, whose voltage operation is 380 V in Paraíba. Also, this voltage is ideal for small consumers of electricity and they are called the end-users.

1.2.1 Balanced Power grid

Electric power systems are supplied by three-phase generators, which are normally composed of a rotating magnet (known as rotor) surrounded by a fixed winding (called a stator). Three coils with three pairs of terminals (called 1-1', 2-2', and 3-3') are attached in this stator with a physical separation of 120°. According to the rotation of the rotor, its magnetic field "cuts" the flux of the three coils, which causes the appearance of induced voltages in them. These voltages (Figure 1.11) have identical magnitudes, but as the coils present a separation of 120°, they will also manifest this phase shift (ALEXANDER; SADIKU, 2013).

The voltages in Figure 1.11, V_{1n}, V_{2n}, and V_{3n} are called phase voltages, as they represent the voltage between lines 1, 2, and 3 and the grid neutral. Thus, if the sources have the same amplitude, frequency, and 120°phase shift, the voltages are said to be balanced (NAHVI; EDMINISTER, 2014).
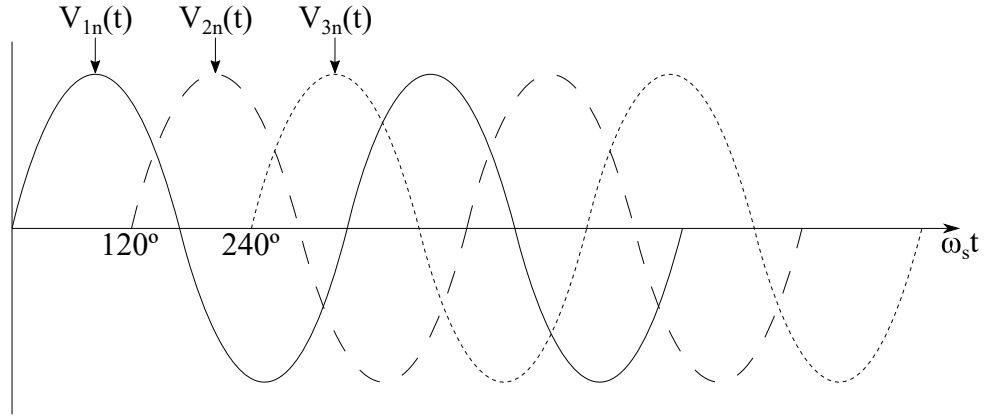
Figure 1.11 – Induced voltages with 120°of phase shift (Source: Adapted from (ALEXANDER; SADIKU, 2013))

Due to this phase shift, there are two possible scenarios. The first refers to the 123 sequence or positive sequence, in which the voltage V_{1n} peaks first, followed by the voltage V_{2n} and, finally, V_{3n}. This sequence can be expressed mathematically as

$$V_{1n} = E_p sin(\omega_s t - \phi) \tag{1.1}$$

$$V_{2n} = E_p sin(\omega_s t - \phi - 120°) \tag{1.2}$$

$$V_{3n} = E_p sin(\omega_s t - \phi + 120°) \tag{1.3}$$

where E_p is peak value, ω_s is the angular frequency related to the grid frequency by $\omega_s = 2\pi f_s$, t is the time and ϕ is the initial angular phase.

The second scenario occurs when the voltage V_{3n} is ahead of V_{2n}, which, in turn, is ahead of V_{1n}. This is the so-called 132 sequence or negative sequence, which can be expressed mathematically as

$$V_{1n} = E_p sin(\omega_s t - \phi) \tag{1.4}$$

$$V_{3n} = E_p sin(\omega_s t - \phi - 120°) \tag{1.5}$$

$$V_{2n} = E_p sin(\omega_s t - \phi + 120°) \tag{1.6}$$

In addition to voltage sources, a typical three-phase electrical system consists of loads connected by three or four wires, or transmission lines. So, for total balance between the phases to occur, these loads must also balanced each other, i.e., they must present the same impedance in magnitude and phase.

1.2.2 Unbalanced power grid

The three-phase grid is said to be unbalanced when the voltages or currents of its phases have different magnitudes from each other or do not have a 120º phase shift, while the causes may vary according to the system topology and the load connected on it (PEREIRA, 2015).

Electrical systems are also subject to several types of faults, including: single-phase (line-to-ground), two-phase (line-to-line or line-line-to-ground) and three-phase (three-phase-to-ground), which lead to different types of voltage drop, that is, to grid unbalance (BOLLEN; OLGUIN; MARTINS, 2005).

The work of (BOLLEN; ZHANG, 2003) shows a classification to represent seven types of voltage sags, called A, B, C, D, E, F, and G, which are related to different faults in the electrical grid. Their complex expressions of the phase voltages are shown in Table 1.1. $\vec{V}$ represents the voltage during the fault, and $\vec{E}$ represents the complex pre-fault voltage.

Table 1.1 – Seven types of voltage sags caused by faults

Type	$\mathbf{V_1}$	$\mathbf{V_2}$	$\mathbf{V_3}$
A	$\vec{V}$	$-\frac{1}{2}\vec{V} - j\sqrt{3}\frac{1}{2}\vec{V}$	$-\frac{1}{2}\vec{V} + j\sqrt{3}\frac{1}{2}\vec{V}$
B	$\vec{V}$	$-\frac{1}{2}\vec{E} - j\sqrt{3}\frac{1}{2}\vec{E}$	$-\frac{1}{2}\vec{E} + j\sqrt{3}\frac{1}{2}\vec{E}$
C	$\vec{E}$	$-\frac{1}{2}\vec{V} - j\sqrt{3}\frac{1}{2}\vec{E}$	$-\frac{1}{2}\vec{V} + j\sqrt{3}\frac{1}{2}\vec{E}$
D	$\vec{V}$	$-\frac{1}{2}\vec{E} - j\sqrt{3}\frac{1}{2}\vec{V}$	$-\frac{1}{2}\vec{E} + j\sqrt{3}\frac{1}{2}\vec{V}$
E	$\vec{E}$	$-\frac{1}{2}\vec{V} - j\sqrt{3}\frac{1}{2}\vec{V}$	$-\frac{1}{2}\vec{V} + j\sqrt{3}\frac{1}{2}\vec{V}$
F	$\vec{V}$	$-\frac{1}{2}\vec{V} - j\sqrt{3}(\frac{1}{3}\vec{E} + \frac{1}{6}\vec{V})$	$-\frac{1}{2}\vec{V} + j\sqrt{3}(\frac{1}{3}\vec{E} + \frac{1}{6}\vec{V})$
G	$\frac{2}{3}\vec{E} + \frac{1}{3}\vec{V}$	$-\frac{1}{3}\vec{E} - \frac{1}{6}\vec{V} - j\sqrt{3}\frac{1}{2}\vec{V}$	$-\frac{1}{3}\vec{E} - \frac{1}{6}\vec{V} + j\sqrt{3}\frac{1}{2}\vec{V}$

The consequences of operating with an unbalanced three-phase grid can manifest in different ways, especially through the inadequate performance of systems and equipment, resulting, for example, in service blackout, and through the degradation of the power used in the conversion of electromechanical processes. Therefore, unbalances directly affect the operating costs of electrical systems and electronic equipment, being capable of causing extensive financial losses due to equipment burning, increased losses, and service stops. Electric motors are the first equipment to feel the electrical grid unbalances, due to their sensitivity to the negative sequence component of the current that arises with the unbalance. The application of unbalanced phase voltages at the terminals of a three-phase motor gives rise to the emergence of additional negative sequence currents in the motor, increasing temperature and, therefore, an increase in losses (TEODORO, 2005; BIRICIK et al., 2019; ANWARI; HIENDRO, 2010).

1.2.3   Symmetrical components

According to Fortescue's theorem, any unbalanced three-phase phasors of a three-phase system can be decomposed into three symmetrical phasor systems. The sets of components are (STEVENSON and GRAINGER, 1994):

- Positive sequence components: consists of three phasors that have the same magnitude, with an angular shift of 120° to each other, and have the same phase sequence as the original phasors;

- Negative sequence components: they are three phasors that have the same magnitude, are 120° out of phase between each other, and have a phase sequence opposite to that of the original phasors;

- Zero sequence components: includes three phasors that have the same magnitude and do not have a phase shift between them.

The symmetrical components of a generic unbalanced three-phase system are shown in Figure 1.12.
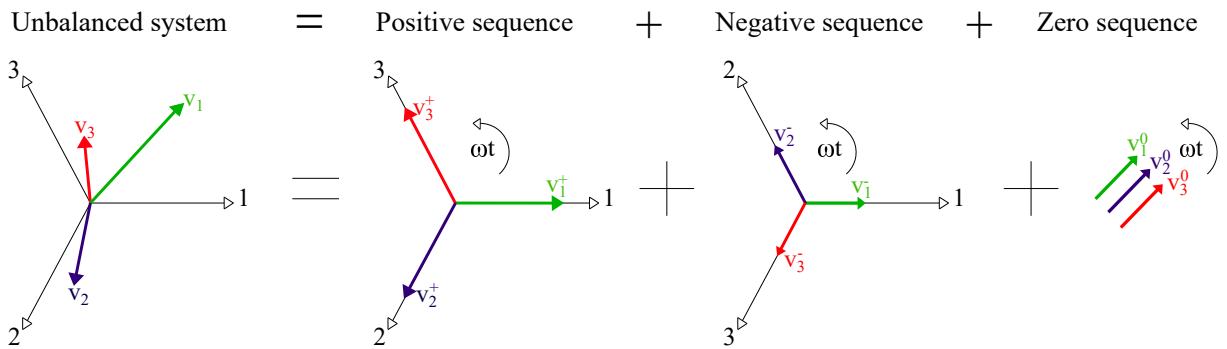
Figure 1.12 – Symmetrical components of an unbalanced three-phase system (Source: Adapted from (ALEXANDER; SADIKU, 2013))

One way to represent the symmetrical components (voltage, current) of an unbalanced three-phase system is expressed in equation (1.7), as follows

$$v_{123} = \begin{bmatrix} v_1 \\ v_2 \\ v_3 \end{bmatrix} = \sum_{n=1}^{\infty} = v_{123}^{+n} + v_{123}^{-n} + v_{123}^{0n} \qquad (1.7)$$

where $+n$, $-n$, and $0n$ represent, respectively, the positive, negative, and zero sequence components of the nth harmonic of the voltage phasor v. This work takes into account only the fundamental frequency (n=1), so the symmetrical components in this frequency received the following designations: V^+ for the positive, V^- for the negative, and V^0 for zero component. Current phasors are represented in the same way as voltages.

Since the original unbalanced phasors can be decompounded as the sum of their symmetrical components, as can be seen in equation (1.7), we will have the following expressions representing each phase at the fundamental frequency

$$v_1 = V_1^0 + V_1^+ + V_1^- \tag{1.8}$$

$$v_2 = V_2^0 + V_2^+ + V_2^- \tag{1.9}$$

$$v_3 = V_3^0 + V_3^+ + V_3^- \tag{1.10}$$

It is possible to arrive at a transformation relation through expressions 1, 2, and 3 with the aid of a transformation matrix designated here as [F]. This transformation permits obtaining the components in coordinate 123 from the symmetrical components and vice versa. Here is the relationship, in matrix form, based on Fortescue's theorem (STEVENSON and GRAINGER, 1994):

$$v_{123} = \begin{bmatrix} v_1 \\ v_2 \\ v_3 \end{bmatrix} = [F] \begin{bmatrix} V_1^0 \\ V_1^+ \\ V_1^- \end{bmatrix} \tag{1.11}$$

and the inverse transformation is

$$V_1^{0+-} = \begin{bmatrix} V_1^0 \\ V_1^+ \\ V_1^- \end{bmatrix} = [F]^{-1} \begin{bmatrix} v_1 \\ v_2 \\ v_3 \end{bmatrix} \tag{1.12}$$

where

$$[F] = \begin{bmatrix} 1 & 1 & 1 \\ 1 & \alpha^2 & \alpha \\ 1 & \alpha & \alpha^2 \end{bmatrix} \tag{1.13}$$

$$[F]^{-1} = \frac{1}{3} \begin{bmatrix} 1 & 1 & 1 \\ 1 & \alpha & \alpha^2 \\ 1 & \alpha^2 & \alpha \end{bmatrix} \tag{1.14}$$

and $\alpha = e^{j\frac{2\pi}{3}}$ or $1\angle 120°$ (magnitude and angular phase).

1.3 LITERATURE REVIEW

The ideal operation for the low voltage electrical grid would be with the three phases that compose it fully balanced, as this balance would guarantee better efficiency for the electrical system. However, this does not practically happen since the electrical grid presents unbalance arising from some reasons, like the unequal allocation of loads in the phases and electrical faults (CASTILLA et al., 2010; RODRíGUEZ et al., 2012). So,

this unbalance can lead to line losses and reduce the efficiency of the electrical system in general. In addition, it reduces the useful life of electrical equipment, such as electrical machines that suffer from torque oscillation and heating due to the appearance of negative sequence components of the current, which increase losses (BIRICIK et al., 2019; ANWARI; HIENDRO, 2010). Therefore, it is necessary to pay attention to how distributed generation systems, such as PVs, are inserted into the grid, using adequate control systems to ensure good quality power injection.

One of the components of the PV system studied is a three phase inverter for energy conversion, being the focus of control strategies that try to regulate the currents injected into the grid. In this way, in the literature, it is possible to find several techniques used in the control of voltage source inverters (VSI) connected to the grid, where two segments stand out: direct power control (DPC) and current control (FILHO et al., 2009).

The DPC segment is characterized by carrying out the control through the power directly, as its name suggests. It uses active and reactive powers as state variables, activating the converter switches to track the desired power signals (NOGUCHI et al., 1998). However, this definition is for the root technique, which presented issues, such as the changing frequency that makes it difficult to parameterize the output filter. In this sense, a solution was given by (MALINOWSKI; JASINSKI; KAZMIERKOWSKI, 2004), who applied spatial vector modulation together with the DPC, which made it possible to apply a fixed switching frequency, and the technique was named DPC-SVM.

Another method applied together with the DPC is the predictive model, which uses a system model to predict future actions of the control variables while depending on the desired goal, the future information obtained is used to designate the controller's action (OLIVEIRA, 2019). Furthermore, the predictive model acts by minimizing cost functions that characterize the desired behavior for the system under analysis. The work developed by (VAZQUEZ et al., 2017) demonstrates the most used models for this type of controller.

Many of the interconnections of the converters to the electrical grid have the characteristic that their control is generally formed by two cascade control loops, one external for the DC-link voltage control and the other internal for the current control. In this way, among the types of current control, the ones that use the dq control in the synchronous reference of the mains voltage and stationary stand out. The difference between them lies in the properties of the originated signals through Clarke's transformation, where the synchronous frame produces two constant signals and the stationary frame two oscillating signals. The application of PI-type controllers in the first one is possible, as they guarantee zero error in steady-state for DC signals. The second is not possible, as the PI ends up producing a non-zero error in the steady-state for oscillating signals (PARVEZ et al., 2016).

Another current control technique considered one of the easiest methods to apply is hysteresis current control. This control, in essence, does not require any PWM modulation approach once the switches states of the converter are determined through the error generated by the difference between the reference and the measured current. Then, this error is compared with a defined tolerance band of hysteresis (RAHIM; SELVARAJ; KRISMADINATA, 2007). On the other hand, the control underwent modifications over time to enhance its performance by combining it with other tools. Some works, such as those seen in (DAI; CHAO, 2009; MERAI et al., 2016; KANG; LIAW, 2001; SUUL et al., 2011), demonstrate few applications of this type of control. In addition, there are also works related to current control with the predictive control model, such as in (ZANCHETTA et al., 2011; RODRIGUEZ et al., 2004; KOURO et al., 2009).

A method widely used in control systems for the connection of distributed generation to the power grid is the Synchronous Reference Frame (SRF), commonly called *dq* frame (BLAABJERG et al., 2006), and called conventional strategy in this paper. Figure 1.13 shows the structure used in the SRF control strategy. However, this type of control does not work well in adverse grid situations, that is, in cases of the appearance of unbalances (TIMBUS et al., 2005). To fill this gap, the work in (SONG; NAM, 1999) presents the Double Synchronous Reference Frame (DSRF), which performs the control through the positive and negative sequence components of electrical quantities. In both cases, it is possible to use PI controllers, due to the use of the *dq* reference frame that transforms the alternating quantities into constants.
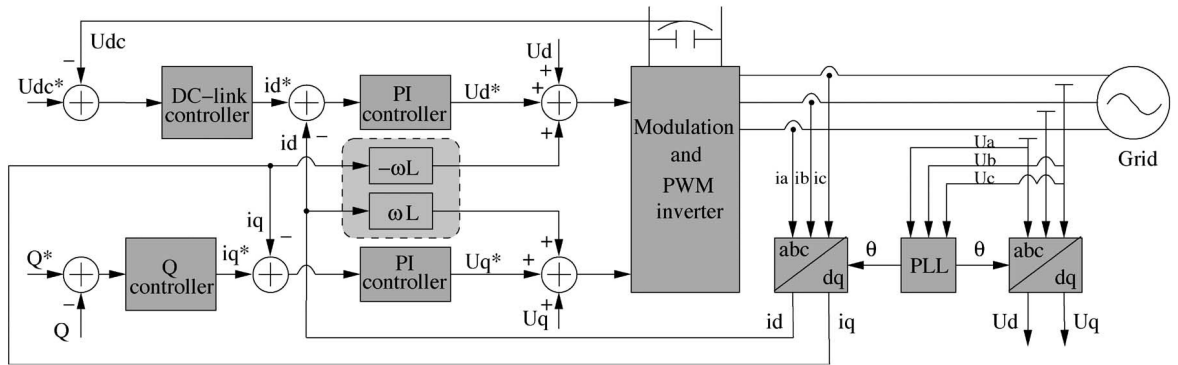
Figure 1.13 – Control structure of the SRF (Source: (BLAABJERG et al., 2006))

If the electrical grid is under unbalanced effects, the renewable energy sources connected to this grid can help reduce these abnormalities. With this in mind, some studies use the control technique based on DSRF (Double Synchronous Reference Frame) to regulate the negative and positive sequence components of the current injected by the inverter. Focusing on verifying the operation of the control technique, the author (Li-Jun et al., 2015) uses the DSRF structure and a DSOGI (Double Second Order Generalized Integrator) structure to eliminate active power oscillations. However, the work is limited to just this possibility of control, not taking into account the others, which would be the

elimination of reactive power oscillations and injection of balanced currents. Increasing the number of control strategies usage, (Günther; Bendrat; Sourkounis, 2019) performs a small comparison between the results of the electrical quantities of the grid and coupling inverter, also using the control strategy that tries to reduce the oscillations of reactive power, in addition to a strategy without DSRF. However, it also comes up against the limitation of control strategies usage, in addition to performing the simulations only for one fault scenario.

Furthermore, the ability of these renewable sources to help with voltage levels during a grid surge is shown in (Khan et al., 2017), especially in the case of low voltage. The author performs the analysis for different types of faults but focuses only on the application of DSRF to reduce active power oscillations. Similar to the previous work, (Lin et al., 2018) carries out studies on the use of a specific distributed generation system with a coupling inverter, the PV. The author makes simulations for different fault scenarios but focuses on eliminating the negative sequence components of the current that arise with unbalances caused by electrical faults. (WIJNHOVEN; DECONINCK, 2013) makes an analysis of several fault scenarios for a distributed generation system connected to the grid through an inverter using the DSRF structure but does not use any of the possible strategies. Other works using the DSRF scheme are seen in (SEN; SHARMA; BABU, 2012; Kandpal; Hussain; Singh, 2015; YU; HU, 2019).

In addition to active power injection, the distributed generation system (such as PV) can also be designed to perform auxiliary services, such as reactive power injection. This service is capable, among other things, of allowing the correction of the power factor at a desired point in the electrical grid. In addition, these auxiliary DG services help to reduce the impact on the electricity grid caused by the high insertion of DG itself and the natural growth of the electricity grid (HASHMI et al., 2020). In this sense, the control system in (KHAN et al., 2020) also aims to amortize the active power fluctuations of a PV system connected to the grid through the DSRF. Such analysis focuses on helping the power grid under low voltage due to some electrical faults. In addition, it also injects reactive power, which is a type of auxiliary service. Again, there is a lack of use of the other control strategies for comparison purposes.

Therefore, this work presents and compares three control approaches to control a PV system connected to the three-phase grid based on DSRF: elimination of the negative sequence component of the current, mitigation of oscillations in active power, and reactive power. The mathematical model of the system is presented, and the DSRF control is described. In addition, computer simulations are performed to validate the operation of each control strategy in a voltage unbalance scenario in the three-phase grid. Two voltage sags resulting from electrical faults are considered in the simulations, in addition to the unequal allocation of loads in the three phases of the grid. For comparison purposes,

two indices are taken to analyze the performance of the PV system running each of the strategies, being the line losses and the voltage unbalance factor.

Thus, the main contributions of the work are:

- Use of a 7-bus electrical grid that is closer to what is found materially;

- Application of the three control strategies to the PV system, which are: elimination of negative sequence components of the injected current, reduction of active and reactive power oscillations;

- PV system connection at different points in the grid to compare the effects of this system on the grid;

- Use of two indices to compare the control strategies applied to the PV system, which are line losses and grid voltage unbalances.

1.4 WORK ORGANIZATION

In addition to this Introduction chapter, this work has four other chapters divided into:

Chapter 2: System Model - this chapter presents the mathematical model of the studied system for a balanced and unbalanced power grid, including an analysis in the synchronous reference frame. Also, it shows the PV model and MPPT technique applied in the PV array.

Chapter 3: Control System - this chapter shows the build of the overall control structure adopted in this work, which includes the development of root equations for the control strategies based on the DSRF and the analysis of control loops.

Chapter 4: Simulation Results - in this chapter, simulations are performed to validate the proposed strategies for the PV system.

Chapter 5: Simplified Model - in this chapter, the simplified model is presented together with a line loss and unbalance factor analysis.

Chapter 6: Conclusions - in this chapter, the general conclusions, and proposals for the continuity of the work are presented.

2 SYSTEM MODEL

2.1 INTRODUCTION

In this Chapter, the mathematical model of the on-grid photovoltaic system and the development of the base for the control strategies will be presented. The foundation for these strategies came from a set of equations that relates voltages and currents through the PV system when it is inserted in an unbalanced three-phase grid, also taking into account the unbalance effects upon the active and reactive powers. Besides, the model of a PV module and the MPPT technique are shown.

2.2 ON-GRID PV SYSTEM MODEL

The PV system analyzed is shown in Figure 2.1 and it includes a PV array, DC-DC stage, inverter, filter inverter, and the three-phase power grid that is balanced for the first analysis.
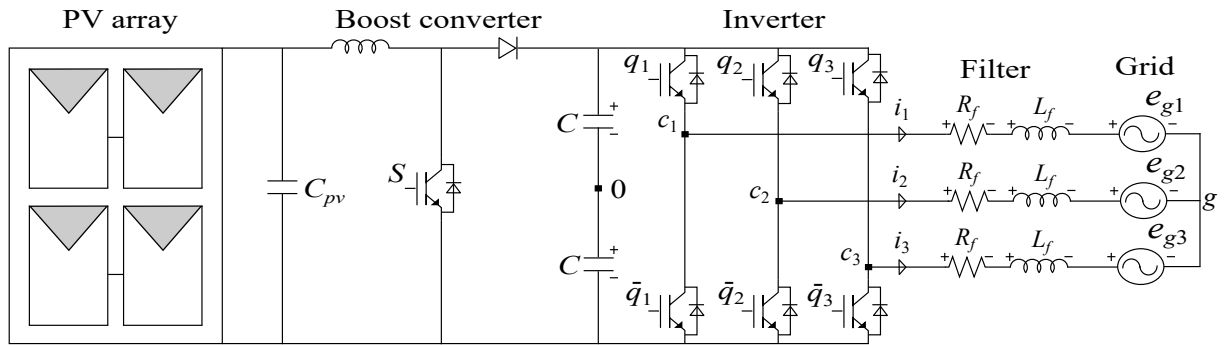
Figure 2.1 – Scheme of the studied system

Observing the AC side of the inverter in the Figure 2.1, that is, the grid side, and applying Kirchoff's Voltage Law (KVL), it obtain the following equations for the voltages

$$e_{g1} = v_{c10} - v_{g0} - i_1 R_f - L_f \frac{di_1}{dt} \tag{2.1}$$

$$e_{g2} = v_{c20} - v_{g0} - i_2 R_f - L_f \frac{di_2}{dt} \tag{2.2}$$

$$e_{g3} = v_{c30} - v_{g0} - i_3 R_f - L_f \frac{di_3}{dt} \tag{2.3}$$

where v_{c10}, v_{c20} and v_{c30} are the pole voltages, v_{g0} is the voltage between the middle point of the DC-link and the center point of the grid, i_1, i_2 and i_3 are the currents injected by the inverter into the grid, L_f is the filter inductance and R_f would be its resistance.

Furthermore, the following simplification is made

$$v_{c1} = v_{c10} - v_{g0} \tag{2.4}$$

$$v_{c2} = v_{c20} - v_{g0} \tag{2.5}$$

$$v_{c3} = v_{c30} - v_{g0} \tag{2.6}$$

Now, replacing the expressions (2.4), (2.5), and (2.6) in (2.1), (2.2), and (2.3), the voltage expressions are given by

$$e_{g1} = v_{c1} - i_1 R_f - L_f \frac{di_1}{dt} \tag{2.7}$$

$$e_{g2} = v_{c2} - i_2 R_f - L_f \frac{di_2}{dt} \tag{2.8}$$

$$e_{g3} = v_{c3} - i_3 R_f - L_f \frac{di_3}{dt} \tag{2.9}$$

Finally, these voltage expressions can be written in matrix form, as follows

$$\overline{e}_{g123} = \overline{v}_{c123} - \overline{i}_{123} \overline{R}_f - \overline{L}_f \frac{d\overline{i}_{123}}{dt} \tag{2.10}$$

where the dash over quantities represents matrix form.

2.2.1 $dq0$ model

It is known that any electrical quantity in the natural reference 123 can be written in $dq0$ coordinates through the Park's transformation, and this is an essential tool since the control system in this work is based on the dq synchronous reference frame. This transformation simplifies the control, which now regulates only two constant quantities, and enables the use of PI controllers that guarantee zero steady-state error for constant quantities. This way, the relation between an electrical quantity in $dq0$ and 123 reference frame is given by

$$\overline{x}_{dq0}^g = \overline{P}^g \overline{x}_{123} \tag{2.11}$$

where the $\overline{x}_{123} = [x_1 \ x_2 \ x_3]^T$ and $\overline{x}_{dq0} = [x_0 \ x_d \ x_q]^T$ are the vectors for the 123 and $dq0$ variables, respectively; the g superscript is for generic reference; and $\overline{P}^g$ is the matrix used to perform the Park's transformation and whose expression is

$$\overline{P}^g = \sqrt{\frac{2}{3}} \begin{bmatrix} \cos(\delta_g) & \cos(\delta_g - \frac{2\pi}{3}) & \cos(\delta_g - \frac{4\pi}{3}) \\ -\sin(\delta_g) & -\sin(\delta_g - \frac{2\pi}{3}) & -\sin(\delta_g - \frac{4\pi}{3}) \\ \frac{1}{\sqrt{2}} & \frac{1}{\sqrt{2}} & \frac{1}{\sqrt{2}} \end{bmatrix} \tag{2.12}$$

where δ_g is the initial angle.

An important property of the P_g matrix must be highlighted that it is orthogonal, thus implying equality between its inverse and transposed matrix.

Multiplying both sides of the expression (2.10) by (2.12) results in

$$\overline{P}^g \overline{e}_{g123} = \overline{P}^g \overline{v}_{c123} - \overline{P}^g \overline{i}_{123} \overline{R}_f - \overline{P}^g \overline{L}_f \frac{d\overline{i}_{123}}{dt} \tag{2.13}$$

The identity matrix has necessary properties, and some are used here. The first is the multiplication of a matrix by the identity matrix of the same order culminates in the multiplied matrix itself. And the other is the multiplication of a matrix by its inverse results in the identity matrix. Thus, applying these two properties in expression (2.13), the following expression appears

$$\overline{P}^g \overline{e}_{g123} = \overline{P}^g \overline{P}^{g^{-1}} \overline{P}^g \overline{v}_{c123} - \overline{P}^g \overline{R}_f \overline{P}^{g^{-1}} \overline{P}^g \overline{i}_{123} - \overline{P}^g \overline{L}_f \frac{d\overline{P}^{g^{-1}} \overline{P}^g \overline{i}_{123}}{dt} \quad \rightarrow$$

$$\overline{e}_{gdq0}^g = \overline{v}_{cdq0}^g - \overline{i}_{dq0}^g \overline{R}_f - \overline{P}^g \overline{L}_f \frac{d\overline{P}^{g^{-1}} \overline{i}_{dq0}^g}{dt} \tag{2.14}$$

Applying the derivative multiplication property in the expression (2.14) gives the following result

$$\overline{e}_{gdq0}^g = \overline{v}_{cdq0}^g - \overline{i}_{dq0}^g \overline{R}_f - \overline{P}^g \overline{L}_f \frac{d\overline{P}^{g^{-1}}}{dt} \overline{i}_{dq0}^g - \overline{P}^g \overline{P}^{g^{-1}} \overline{L}_f \frac{d\overline{i}_{dq0}^g}{dt} \quad \rightarrow$$

$$\overline{e}_{gdq0}^g = \overline{v}_{cdq0}^g - \overline{i}_{dq0}^g \overline{R}_f - \overline{L}_f \overline{P}^g \frac{d\overline{P}^{g^{-1}}}{dt} \overline{i}_{dq0}^g - \overline{L}_f \frac{d\overline{i}_{dq0}^g}{dt} \tag{2.15}$$

Now, looking deeply into expression (2.15), it is possible to perform a manipulation on a specific multiplication term to simplify the expression, as follows

$$\overline{P}^g \frac{d\overline{P}^{g^{-1}}}{dt} = \begin{bmatrix} 0 & 0 & 0 \\ 0 & 0 & -\frac{d\delta_g}{dt} \\ 0 & \frac{d\delta_g}{dt} & 0 \end{bmatrix} = \begin{bmatrix} 0 & 0 & 0 \\ 0 & 0 & -\omega_g \\ 0 & \omega_g & 0 \end{bmatrix} = \overline{\omega}_g \tag{2.16}$$

Replacing the expression (2.16) in (2.15), the result is

$$\overline{e}_{gdq0}^g = \overline{v}_{cdq0}^g - \overline{i}_{dq0}^g \overline{R}_f - \overline{L}_f \overline{\omega}_g \overline{i}_{dq0}^g - \overline{L}_f \frac{d\overline{i}_{dq0}^g}{dt} \tag{2.17}$$

where ω_g is the angular frequency.

When expanding the matrix expression (2.17), the result obtained is

$$\begin{bmatrix} e_{g0} \\ e_{gd} \\ e_{gq} \end{bmatrix} = \begin{bmatrix} v_{c0} \\ v_{cd} \\ v_{cq} \end{bmatrix} - \begin{bmatrix} R_f & 0 & 0 \\ 0 & R_f & 0 \\ 0 & 0 & R_f \end{bmatrix} \begin{bmatrix} i_0 \\ i_d \\ i_q \end{bmatrix} - \begin{bmatrix} L_f & 0 & 0 \\ 0 & L_f & 0 \\ 0 & 0 & L_f \end{bmatrix} \begin{bmatrix} 0 & 0 & 0 \\ 0 & 0 & -\omega_g \\ 0 & \omega_g & 0 \end{bmatrix} \begin{bmatrix} i_0 \\ i_d \\ i_q \end{bmatrix}$$

$$- \begin{bmatrix} L_f & 0 & 0 \\ 0 & L_f & 0 \\ 0 & 0 & L_f \end{bmatrix} \frac{d}{dt} \begin{bmatrix} i_0 \\ i_d \\ i_q \end{bmatrix} \rightarrow$$

$$\begin{bmatrix} e_{g0} \\ e_{gd} \\ e_{gq} \end{bmatrix} = \begin{bmatrix} v_{c0} \\ v_{cd} \\ v_{cq} \end{bmatrix} - \begin{bmatrix} R_f & 0 & 0 \\ 0 & R_f & -\omega_g L_f \\ 0 & \omega_g L_f & R_f \end{bmatrix} \begin{bmatrix} i_0 \\ i_d \\ i_q \end{bmatrix} - \begin{bmatrix} L_f & 0 & 0 \\ 0 & L_f & 0 \\ 0 & 0 & L_f \end{bmatrix} \frac{d}{dt} \begin{bmatrix} i_0 \\ i_d \\ i_q \end{bmatrix} \quad (2.18)$$

The expression for homopolar symmetric component of the voltage can be extracted from the result achieved in (2.18), as follows

$$e_{g0}^g = v_{c0}^g - R_f i_0^g - L_f \frac{di_0^g}{dt} \quad (2.19)$$

Taking into account that a three-wire system is being used, the homopolar component expressed by (2.19) will be null. In addition, the matrix expression given by (2.18) will be reduced to

$$\begin{bmatrix} e_{gd}^g \\ e_{gq}^g \end{bmatrix} = \begin{bmatrix} v_{cd}^g \\ v_{cq}^g \end{bmatrix} - \begin{bmatrix} R_f & -\omega_g L_f \\ \omega_g L_f & R_f \end{bmatrix} \begin{bmatrix} i_d^g \\ i_q^g \end{bmatrix} - \begin{bmatrix} L_f & 0 \\ 0 & L_f \end{bmatrix} \frac{d}{dt} \begin{bmatrix} i_d^g \\ i_q^g \end{bmatrix} \quad (2.20)$$

And finally, the voltage expressions in the dq coordinates in the generic frame will be given by

$$e_{gd}^g = v_{cd}^g - R_f i_d^g + \omega_g L_f i_q^g - L_f \frac{di_d^g}{dt} \quad (2.21)$$

$$e_{gq}^g = v_{cq}^g - R_f i_q^g - \omega_g L_f i_d^g - L_f \frac{di_q^g}{dt} \quad (2.22)$$

The quantities studied so far can be written in vector form, according to the following rule

$$\vec{x}^g = \frac{1}{\sqrt{2}} (x_d^g + j x_q^g) \quad (2.23)$$

Hence, the voltage expressions in (2.21) and (2.22) can be written as follows

$$e_{gd}^g + j e_{gq}^g = \vec{e}_g^g = \vec{v}_c^g - R_f \vec{i}^g - j\omega_g L_f \vec{i}^g - L_f \frac{d\vec{i}^g}{dt} \quad (2.24)$$

From now on, the reference frames will be changed to grid voltage frequency and the stationary frames. In the voltage synchronous reference frame, the axis d is aligned with axis 1 of the voltage, which implies that the frequency ω_g becomes the grid frequency ω_s, and the index g is substituted by e. Therefore, the expression (2.24) becomes

$$\vec{e}_g^e = \vec{v}_c^e - R_f \vec{i}^e - j\omega_s L_f \vec{i}^e - L_f \frac{d\vec{i}^e}{dt} \quad (2.25)$$

The same procedure can be done in the stationary reference frame dq_s, where the d axis aligns with the stationary axis, making δ_g and ω_g null. Furthermore, by replacing the index g with s, the expression (2.24) now can be written as follows

$$\vec{e}_g^s = \vec{v}_c^s - R_f\vec{i}^s - L_f\frac{d\vec{i}^s}{dt} \tag{2.26}$$

Starting now for power analysis on the AC side, it is known that the complex power can be expressed as a function of voltage and current in the stationary frame (NILSSON; RIEDEL, 2008), as follows

$$S_{AC} = 2\vec{e}_g^s\vec{i}^{s*} \tag{2.27}$$

where S_{AC} is the complex power, and the superscript $*$ indicates the complex conjugate of the quantity.

Using the vector form given by expression (2.23), the complex power (2.27) can be rewritten as a fuction of the voltage and current conjugate

$$S_{AC} = 2\frac{1}{\sqrt{2}}(e_d^s + je_q^s)\frac{1}{\sqrt{2}}(i_d^s - ji_q^s) = (e_d^s + je_q^s)(i_d^s - ji_q^s) \ \rightarrow$$

$$S_{AC} = e_d^si_d^s - je_d^si_q^s + je_q^si_d^s + e_q^si_q^s \ \rightarrow$$

$$S_{AC} = (e_d^si_d^s + e_q^si_q^s) + j(e_q^si_d^s - e_d^si_q^s) \tag{2.28}$$

It is known that the complex power S_{AC} is the vector sum of the active power and reactive power, whose expression is

$$S_{AC} = P_{AC} + jQ_{AC} \tag{2.29}$$

Comparing the expression (2.29) with (2.28), it is possible to obtain the following relations for active and reactive power

$$P_{AC} = e_d^si_d^s + e_q^si_q^s \tag{2.30}$$

$$Q_{AC} = -e_d^si_q^s + e_q^si_d^s \tag{2.31}$$

2.2.2 Model with unbalance

Unbalances among the phases of three-phase three-wire systems give rise to the positive and negative sequence components of current and voltage, thus implying the need for an analysis of the system when such a situation occurs.

Considering expression (2.24) and symmetrical negative component of the electrical quantities that appear in the presence of unbalances, it is possible to write the voltage expression in the synchronous reference frame of the grid voltage as shown below

$$e_g^{e+} = v_c^{e+} - R_fi^{e+} - j\omega_sL_fi^{e+} - L_f\frac{di^{e+}}{dt}, \tag{2.32}$$

$$e_g^{e-} = v_c^{e-} - R_f i^{e-} + j\omega_s L_f i^{e-} - L_f \frac{d i^{e-}}{dt} \tag{2.33}$$

where the "+" and "−" superscript signals represent the positive and negative sequence, respectively.

Now, the stationary reference frame will be used because a quantity in this reference can be expressed as a sum of its symmetrical components, hence

$$x_g^s = x_g^{s+} + x_g^{s-} \tag{2.34}$$

The analysis is being carried out on the positive and negative axis of the reference frames. That said, a quantity in the positive synchronous frame can be decomposed into a sum of the *dq* components in the stationary frame. Figure 2.2 shows the mentioned axis relation.
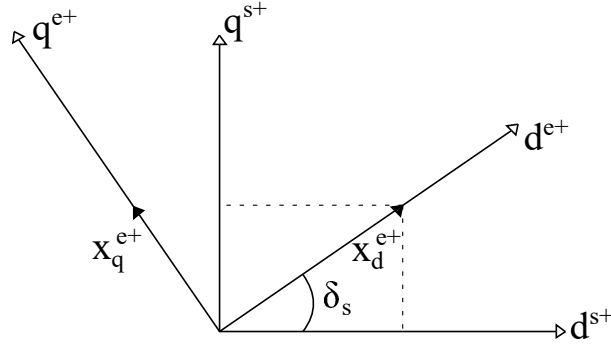
Figure 2.2 – Synchronous and Stationary axis of positive sequence

From Figure 2.2, it can be seen that the generic quantity in the synchronous frame of axis positive *d* can be written as follow

$$x_d^{e+} = x_d^{s+} \cos(\delta_s) + x_q^{s+} \sin(\delta_s) \tag{2.35}$$

and the *q* sychronous positive component is

$$x_q^{e+} = x_q^{s+} \cos(\delta_s) - x_d^{s+} \sin(\delta_s) \tag{2.36}$$

The same vector form will be used to write the positive components, as shown below

$$x_g^{e+} = \frac{1}{\sqrt{2}}(x_d^{e+} + j x_q^{e+}) \tag{2.37}$$

Replacing expressions (2.35) and (2.36) in (2.37), the result is

$$x_g^{e+} = \frac{1}{\sqrt{2}}[x_d^{s+} \cos(\delta_s) + x_q^{s+} \sin(\delta_s) + j x_q^{s+} \cos(\delta_s) - j x_d^{s+} \sin(\delta_s)] \;\rightarrow$$

$$x_g^{e+} = \frac{1}{\sqrt{2}}\{(x_d^{s+} + j x_q^{s+})\,[\cos(\delta_s) - j \sin(\delta_s)]\} \;\rightarrow$$

$$x_g^{e+} = x_g^{s+} \, e^{-j\delta_s} \tag{2.38}$$

Multiplying both sides of the expression (2.38) by $e^{j\delta_s}$ gives

$$x_g^{s+} = x_g^{e+} \, e^{j\delta_s} \tag{2.39}$$

Now, the same analysis can be done regarding negative coordinates through Figure 2.3.
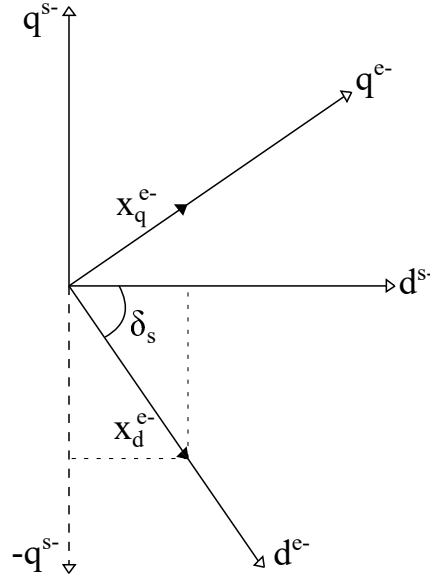
Figure 2.3 – Synchronous and stationary axis of negative sequence

From Figure 2.3, it is noticed that the generic quantity in the d coordinate for the negative sequence can be written as

$$x_d^{e-} = x_d^{s-} \cos(\delta_s) - x_q^{s-} \sin(\delta_s) \tag{2.40}$$

and the same quantity for the q coordinate is

$$x_q^{e-} = x_q^{s-} \cos(\delta_s) + x_d^{s-} \sin(\delta_s) \tag{2.41}$$

The vector form of the quantity in the negative reference synchronous is

$$x_g^{e-} = \frac{1}{\sqrt{2}} (x_d^{e-} + j x_q^{e-}) \tag{2.42}$$

Replacing expressions (2.40) and (2.41) in (2.42), the result is

$$x_g^{e-} = \frac{1}{\sqrt{2}} [x_d^{s-} \cos(\delta_s) - x_q^{s-} \sin(\delta_s) + j x_q^{s-} \cos(\delta_s) + j x_d^{s-} \sin(\delta_s)] \; \rightarrow$$

$$x_g^{e-} = \frac{1}{\sqrt{2}} \{ (x_d^{s-} + j x_q^{s-}) \left[\cos(\delta_s) + j \sin(\delta_s) \right] \} \; \rightarrow$$

$$x_g^{e-} = x_g^{s-} e^{j\delta_s} \tag{2.43}$$

Thus,

$$x_g^{s-} = x_g^{e-} e^{-j\delta_s} \tag{2.44}$$

Now, the relation between a quantity in stationary frame and its symmetrical components given by the expression (2.34) will be applied in the complex power expression (2.27), which gives the following result

$$S_{AC} = 2(e_g^{s+} + e_g^{s-})(i_g^{s+*} + i_g^{s-*}) \rightarrow$$

$$S_{AC} = 2[e_g^{s+}i_g^{s+*} + e_g^{s+}i_g^{s-*} + e_g^{s-}i_g^{s+*} + e_g^{s-}i_g^{s-*}] \tag{2.45}$$

As shown, a quantity in the stationary frame can be written in the positive and negative synchronous frame, following the relations given by (2.39) and (2.44). Therefore, the expression (2.45) of the complex power will be

$$S_{AC} = 2[(e_g^{e+}e^{j\delta_s})(i_g^{e+*}e^{-j\delta_s}) + (e_g^{e+}e^{j\delta_s})(i_g^{e-*}e^{j\delta_s}) + (e_g^{e-}e^{-j\delta_s})(i_g^{e+*}e^{-j\delta_s}) + (e_g^{e-}e^{-j\delta_s})(i_g^{e-*}e^{j\delta_s})] \rightarrow$$

$$S_{AC} = 2e_g^{e+}i_g^{e+*}e^0 + 2e_g^{e+}i_g^{e-*}e^{2j\delta_s} + 2e_g^{e-}i_g^{e+*}e^{-2j\delta_s} + 2e_g^{e-}i_g^{e-*}e^0 \rightarrow$$

$$S_{AC} = 2e_g^{e+}i_g^{e+*} + 2e_g^{e+}i_g^{e-*}e^{2j\delta_s} + 2e_g^{e-}i_g^{e+*}e^{-2j\delta_s} + 2e_g^{e-}i_g^{e-*} \tag{2.46}$$

Each multiplication term of the expression (2.46) will be developed separately to simplify the calculations. In this way, the positive-sequence terms are analyzed firstly, hence,

$$2e_g^{e+}i_g^{e+*} = 2\frac{1}{\sqrt{2}}(e_{gd}^{e+} + je_{gq}^{e+})\frac{1}{\sqrt{2}}(i_{gd}^{e+} - ji_{gq}^{e+}) \rightarrow$$

$$2e_g^{e+}i_g^{e+*} = e_{gd}^{e+}i_{gd}^{e+} - je_{gd}^{e+}i_{gq}^{e+} + je_{gq}^{e+}i_{gd}^{e+} + e_{gq}^{e+}i_{gq}^{e+} \tag{2.47}$$

Then, the negative sequence term

$$2e_g^{e-}i_g^{e-*} = 2\frac{1}{\sqrt{2}}(e_{gd}^{e-} + je_{gq}^{e-})\frac{1}{\sqrt{2}}(i_{gd}^{e-} - ji_{gq}^{e-}) \rightarrow$$

$$2e_g^{e-}i_g^{e-*} = e_{gd}^{e-}i_{gd}^{e-} - je_{gd}^{e-}i_{gq}^{e-} + je_{gq}^{e-}i_{gd}^{e-} + e_{gq}^{e-}i_{gq}^{e-} \tag{2.48}$$

The terms of expression (2.46) multiplicated by $e^{2j\delta_s}$ and $e^{-2j\delta_s}$ are the power terms that oscillate with twice the grid frequency, i.e., $2\omega_s$. And now, these terms will be analyzed, as follows

$$2e_g^{e+}i_g^{e-*}e^{2j\delta_s} = 2\frac{1}{\sqrt{2}}(e_{gd}^{e+} + je_{gq}^{e+})\frac{1}{\sqrt{2}}(i_{gd}^{e-} - ji_{gq}^{e-})e^{2j\delta_s} \rightarrow$$

$$2e_g^{e+}i_g^{e-*}e^{2j\delta_s} = (e_{gd}^{e+}i_{gd}^{e-} - je_{gd}^{e+}i_{gq}^{e-} + je_{gq}^{e+}i_{gd}^{e-} + e_{gq}^{e+}i_{gq}^{e-})e^{2j\delta_s} \tag{2.49}$$

And the last term of (2.46),

$$2e_g^{e-} i_g^{e+*} e^{-2j\delta_s} = 2\frac{1}{\sqrt{2}}(e_{gd}^{e-} + je_{gq}^{e-})\frac{1}{\sqrt{2}}(i_{gd}^{e+} - ji_{gq}^{e+})e^{-2j\delta_s} \rightarrow$$

$$2e_g^{e-} i_g^{e+*} e^{-2j\delta_s} = (e_{gd}^{e-} i_{gd}^{e+} - je_{gd}^{e-} i_{gq}^{e+} + je_{gq}^{e-} i_{gd}^{e+} + e_{gq}^{e-} i_{gq}^{e+})e^{-2j\delta_s} \tag{2.50}$$

The expressions (2.49) and (2.50) will be devolped by applying the Euler identity $e^{j\theta} = \cos(\theta) + j\sin(\theta)$ along the replacement of δ_s by $\omega_s t$. Hence, the expression (2.49) becomes

$$e_g^{e+} i_g^{e-*} e^{2j\delta_s} = (e_{gd}^{e+} i_{gd}^{e-} - je_{gd}^{e+} i_{gq}^{e-} + je_{gq}^{e+} i_{gd}^{e-} + e_{gq}^{e+} i_{gq}^{e-})[\cos(2\omega_s t) + j\sin(2\omega_s t)] \tag{2.51}$$

and now the expression (2.50) becomes

$$e_g^{e-} i_g^{e+*} e^{-2j\delta_s} = (e_{gd}^{e-} i_{gd}^{e+} - je_{gd}^{e-} i_{gq}^{e+} + je_{gq}^{e-} i_{gd}^{e+} + e_{gq}^{e-} i_{gq}^{e+})[\cos(2\omega_s t) - j\sin(2\omega_s t)] \tag{2.52}$$

Replacing the expressions (2.47), (2.48), (2.51), and (2.52) in the complex expression (2.46) gives the following result

$$\begin{aligned}
S_{AC} = &\, e_{gd}^{e+} i_{gd}^{e+} + e_{gq}^{e+} i_{gq}^{e+} + e_{gd}^{e-} i_{gd}^{e-} + e_{gq}^{e-} i_{gq}^{e-} \\
&+ \cos(2\omega_s t)(e_{gd}^{e+} i_{gd}^{e-} + e_{gq}^{e+} i_{gq}^{e-} + e_{gd}^{e-} i_{gd}^{e+} + e_{gq}^{e-} i_{gq}^{e+}) \\
&+ \sin(2\omega_s t)(e_{gd}^{e+} i_{gq}^{e-} - e_{gd}^{e-} i_{gq}^{e+} - e_{gq}^{e+} i_{gd}^{e-} + e_{gq}^{e-} i_{gd}^{e+}) \\
&+ j[-e_{gd}^{e+} i_{gq}^{e+} + e_{gq}^{e+} i_{gd}^{e+} - e_{gd}^{e-} i_{gq}^{e-} + e_{gq}^{e-} i_{gd}^{e-} \\
&+ \cos(2\omega_s t)(-e_{gd}^{e+} i_{gq}^{e-} + e_{gq}^{e+} i_{gd}^{e-} - e_{gd}^{e-} i_{gq}^{e+} + e_{gq}^{e-} i_{gd}^{e+}) \\
&+ \sin(2\omega_s t)(e_{gd}^{e+} i_{gd}^{e-} + e_{gq}^{e+} i_{gq}^{e-} - e_{gd}^{e-} i_{gd}^{e+} - e_{gq}^{e-} i_{gq}^{e+})] \tag{2.53}
\end{aligned}$$

Looking to the expression in (2.53), it is noted real and imaginary components that are related to the active and reactive powers, respectively. Therefore, it can be split into different expressions, one set is for active and other for the reactive power, as shown below

- Active power

$$P_{AC-C} = e_{gd}^{e+} i_{gd}^{e+} + e_{gq}^{e+} i_{gq}^{e+} + e_{gd}^{e-} i_{gd}^{e-} + e_{gq}^{e-} i_{gq}^{e-} \tag{2.54}$$

$$P_{AC-cos} = e_{gd}^{e+} i_{gd}^{e-} + e_{gq}^{e+} i_{gq}^{e-} + e_{gd}^{e-} i_{gd}^{e+} + e_{gq}^{e-} i_{gq}^{e+} \tag{2.55}$$

$$P_{AC-sin} = e_{gd}^{e+} i_{gq}^{e-} - e_{gd}^{e-} i_{gq}^{e+} - e_{gq}^{e+} i_{gd}^{e-} + e_{gq}^{e-} i_{gd}^{e+} \tag{2.56}$$

- Reactive power

$$Q_{AC-C} = -e_{gd}^{e+} i_{gq}^{e+} + e_{gq}^{e+} i_{gd}^{e+} - e_{gd}^{e-} i_{gq}^{e-} + e_{gq}^{e-} i_{gd}^{e-} \tag{2.57}$$

$$Q_{AC-cos} = -e_{gd}^{e+} i_{gq}^{e-} + e_{gq}^{e+} i_{gd}^{e-} - e_{gd}^{e-} i_{gq}^{e+} + e_{gq}^{e-} i_{gd}^{e+} \tag{2.58}$$

$$Q_{AC-sin} = e_{gd}^{e+} i_{gd}^{e-} + e_{gq}^{e+} i_{gq}^{e-} - e_{gd}^{e-} i_{gd}^{e+} - e_{gq}^{e-} i_{gq}^{e+} \tag{2.59}$$

By analysing the power expressions, it is noted that P_{AC-C} and Q_{AC-C} are the constant power terms, while P_{AC-cos}, P_{AC-sin}, Q_{AC-cos} and Q_{AC-sin} are the power terms that oscillate at twice the voltage frequency ($2\omega_s$). If there are no unbalances in the system, these oscillating components will be null, considering that the negative sequence terms will not exist. Besides, this set of expressions are the basis for the control strategies adoped in this work as they originate the expressions for the current references of the photovoltaic system.

2.3 PV MODEL

The identification of a photovoltaic module usually takes place through the peak power (W_p) determined under standard test conditions (STC). These conditions are specific to the module tests in the laboratory and are set as follows: $1000\,\text{W/m}^2$ for solar irradiance and $25\,°\text{C}$ for cell temperature. Other parameters obtained through these tests are the open-circuit voltage (V_{oc}) obtained by measuring the disconnected module terminals, and the short-circuit current (I_{SC}) measured by short-circuiting the module terminals (XIAO; DUNFORD; CAPEL, 2004).

The equivalent circuit of an ideal PV cell is shown in Figure 2.4, and according to (RAUSCHENBACH, 1980) its mathematical model is given by the following expression

$$I = I_{PV} - I_0 \left[e^{\left(\frac{qV}{\alpha kT} \right)} - 1 \right] \tag{2.60}$$

where I_{PV} is the photovoltaic current, I_0 is the cell's saturation current, q is the electron charge whose value is $1.60217646x10^{-19}\,\text{C}$, V and I are the terminal voltage and current, α is the diode ideality constant, K is the Boltzmann constant whose value is $1.3806503x10^{-23}\,\text{J/K}$, and T is the temperature in the p-n junction given in K.
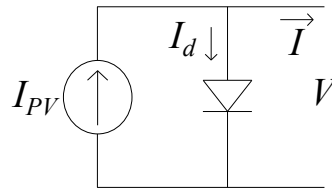
Figure 2.4 – Equivalent circuit of an ideal photovoltaic cell

However, the expression (2.60) does not represent a practical PV module composed of photovoltaic cells connected in series or parallel to achieve the desired power and voltage. Besides, these connections consequently form small resistances that represent losses in the module. Thus, Figure 2.5 shows the equivalent circuit of a practical PV module, and its expression that describes the I-V characteristics of the photovoltaic module is shown in (2.61) (VILLALVA; GAZOLI; FILHO, 2009).

$$I = I_{PV} - I_0 \left[e^{\left(\frac{V + R_s I}{V_t a} \right)} - 1 \right] - \frac{V + R_s I}{R_{sh}} \tag{2.61}$$

where $V_t = N_s KT/q$ is the thermal voltage with N_S cells connected in series, I_{PV} and I_0 are the photovoltaic and saturation currents, R_{sh} is the equivalent parallel resistance and models the leakage current, and R_s is the equivalent series resistance and represent the losses due to the current flow and electrical connections.
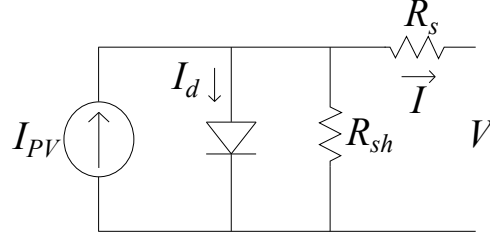
Figure 2.5 – Photovoltaic module's equivalent circuit

An essential characteristic of photovoltaic modules is their Current-Voltage (I-V) curves obtained through the expression (2.61), and they are important because the modelling is obtaining those curves. An I-V curve is shown in Figure 2.6, and some points must be highlighted, such as V_{MP} and I_{MP} that originate the maximum power point (MPP), the open circuit voltage (V_{oc},0), and the short-circuit current (0,I_{SC}).
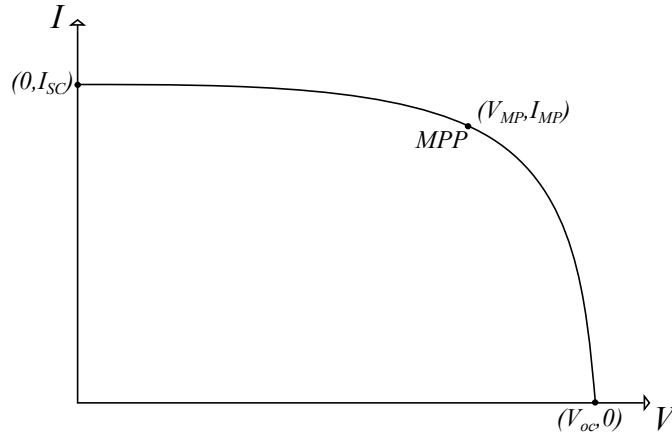
Figure 2.6 – Characteristic I-V curve

The photovoltaic system used in this work is composed of a boost DC-DC converter and a three-phase DC-AC inverter and has the nominal capacity to supply $20\,\mathrm{kW_p}$. The photovoltaic array has 50 panels in total, with five panels being connected in series to form a string, while there is a parallel connection of ten of these strings. Also, each photovoltaic panel can supply up to $400\,\mathrm{W_p}$ individually, and the model chosen to obtain the electrical parameters was the OSDA ODA400-36-MH. The main features of the PV system can be seen in Table 2.1, where the DC-link voltage parameter is for the voltage after the boost converter..

Table 2.1 – PV system parameters

Parameters	Value
Panels per string	5
Number of strings	10
Panel rated power	$400\,\mathrm{W_p}$
Array rated power	$20\,\mathrm{kW_p}$
DC-link voltage	1200 V
Boost switching frequency	10 kHz

2.4 MPPT TECHNIQUE

The photovoltaic system used in this work is connected to the electrical grid, requiring the application of power converters. These converters have two essential functions: the first one relates to the increase in the voltage generated by the photovoltaic array, which is generally not enough for the correct functioning of the DC-link, while the second function is related to the power conversion for the connection to the AC grid (KJAER; PEDERSEN; BLAABJERG, 2002).

In two-stage photovoltaic systems composed of a DC-DC stage followed by a DC-AC stage, it is customary to adopt the boost converter to carry out the PV array's input voltage increase, and also in addition to employing the maximum power point tracking technique to operate at its maximum efficiency. In a PV generation, temperature and irradiance variation affect its performance, reflecting on the power delivered to the electrical grid, and thus, the MPPT is used to maintain the operation at maximum power even when there are input changes. That said, the DC link voltage is generally set in a fixed point and the MPPT is responsible for controlling the input voltage levels of the array by modifying the converter's duty cycle, which checks whether there is a decrease or increase in the power delivered to the grid (FEMIA et al., 2005; ROCHA, 2015).

There are several methods for MPPT, among which Perturb and Observe (*P&O*) stand out, being the most common to be used. This method stands out because of its simplicity of implementation, as there is no need for studies on temperature or irradiance or the use of databases. Also, the method's simplicity implies greater versatility and cheaper implementation than other methods since there is no need to apply sensors other than voltage and current. Its operation consists of maintaining the operating point of the photovoltaic array around the maximum power point through iterations and power analysis (BRITO et al., 2012; VERMA et al., 2016; SUBUDHI; PRADHAN, 2012; ESRAM; CHAPMAN, 2007).

The traditional *P&O* algorithm works with a fixed disturbance applied to the output voltage terminal of the photovoltaic array, and the response provoked in the power is observed. In this way, the operating point of the panels is heading towards the MPP, if the voltage disturbance in a given direction implies an increase in the measured power of

the photovoltaic panels, requiring that the next disturbance occurs in the same direction. However, if the voltage disturbance gives rise to power decrease indicates that the MPP is moving away, thus requiring the next disturbance direction must be reversed. This process is to ensure that the system operates around the point $dV/dP = 0$ (VERMA et al., 2016; HUA; SHEN, 1998).

The flowchart of the algorithm for the *P&O* MPPT technique can be seen in Figure 2.7. The first step of this algorithm consists in reading the input current $I(j)$ and voltage $V(j)$ of the PV array, which in turn are used to calculate the currently active power $P(j)$. Besides, the differential terms for voltage and power, which are called dV and dP, are calculated from the current and previous signals of these quantities. After this, the analysis begins, and the first step consists to know whether the power differential term is negative or positive, once this information will be used to increase or decrease the voltage. Then, Assuming that the power differential term is negative, the algorithm now verifies whether the voltage differential term is negative or positive. Considering that the differential voltage term is negative, the voltage signal increases by adding a small disturbance d and decreases by the same value if the differential term is positive. However, if the differential power term is positive, the voltage decreases if the differential voltage term is negative, and increases otherwise. And finally, the voltage and power signals are updated, and the algorithm repeats.

2.5 CONCLUSION

In this chapter, the mathematical model of the photovoltaic system connected to the power grid with unbalances and the basic expressions for the control strategies of this work are presented. The analysis carried out considered an unbalanced three-phase power grid, whose characteristics include the presence of negative and homopolar symmetric components of current and voltage, but the last one is neglected as the system used here is three-wired. This symmetric component influences the active and reactive powers because they cause oscillations in such quantities to arise. A detailed step-by-step was carried out to show the relations between the symmetric components and the reactive and active powers, which culminated in a set of expressions that highlight the appearance of oscillating terms of power at twice the grid frequency. These expressions serve as the basis for the control strategies adopted in this work. In addition to this analysis, the PV model was shown, including the I-V curve, and equivalent circuits of a PV module that are the main modeling elements. Besides, the MPPT technique used in the DC-DC converter of the PV system was presented, in which the *P&O* was chosen, once it is the most used and the simplest one.
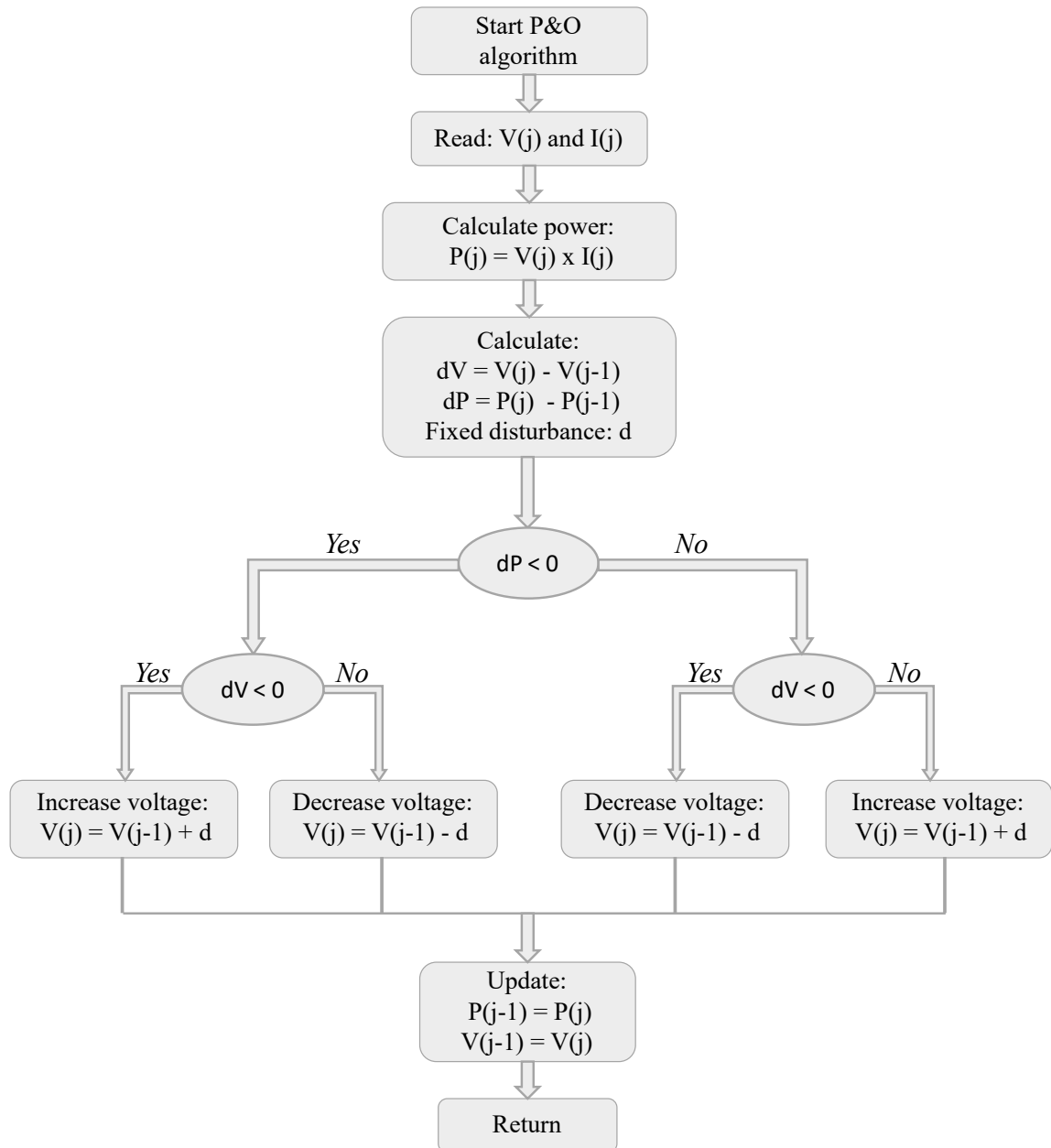
Figure 2.7 – *P&O* flowchart

3 CONTROL SYSTEM

3.1 INTRODUCTION

In this chapter, the control system of the on-grid photovoltaic system will be presented, including the strategies adoped and the control structure. The main tools used in the control strategies are the expressions developed in the previous chapter, once they result in the current references of the PV system inverter. There are three control strategies: the first is to inject balanced currents into the grid by eliminating the negative sequence current, the second and third are reducing active and reactive power oscillations, respectively. The regulation of currents occurs through a structure that uses the negative and positive symmetrical components in the grid synchronous reference frame and, therefore, is called Double Synchronous Reference Frame (DSRF).

3.2 CONTROL STRATEGIES

Three possibilities of control strategies based on the control of the symmetrical components of the current delivered into the power grid by the inverter are used here. The first one allows mitigating the negative component of the current, which provides balanced currents to the grid. The other strategies are focused on diminishing the double frequency oscillation in the active and reactive power, which improves the quality of the energy delivered to the utility grid.

3.2.1 Control strategy 1

The first control strategy targets to amortize the negative sequence components of the current, rendering them null. For this, the expressions (2.54) and (2.57) must be used, and they can still be written in matrix form, as follows

$$
\begin{bmatrix} P_{AC-C} \\ Q_{AC-C} \end{bmatrix} = \begin{bmatrix} e_{gd}^{e+} & e_{gq}^{e+} & e_{gd}^{e-} & e_{gq}^{e-} \\ e_{gq}^{e+} & -e_{gd}^{e+} & e_{gq}^{e-} & -e_{gd}^{e-} \end{bmatrix} \begin{bmatrix} i_d^{e+} \\ i_q^{e+} \\ i_d^{e-} \\ i_q^{e-} \end{bmatrix}
\tag{3.1}
$$

The purpose here is to ensure that the negative-sequence components of the current are eliminated and, for that, they must be considered zero in the matrix expression (3.1), which will become

$$
\begin{bmatrix} P_{AC-C} \\ Q_{AC-C} \end{bmatrix} = \begin{bmatrix} e_{gd}^{e+} & e_{gq}^{e+} \\ e_{gq}^{e+} & -e_{gd}^{e+} \end{bmatrix} \begin{bmatrix} i_d^{e+} \\ i_q^{e+} \end{bmatrix}
\tag{3.2}
$$

The goal here is to isolate the currents in expression (3.2), as follows

$$
\begin{bmatrix} i_d^{e+} \\ i_q^{e+} \end{bmatrix} = \begin{bmatrix} e_{gd}^{e+} & e_{gq}^{e+} \\ e_{gq}^{e+} & -e_{gd}^{e+} \end{bmatrix}^{-1} \begin{bmatrix} P_{AC-C} \\ Q_{AC-C} \end{bmatrix}
\tag{3.3}
$$

The inverse matrix of the voltage matrix in expression (3.3) is

$$
\begin{bmatrix} e_{gd}^{e+} & e_{gq}^{e+} \\ e_{gq}^{e+} & -e_{gd}^{e+} \end{bmatrix}^{-1} = \begin{bmatrix} \dfrac{e_{gd}^{e+}}{(e_{gd}^{e+})^2 + (e_{gq}^{e+})^2} & \dfrac{e_{gq}^{e+}}{(e_{gd}^{e+})^2 + (e_{gq}^{e+})^2} \\ \dfrac{e_{gq}^{e+}}{(e_{gd}^{e+})^2 + (e_{gq}^{e+})^2} & \dfrac{-e_{gd}^{e+}}{(e_{gd}^{e+})^2 + (e_{gq}^{e+})^2} \end{bmatrix}
\tag{3.4}
$$

Replacing expression (3.4) in (3.3), it results in

$$
\begin{bmatrix} i_d^{e+} \\ i_q^{e+} \end{bmatrix} = \begin{bmatrix} \dfrac{e_{gd}^{e+}}{(e_{gd}^{e+})^2 + (e_{gq}^{e+})^2} & \dfrac{e_{gq}^{e+}}{(e_{gd}^{e+})^2 + (e_{gq}^{e+})^2} \\ \dfrac{e_{gq}^{e+}}{(e_{gd}^{e+})^2 + (e_{gq}^{e+})^2} & \dfrac{-e_{gd}^{e+}}{(e_{gd}^{e+})^2 + (e_{gq}^{e+})^2} \end{bmatrix} \begin{bmatrix} P_{AC-C} \\ Q_{AC-C} \end{bmatrix}
\tag{3.5}
$$

Separately isolating each of the currents in (3.5), it is possible writing these current reference terms in the function of constant active and reactive powers among the voltage, resulting in

$$
i_{d\_ref}^{e+} = \frac{e_{gd}^{e+}}{\left(e_{gd}^{e+}\right)^2 + \left(e_{gq}^{e+}\right)^2} P_{AC-C} + \frac{e_{gq}^{e+}}{\left(e_{gd}^{e+}\right)^2 + \left(e_{gq}^{e+}\right)^2} Q_{AC-C}
\tag{3.6}
$$

$$
i_{q\_ref}^{e+} = \frac{e_{gq}^{e+}}{\left(e_{gd}^{e+}\right)^2 + \left(e_{gq}^{e+}\right)^2} P_{AC-C} - \frac{e_{gd}^{e+}}{\left(e_{gd}^{e+}\right)^2 + \left(e_{gq}^{e+}\right)^2} Q_{AC-C}
\tag{3.7}
$$

3.2.2 Control strategy 2

Control strategy 2 consists of attenuating the active power components that oscillate at twice the frequency of grid. Hence, expressions (2.54) to (2.57) should be used, which can be organized in matrix form to facilitate manipulation, as follows

$$
\begin{bmatrix} P_{AC-C} \\ Q_{AC-C} \\ P_{AC-cos} \\ P_{AC-sin} \end{bmatrix} = \begin{bmatrix} e_{gd}^{e+} & e_{gq}^{e+} & e_{gd}^{e-} & e_{gq}^{e-} \\ e_{gq}^{e+} & -e_{gd}^{e+} & e_{gq}^{e-} & -e_{gd}^{e-} \\ e_{gd}^{e-} & e_{gq}^{e-} & e_{gd}^{e+} & e_{gq}^{e+} \\ e_{gq}^{e-} & -e_{gd}^{e-} & -e_{gq}^{e+} & e_{gd}^{e+} \end{bmatrix} \begin{bmatrix} i_d^{e+} \\ i_q^{e+} \\ i_d^{e-} \\ i_q^{e-} \end{bmatrix}
\tag{3.8}
$$

To be able to apply the proposed strategy, it must be assumed that the oscillatory terms of the active power are null in (3.8), that is, $P_{AC-cos} = P_{AC-sin} = 0$. By considering such propositions is possible to guarantee the attenuation of active power oscillations

with twice the frequency. So, taking into account the propositions, the matrix in 3.8 now becomes

$$
\begin{bmatrix} P_{AC-C} \\ Q_{AC-C} \\ 0 \\ 0 \end{bmatrix} = \begin{bmatrix} e_{gd}^{e+} & e_{gq}^{e+} & e_{gd}^{e-} & e_{gq}^{e-} \\ e_{gq}^{e+} & -e_{gd}^{e+} & e_{gq}^{e-} & -e_{gd}^{e-} \\ e_{gd}^{e-} & e_{gq}^{e-} & e_{gd}^{e+} & e_{gq}^{e+} \\ e_{gq}^{e-} & -e_{gd}^{e-} & -e_{gq}^{e+} & e_{gd}^{e+} \end{bmatrix} \begin{bmatrix} i_d^{e+} \\ i_q^{e+} \\ i_d^{e-} \\ i_q^{e-} \end{bmatrix} \tag{3.9}
$$

Isolating the current matrix in (3.9), it results in

$$
\begin{bmatrix} i_d^{e+} \\ i_q^{e+} \\ i_d^{e-} \\ i_q^{e-} \end{bmatrix} = \begin{bmatrix} e_{gd}^{e+} & e_{gq}^{e+} & e_{gd}^{e-} & e_{gq}^{e-} \\ e_{gq}^{e+} & -e_{gd}^{e+} & e_{gq}^{e-} & -e_{gd}^{e-} \\ e_{gd}^{e-} & e_{gq}^{e-} & e_{gd}^{e+} & e_{gq}^{e+} \\ e_{gq}^{e-} & -e_{gd}^{e-} & -e_{gq}^{e+} & e_{gd}^{e+} \end{bmatrix}^{-1} \begin{bmatrix} P_{AC-C} \\ Q_{AC-C} \\ 0 \\ 0 \end{bmatrix} \tag{3.10}
$$

The following results are obtained for the reference currents of positive and negative components as a function of voltage, and constant active and reactive powers from expression (3.10)

$$
i_{d\_ref}^{e+} = \frac{e_{gd}^{e+}}{D_1} P_{AC-C} + \frac{e_{gq}^{e+}}{D_2} Q_{AC-C} \tag{3.11}
$$

$$
i_{q\_ref}^{e+} = \frac{e_{gq}^{e+}}{D_1} P_{AC-C} - \frac{e_{gd}^{e+}}{D_2} Q_{AC-C} \tag{3.12}
$$

$$
i_{d\_ref}^{e-} = \frac{-e_{gd}^{e-}}{D_1} P_{AC-C} + \frac{e_{gq}^{e-}}{D_2} Q_{AC-C} \tag{3.13}
$$

$$
i_{q\_ref}^{e-} = \frac{-e_{gq}^{e-}}{D_1} P_{AC-C} - \frac{e_{gd}^{e-}}{D_2} Q_{AC-C} \tag{3.14}
$$

where

$$
D_1 = (e_{gd}^{e+})^2 + (e_{gq}^{e+})^2 - (e_{gd}^{e-})^2 - (e_{gq}^{e-})^2 \tag{3.15}
$$

$$
D_2 = (e_{gd}^{e+})^2 + (e_{gq}^{e+})^2 + (e_{gd}^{e-})^2 + (e_{gq}^{e-})^2 \tag{3.16}
$$

and they must be nonzero.

3.2.3 Control Strategy 3

In this strategy, the target is to attenuate the reactive power components that oscillate with twice the frequency due to the appearance of the negative sequence component of the current. There will be considered the expressions (2.54) and (2.57) to (2.59) to carry out this strategy. Thus, organizing these expressions in matrix form, we obtain

$$
\begin{bmatrix} P_{AC-C} \\ Q_{AC-C} \\ Q_{AC-cos} \\ Q_{AC-sin} \end{bmatrix} = \begin{bmatrix} e_{gd}^{e+} & e_{gq}^{e+} & e_{gd}^{e-} & e_{gq}^{e-} \\ e_{gq}^{e+} & -e_{gd}^{e+} & e_{gq}^{e-} & -e_{gd}^{e-} \\ e_{gq}^{e-} & -e_{gd}^{e-} & e_{gq}^{e+} & -e_{gd}^{e+} \\ -e_{gd}^{e-} & -e_{gq}^{e-} & e_{gd}^{e+} & e_{gq}^{e+} \end{bmatrix} \begin{bmatrix} i_d^{e+} \\ i_q^{e+} \\ i_d^{e-} \\ i_q^{e-} \end{bmatrix} \tag{3.17}
$$

It is necessary to consider null in (3.17) the oscillating components of the reactive power to achieve control strategy 3, that is, $Q_{CA-cos} = Q_{CA-sin} = 0$. These considerations make it possible to attenuate fluctuations in reactive power and result in the following matrix expression

$$\begin{bmatrix} P_{AC-C} \\ Q_{AC-C} \\ 0 \\ 0 \end{bmatrix} = \begin{bmatrix} e_{gd}^{e+} & e_{gq}^{e+} & e_{gd}^{e-} & e_{gq}^{e-} \\ e_{gq}^{e+} & -e_{gd}^{e+} & e_{gq}^{e-} & -e_{gd}^{e-} \\ e_{gq}^{e-} & -e_{gd}^{e-} & e_{gq}^{e+} & -e_{gd}^{e+} \\ -e_{gd}^{e-} & -e_{gq}^{e-} & e_{gd}^{e+} & e_{gq}^{e+} \end{bmatrix} \begin{bmatrix} i_d^{e+} \\ i_q^{e+} \\ i_d^{e-} \\ i_q^{e-} \end{bmatrix} \tag{3.18}$$

Isolating the currents in matrix (3.18), the matrix expression becomes

$$\begin{bmatrix} i_d^{e+} \\ i_q^{e+} \\ i_d^{e-} \\ i_q^{e-} \end{bmatrix} = \begin{bmatrix} e_{gd}^{e+} & e_{gq}^{e+} & e_{gd}^{e-} & e_{gq}^{e-} \\ e_{gq}^{e+} & -e_{gd}^{e+} & e_{gq}^{e-} & -e_{gd}^{e-} \\ e_{gq}^{e-} & -e_{gd}^{e-} & e_{gq}^{e+} & -e_{gd}^{e+} \\ -e_{gd}^{e-} & -e_{gq}^{e-} & e_{gd}^{e+} & e_{gq}^{e+} \end{bmatrix}^{-1} \begin{bmatrix} P_{AC-C} \\ Q_{AC-C} \\ 0 \\ 0 \end{bmatrix} \tag{3.19}$$

Now, the positive and negative components of the reference current can be expressed as a function of voltage, and constant active and reactive powers, as follows

$$i_{d\_ref}^{e+} = \frac{e_{gd}^{e+}}{D_2} P_{AC-C} + \frac{e_{gq}^{e+}}{D_1} Q_{AC-C} \tag{3.20}$$

$$i_{q\_ref}^{e+} = \frac{e_{gq}^{e+}}{D_2} P_{AC-C} - \frac{e_{gd}^{e+}}{D_1} Q_{AC-C} \tag{3.21}$$

$$i_{d\_ref}^{e-} = \frac{e_{gd}^{e-}}{D_2} P_{AC-C} - \frac{e_{gq}^{e-}}{D_1} Q_{AC-C} \tag{3.22}$$

$$i_{q\_ref}^{e-} = \frac{e_{gq}^{e-}}{D_2} P_{AC-C} + \frac{e_{gd}^{e-}}{D_1} Q_{AC-C} \tag{3.23}$$

3.3 CONTROL STRUCTURE

Some of the functions of the PV system control are shown in Figure 3.1. Note that x can represent any quantity generated as a reference for the internal current control, such as a power or current signal.

The control system of the Figure 3.1 consists a cascade architecture composed of two main methodologies, whose functions are:

- Inner loop current control: it is responsible for providing the voltage references for the pulse modulator of the three-phase inverter;

- outer loop DC-link voltage control: It keeps the DC bus voltage constant, even with disturbances, and can also determine the amplitudes of the currents injected by the inverter into the grid, i.e., it supplies the reference currents for the internal current loop or even the active power reference signal;
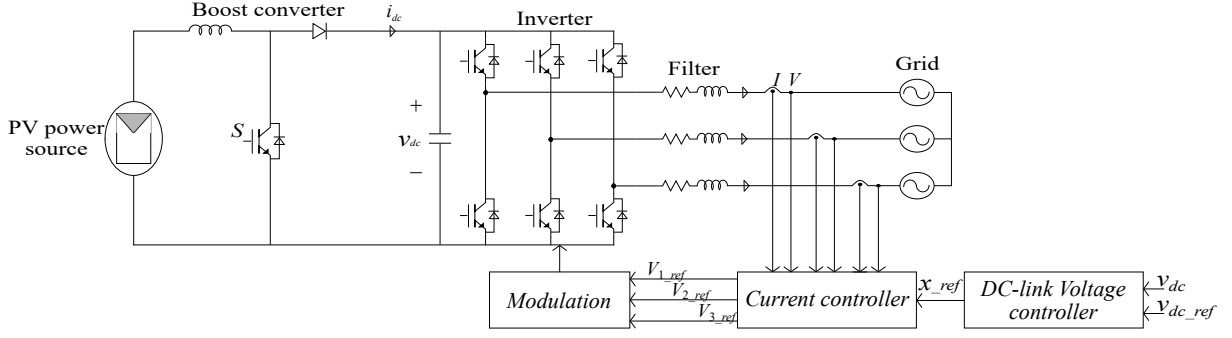
Figure 3.1 – Control system's functions

3.3.1 Current control inner loop

The objective here is controlling the currents injected by the PV system into the grid through the inverter output voltages.

The analysis will start with a balanced three-phase power grid, whose mathematical model in *dq* coordinates is given by the expressions (2.21) and (2.22). Those expressions are in the generic reference frame and can be changed to the voltage grid synchronous reference frame, which result in

$$e_{gd}^e = v_{cd}^e - R_f i_d^e + \omega_s L_f i_q^e - L_f \frac{di_d^e}{dt} \tag{3.24}$$

$$e_{gq}^e = v_{cq}^e - R_f i_q^e - \omega_s L_f i_d^e - L_f \frac{di_q^e}{dt} \tag{3.25}$$

Applying the Laplace's Transform in (3.24) and (3.25), the result is

$$E_{gd}^e(s) = V_{cd}^e(s) - R_f I_d^e(s) + \omega_s L_f I_q^e(s) - L_f s I_d^e(s) \tag{3.26}$$

$$E_{gq}^e(s) = V_{cq}^e(s) - R_f I_q^e(s) - \omega_s L_f I_d^e(s) - L_f s I_q^e(s) \tag{3.27}$$

Rearranging expressions (3.26) and (3.27), it obtains

$$V_{cd}^e(s) + \omega_s L_f I_q^e(s) - E_{gd}^e(s) = I_d^e(s)(R_f + L_f s) \tag{3.28}$$

$$V_{cq}^e(s) - \omega_s L_f I_d^e(s) - E_{gq}^e(s) = I_q^e(s)(R_f + L_f s) \tag{3.29}$$

As can be seen in expressions (3.28) and (3.29), when performing the reference frame change, the following coupling terms $\omega_s L_f I_q^e(s)$ and $\omega_s L_f I_d^e(s)$ appear, which makes it hard to acquire a transfer function (TF) that relates the currents and voltages at the inverter output and the independent control of the components *dq*. However, it is possible to overcome this situation by performing a decoupling using cross decoupling terms, and this will be shown in more detail later. Besides, aiming at controlling the current injected by the inverter, its output voltages $V_{cd}^e(s)$ and $V_{cq}^e(s)$ are control variables, currents $I_d^e(s)$ and $I_q^e(s)$ are process variables and voltages $E_{gd}^e(s)$ and $E_{gq}^e(s)$ are disturbances. Thus,

considering that the control is sufficiently robust to perform disturbance compensation, a decoupled system, and making

$$V_{cd}^e(s) + \omega_s L_f I_q^e(s) - E_{gd}^e(s) = V_{cd}'^e(s) \tag{3.30}$$

$$V_{cq}^e(s) - \omega_s L_f I_d^e(s) - E_{gq}^e(s) = V_{cq}'^e(s) \tag{3.31}$$

Those expressions (3.28) and (3.29) now become

$$V_{cd}'^e(s) = I_d^e(s)(R_f + L_f s) \tag{3.32}$$

$$V_{cq}'^e(s) = I_q^e(s)(R_f + L_f s) \tag{3.33}$$

Now, considering only the d component, the following TF that relates the injected current and the voltage at the inverter output is obtained

$$G_{vi}(s) = \frac{I_d^e(s)}{V_{cd}'^e(s)} = \frac{1}{R_f + sL_f} \tag{3.34}$$

Note that by the TF of expression (3.34), R_f and L_f are constant, and the inverter sees the filter circuit as load, whose TF is

$$\frac{1}{R_f + sL_f}$$

and which is taken as the plant of the system.

Now, it is possible to draw a block diagram representing the current control inner loop for each d and q axes, as can seen in Figures 3.2 and 3.3. In those figures, $i_{d\_ref}^e$ and $i_{q\_ref}^e$ are the reference currents, i_d^e and i_q^e are the measured currents in dq reference frame, $i_q^e \omega_s L_f$ and $i_d^e \omega_s L_f$ are the decoupling terms, and $G_{inv}(s)$ is the inverter's TF.
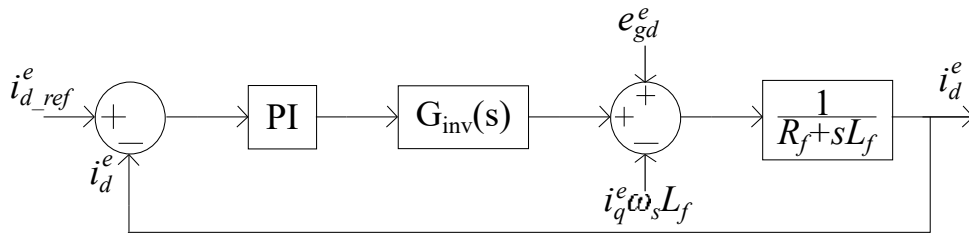
Figure 3.2 – Response system with plant and current control inner loop for the d axis

The control of the inverter currents of the photovoltaic system makes use of the PI type controller, as shown in Figures 3.2 and 3.3, and this is due to the good functioning of this controller with variables in dq synchronous reference frame since in this reference the signals are constant. Besides, it notes that the first control step embraces an error generation, arising from the differences between the reference currents, $i_{d\_ref}^e$ and $i_{q\_ref}^e$, and the measured currents, i_d^e and i_q^e. These differences go through a PI controller and
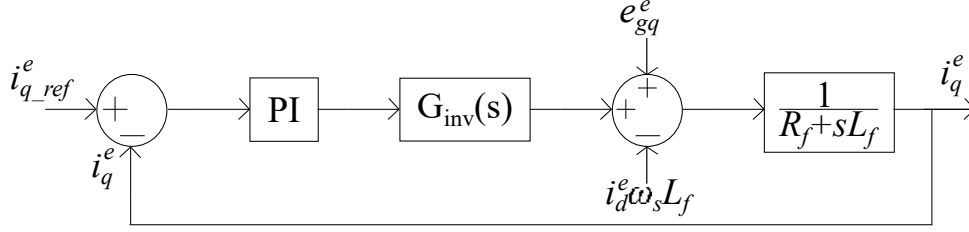
Figure 3.3 – Response system with plant and current control inner loop for the q axis

generate voltage signals. To these signals are added the crossed terms $-i_q^e \omega_s L_f$ and $i_d^e \omega_s L_f$, whose effect is to allow the decoupling of the dq axes and their independent controls (BLAABJERG, 2006; YANG et al., 2014). Also, as the grid voltages (e_{gd}^e and e_{gq}^e) are disturbances, they might be compensated and it can happen through a feedforward compensation, in which they a added. Finally, these resulting voltage signals at the end are references to the PWM, generating the inverter switching signals.

3.3.1.1   Tuning the current PI controller

As PI controllers are used here, their correct dimensioning is the key for regulating the controlled quantities. Its dimensioning consists of determining the proportional and integral gains. For this, its TF must be known, which is given by

$$D(s) = k_p + \frac{k_i}{s} \tag{3.35}$$

where k_p and k_i are the proportional and integral gains, respectively.

At this point, the three-phase inverter will be considered ideal, implying that its TF $G_{inv}(s)$ will assume the value of 1 in Figure 3.2. Furthermore, disregarding disturbances, the decoupling terms and using expressions (3.35), it is obtained the block diagram in Figure 3.4, in which is considered a generic current that represents both axes dq as the same procedure is done for each of them.
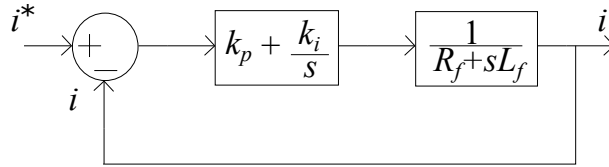
Figure 3.4 – Closed loop blok diagram for current control

The open-loop TF in Figure 3.4 will be given by the following expression

$$G_{oi}(s) = \frac{k_{pi}s + k_{ii}}{s} \frac{1}{R_f + sL_f} \tag{3.36}$$

Now, the closed-loop TF is given by

$$G_{ci}(s) = \frac{G_{oi}(s)}{G_{oi}(s) + 1} \tag{3.37}$$

Replacing the expression (3.36) in (3.37), the result is

$$G_{ci}(s) = \frac{k_{pi}s + k_{ii}}{s^2 + \dfrac{(R_f + k_{pi})}{L_f}s + \dfrac{k_{ii}}{L_f}} \qquad (3.38)$$

Comparing the denominator of expression (3.38) with the second-order characteristic equation, described as

$$s^2 + 2\zeta\omega_n s + \omega_n^2 \qquad (3.39)$$

where ω_n is the natural frequency of the system, and ζ is the damping factor. Thus, the following values of the integral and proportional gains of the current PI controller are reached

$$k_{ii} = \omega_n^2 L_f \qquad (3.40)$$

$$k_{pi} = 2\omega_n\zeta L_f - R_f \qquad (3.41)$$

3.3.2   DC-link voltage control outer loop

The DC-link voltage controller is sized to balance system power flow. System control is achieved by controlling the power flow between the inverter and the grid, to the point that increasing or decreasing the power injected by the inverter increases or decreases the DC voltage, keeping the latter under control. Typically, the design of this controller aims at stability and regulation of the system, having a slower response than the current inner controller. Figure 3.5 shows the electrical quantities relevant to the DC-link.
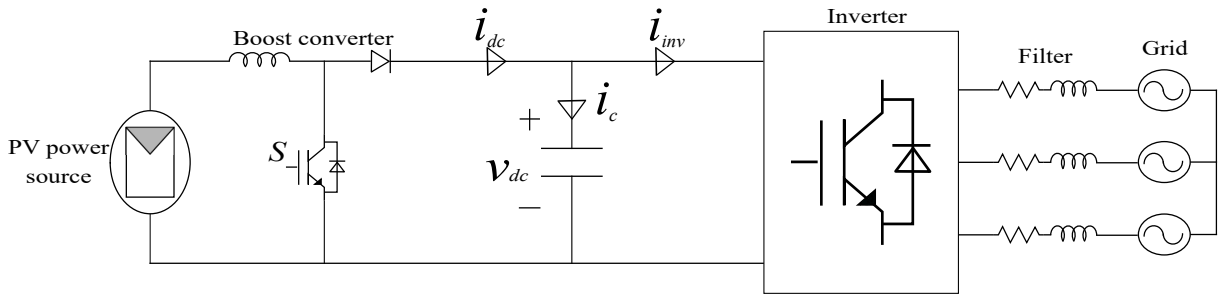
Figure 3.5 – DC-link quantities

Appying the Kirchoff's Current Law (KCL) in the DC-link of Figure 3.5, we obtain the following current expression

$$i_{inv}(t) + i_c(t) = i_{dc}(t) \qquad (3.42)$$

The current flowing through the DC-link capacitor in Figure 20 is given by

$$i_c(t) = C\frac{dv_{dc}(t)}{dt} \qquad (3.43)$$

Replacing expression (3.43) in (3.42), the result is

$$i_{inv}(t) + C\frac{dv_{dc}(t)}{dt} = i_{dc}(t) \tag{3.44}$$

The target of the DC-link control system is keeping its voltage stable. For this, the derivate term in (3.46) must be zero, i.e.,

$$\frac{dv_{dc}(t)}{dt} = 0\,, \tag{3.45}$$

resulting in

$$i_{inv}(t) = i_{dc}(t) \tag{3.46}$$

The input power supplied by the PV system will be assumed as constant, hence, the PV power source can be modeled as

$$P_{in-inv} = i_{dc}(t)v_{dc}(t) \tag{3.47}$$

The output power of the inverter in the AC side can be written as a function of current and voltage in the synchronous reference frame, as follows

$$P_{out-inv} = v_{cd}^e i_d^e + v_{cq}^e i_q^e \tag{3.48}$$

where v_{cd}^e and v_{cq}^e are the voltages at the output inverter, and i_d^e and i_q^e are the currents.

The system here is taken as balanced and there is no reactive power injection so far, then, the reactive voltage term will be null, hence

$$P_{out-inv} = v_{cd}^e i_d^e \tag{3.49}$$

The balance power is achieved through the following expression

$$P_{out-inv} = P_{in-inv} \tag{3.50}$$

Replacing expressions (3.47) and (3.49) in (3.50), the result is

$$v_{cd}^e i_d^e = i_{dc}v_{dc} \tag{3.51}$$

From expression (3.51), it is noted that the DC-link voltage v_{dc} is under control by regulating the current i_d^e.

And now, applying the Laplace transform to expression (3.43), the following result is obtained

$$I_c(s) = sCV_{dc}(S)\,, \tag{3.52}$$

which in turn results in the DC-link plant, whose TF is

$$G_{DC-link}(s) = \frac{V_{dc}(s)}{I_c(s)} = \frac{1}{sC} \tag{3.53}$$

Figure 3.6 shows the control block diagram in cascade with outer and inner loops for DC-link voltage and injected currents, respectively.
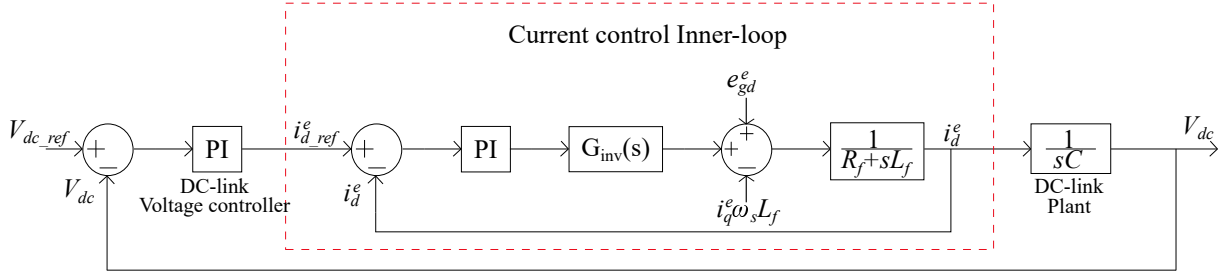
Figure 3.6 – Block diagram for cascade control loop

3.3.3 Tuning the DC-link voltage PI controller

Using the alredy known TF for the PI controller, and also negligecting the disturbances and current control inner loop, it is possible to determine the open loop TF for the voltage control, whose expression is composed by the DC-link plant (3.53), and the PI tranfer function (3.35). The open loop schematic can be seen in Figure 3.7.
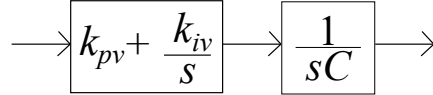
Figure 3.7 – Block diagram for the voltage control open loop

The open loop tranfer function of the block diagram in Figure 3.7 is given by

$$G_{ov}(s) = \frac{k_{pv}s + k_{iv}}{s}\frac{1}{sC} = \frac{k_{pv}s + k_{iv}}{s^2 C} \tag{3.54}$$

According to expression (3.37), the closed loop TF using (3.54) is

$$G_{cv}(s) = \frac{(k_{pv}s + k_{iv})/(s^2 C)}{1 + (k_{pv}s + k_{iv})/(s^2 C)} = \frac{k_{pv}s + k_{iv}}{s^2 C + k_{pv}s + k_{iv}} \tag{3.55}$$

One way to obtain the poles of the system is by comparing the denominator of its closed-loop TF with the second-order characteristic equation that is given by (3.39).

Hence, the denominator of (3.55) must be divided by C to ensure equality comparison, which results in

$$s^2 + \frac{k_{pv}}{C}s + \frac{k_{iv}}{C} \tag{3.56}$$

Through the comparison between expressions (3.39) and (3.56), the values of the integral and proportional gains of the DC-link voltage PI controller are obtained as follows

$$k_{iv} = \omega_n{}^2 C \tag{3.57}$$

$$k_{pv} = 2\zeta\omega_n C \tag{3.58}$$

To summarize the control development done so far, Figure 3.8 displays the whole control structure, including the inner and outer control for the injected currents and the DC-link voltage, respectively. Remember that this system was developed regarding a scenario with a balanced grid, implying the non-appearance of negative sequence components.
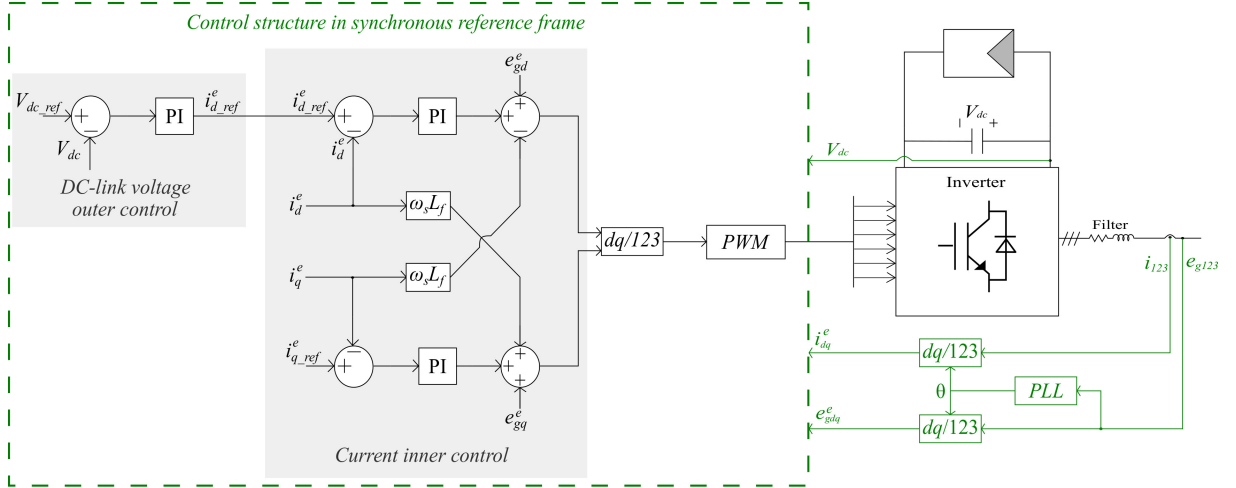
Figure 3.8 – Complete structure of the control system

3.3.4 Phase Locked Loop

To perform the Park transform for the synchronous reference frame of the electrical grid, it is necessary to know the voltage angle, which is obtained through the use of a PLL, whose implementation scheme is illustrated in Figure 3.9 (RODRÍGUEZ et al., 2007). In addition to helping the transform, PLL is also a tool responsible for synchronizing with the grid. This control tool produces an output signal synchronously and with the same phase and frequency as a given input signal. As the PLL keeps input and output frequencies signals equal in the steady-state, it becomes possible to track the sampled signal.
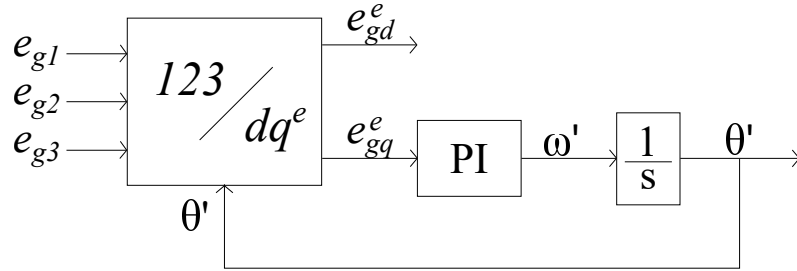
Figure 3.9 – Synchronous Reference Frame PLL

According to (RODRÍGUEZ et al., 2007), the PLL based on the synchronous frame in Figure 3.9 is commonly used in applications related to three-phase systems. It makes use of the transformation of stress vectors from 123 natural reference frame to *dq*. A response loop controls the reference angle, regulating the q component to zero.

3.3.5 Tuning the PLL PI controller

The block diagram for the PLL is displayed in Figure 3.10, which can be adjusted based on the d-axis alignment with v_d, and this implies that the voltage along the q-axis is null, i.e., $v_q = 0$.
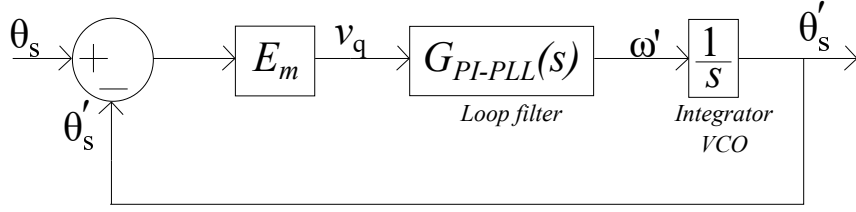
Figure 3.10 – Control loop block diagram for PLL

From Figure 3.10, the voltage v_q can be expressed as follows

$$v_q = E_m sin(\delta) \tag{3.59}$$

where δ is the angle difference given by $\theta_s - \theta_s'$, which is too small and can be negligected, resulting in

$$v_q = E_m \delta \tag{3.60}$$

The angular frequency of the PLL is given by

$$\omega' = \frac{d\theta_s'}{dt} = G_{PI-PLL}v_q = G_{PI-PLL}E_m\delta \tag{3.61}$$

where G_{PI-PLL} is the TF of the PLL's PI controller, whose expression is given by

$$G_{PI-PLL}(s) = k_p^{PLL} + \frac{k_i^{PLL}}{s} \tag{3.62}$$

The closed loop TF of 3.10 is

$$G_{c-PLL} = \frac{G_{PI-PLL}(s)E_m}{s + G_{PI-PLL}(s)E_m} \tag{3.63}$$

Again, the objective here is to determine the poles of the TF given in expression (3.63). For this, expression (3.62) must be replaced in (3.63), and after that, equal its denominator to zero, which gives the following result

$$s^2 + k_p^{PLL}E_m s + k_i^{PLL} = 0 \tag{3.64}$$

Comparing expression (3.64) with (3.39) related to second order characteristic equation, it is possible to obtain the integral and proportional gains, as follows

$$k_p^{PLL} = \frac{2\zeta\omega_n}{E_m} \tag{3.65}$$

$$k_i^{PLL} = \frac{\omega_n^2}{E_m} \tag{3.66}$$

where

- $\zeta = 1/\sqrt{2}$ is the damping factor;

- $E_m = \sqrt{2}V_L/\sqrt{3}$, which is the voltage peak value;

- $\omega_n = 120\pi \, rad/s$ is the voltage natural frequency ($60 \, Hz$).

3.4   CONTROL STRUCTURE FOR UNBALANCED POWER GRID

In this section, the modifications made to the control structure of the PV system when it is connected to an unbalanced grid will be shown. The unbalance situation gives rise to the negative sequence components of current and voltage, whose presence can provoke instabilities in the controllers. Thus, to remedy these instabilities, changes are made so that the control system takes these negative sequence components into account.

3.4.1   Current control inner loop

The three-wire and four-wire configurations enhace the top ones employed in the utility power grid. Naturally, those system operates in unbalanced scenarios whether due to an irregular load distribution among their phases or faults. These unbalances compromise the system operation and realibility, hence, the control configuration. The main problems arise with the symmetrical components, especially the negative and homopolar. However, the last one appears just for four-wire systems, and since the present paper use a three-wire system, this component is negligected.

An effective way to control the symmetrical components of a current vector is through a structure control based on Double Synchronous Reference Frame (DSRF). This configuration is able to regulate the current vector that rotates according to the grid frequency in a positive and negative direction simultaneously (TEODORESCU; LISERRE; RODRIGUEZ, 2011). The metioned system can be seen in Figure 3.11.

As the control scheme uses symmetrical components, some tool is needed to extract them. In this way, to extract the positive and negative sequence components of the voltages and currents necessary for the control, the positive sequence detector DSOGI-PLL (Dual Second Order Generalized Integrator - Phase Locked Loop) presented by (RODRIGUEZ et al., 2006) was used. This detector will be further analyzed in the next section.

3.4.2   Positive Sequence Detector Model

Figure 3.12 shows the DSOGI-PLL block diagram.

There are three highlighted blocks in the positive-sequence detector model of Figure 20, which are:

- Dual Second Order Generalized Integrator for Quadrature Signals Genaration (DSOGI-QSG): this block is responsible for generating quadrature-signals from both the dq voltage components in the stationary reference frame. Each SOGI block gives rise to the quadrature signals of the dq components separately, and its schematic can be seen in Figure 3.13. In this figure, ω and k are, respectively, the frequency and damping factor whose value used is $\sqrt{2}$, as it presents good results.
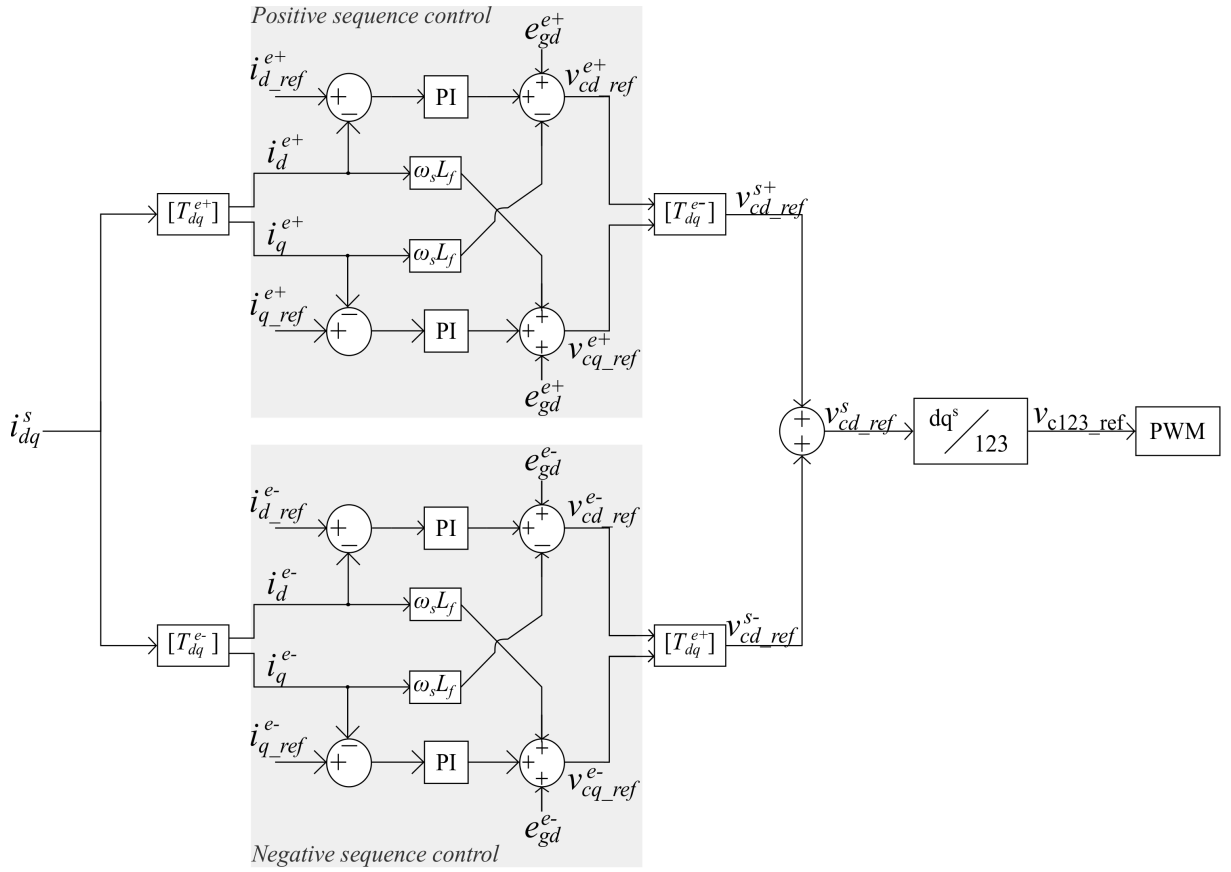
Figure 3.11 – Double Synchronous Reference Frame structure
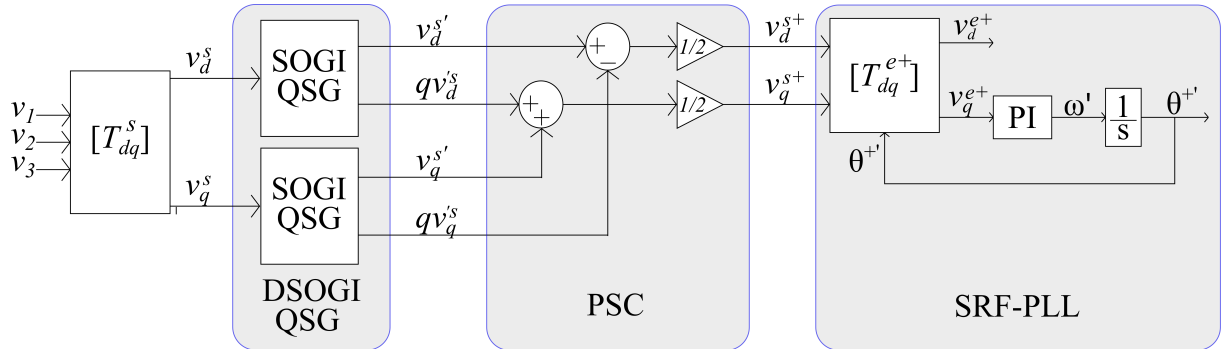
Figure 3.12 – DSOGI-PLL's block diagram
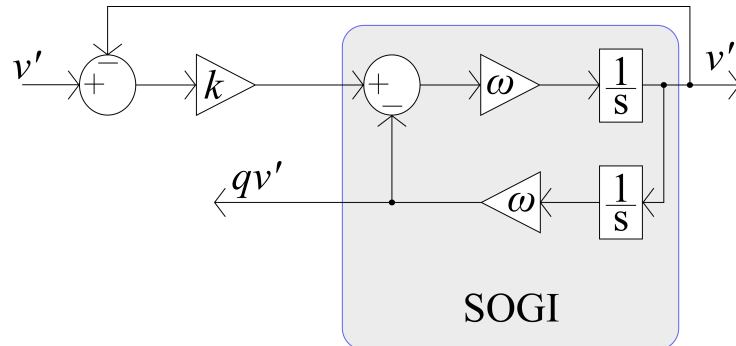
Figure 3.13 – SOGI block diagram

- Positive-Sequence Calculator (PSC): it calculates the positive-sequence components by using the quadrature signals from the DSOGI-QSG block. The relation between the original quadrature signals and the positive-sequence components is gigen by the following expression

$$v_{dq}^{s+} = \begin{bmatrix} v_d^{s+} \\ v_q^{s+} \end{bmatrix} = \frac{1}{2} \begin{bmatrix} 1 & -q \\ q & 1 \end{bmatrix} v_{dq}^s \tag{3.67}$$

where $q = e^{-j\frac{\pi}{2}}$.

From this positive-sequence component, it is possible to obtain the negative-sequence component using the following relation

$$v_{dq}^{s-} = v_{dq}^s - v_{dq}^{s+} \tag{3.68}$$

- Syncronous Reference Frame and Phase Locked Loop (SRF-PLL): This system tracks grid frequency and, therefore, the angle used in the Park transform. It needs to use the signals in DQ coordinates, so its first block does this transformation. The feedback loop adjusts the q component in the positive synchronous frame to zero, controlling the angular position and determining the grid frequency. Besides, this block has a change reference frame at the begining, as the input signals are in the stationary frame. The relation between the stationary and synchronous reference frames are given by

$$v_{dq}^{e+} = \begin{bmatrix} v_d^{e+} \\ v_q^{e+} \end{bmatrix} = \begin{bmatrix} T_{dq}^{e+} \end{bmatrix} v_{dq}^{s+} \tag{3.69}$$

$$v_{dq}^{e-} = \begin{bmatrix} v_d^{e-} \\ v_q^{e-} \end{bmatrix} = \begin{bmatrix} T_{dq}^{e-} \end{bmatrix} v_{dq}^{s-} \tag{3.70}$$

where

$$\begin{bmatrix} T_{dq}^{e+} \end{bmatrix} = \begin{bmatrix} cos\theta^+ & sin\theta^+ \\ -sin\theta^+ & cos\theta^+ \end{bmatrix} \tag{3.71}$$

$$\begin{bmatrix} T_{dq}^{e-} \end{bmatrix} = \begin{bmatrix} cos\theta^+ & -sin\theta^+ \\ sin\theta^+ & cos\theta^+ \end{bmatrix} \tag{3.72}$$

and θ^+ is the tracked angle from SRF-PLL.

3.4.3   Outer loop for control voltage

In the balanced power grid model, the outer loop block for DC-link voltage control provides the reference current for the inner loop current control. However, other variables must be taken into account, as there are other conditions that must be met in an unbalanced

scenario. The emerging oscillations in the active and reactive powers are examples of these variables because when injecting such quantities imbued with these disturbances, the control might be affected. Then, to solve this issue, the authors in (TEODORESCU; LISERRE; RODRIGUEZ, 2011) present an outer loop control that served as inspiration for the one applied in this work.

Figure 3.14 shows the new outer loop for DC link control. This loop now provides the reference active power for the current control inner loop, i.e., it provides the power signal used to calculate the reference currents developed in the control strategies section.
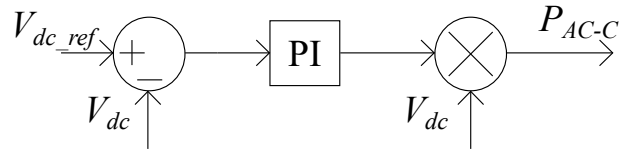
Figure 3.14 – Block diagram of the DC-link voltage outer loop

3.5   CONCLUSION

In this chapter, the control system for the on-grid PV system was presented. In this way, the control strategies for the unbalanced power grid were presented based on the current expressions developed in the system model chapter, in which they aim to: inject balanced currents into the grid (strategy 1), reduce oscillations in the active power (strategy 2), and reduce oscillations in reactive power (strategy 3). Besides, the control structure fully developed is composed of two loops, one for the DC-link voltage and the other for the injected currents. In the first moment, a balanced power grid was considered, in which the external DC-link voltage control loop provided the reference signal for the inner current control loop, specifically for the d coordinate of this quantity. This inner loop regulates the current magnitude and provides the signal triggers for the inverter switches, i.e., it served as a reference for the PWM. However, the unbalance in the grid resulted in changes in the control loops. Thus, the control loop started to provide an active power reference signal for the current control inner loop based on DSRF. This control method uses two control structures, one for controlling the positive component and the other for controlling the negative component. Also, the structure of the PLL for synchronization and the detection model for sequence components of the quantities called DSOGI-PLL were shown.

4 SIMULATION RESULTS

4.1 INTRODUCTION

The steady state results of simulations performed in MATLAB/SIMULINK® with two main simulation scenarios are shown in this chapter. The first scenario presents an electrical grid fully balanced with the PV system injecting power according to the conventional strategy, which does not consider the symmetrical components. On the other hand, the second scenario has the electrical grid unbalanced due to the irregular load distribution among the phases. Also, there's a fault leading to voltage sags, whose voltage phasors are inserted in the simulations by changing the primary power source voltages according to the sag characteristics. In this scenario, the PV system injects power into the grid running all four strategies: conventional, 1, 2, and 3.

4.2 BALANCED SCENARIO

The grid starts with the power source on the medium voltage side with 13.8 kV. It continues with a three-phase transformer Δ-Y delta-star of 150 kVA of power with a transformation ratio of 13.8 kV / 380 V, which is responsible for lower the voltage. Its other parameters are the default parameters of the MATLAB/SIMULINK® transformer model, except for the voltages that were adjusted to those previously described. It also presents impedances along its lines, where each line separating the buses has a resistance of 0.975 Ω/km, R/X = 100 ratio, and 40 meters in length. The first scenario is for a balanced grid, thus, the loads are evenly distributed among the grid phases that supply individually 44 kVA with a unity power factor, as shown in Table 4.1, which also displays other parameters. In addition, Table 4.2 shows the loads distributed on each bus in the system, and Table 4.3 shows the PV parameters. The design of the system is shown in Figure 4.1.

Table 4.1 – Power grid parameters for balanced scenario

Parameter	Value
Line voltage	380 V
Phase voltage	220 V
R/X ratio	100
Line resistance	0.975 Ω/km
Frequency	60 Hz
Loads in phase 1	44 kVA
Loads in phase 2	44 kVA
Loads in phase 3	44 kVA

First, the PV system is connected to the electrical grid along bus 5, and the results are obtained to verify its performance in active power injection and control system

Table 4.2 – Loads on the buses

Bus	1ϕ	3ϕ
B1	-	-
B2	-	-
B3	3x8 kVA	18 kVA
B4	3x8 kVA	-
B5	-	18 kVA
B6	3x8 kVA	-
B7	3x8 kVA	-

Table 4.3 – PV system parameters

Parameters	Value
Panels per string	5
Number of strings	10
Panel rated power	400 W$_\text{p}$
Array rated power	20 kW$_\text{p}$
DC-link voltage	1200 V
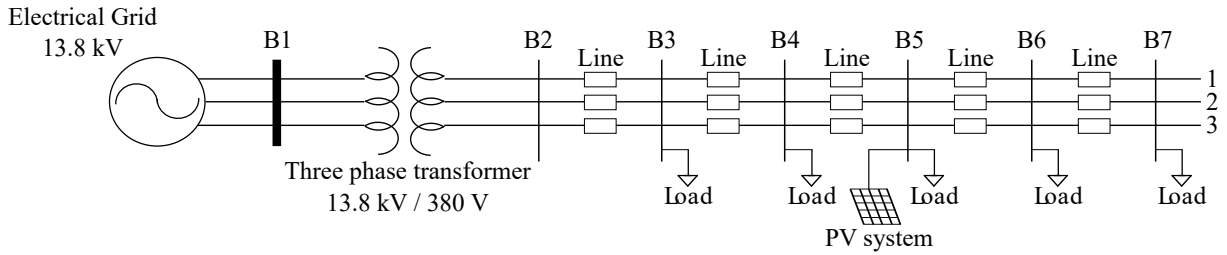
Figure 4.1 – Power grid configuration

functioning. Then, the simulation is done with the PV system connected to bus 7. In other words, there is one set of results when the PV system is connected to bus 5, and one set of results when this system is connected to bus 7. The PV parameters are presented in Table 2.1.

4.2.1 Conventional strategy

At this opening moment, the system is all balanced, and there are two different connections of the PV system into the grid, which means there are two separate simulations to execute: 1) it is connected to bus 5, and 2) to bus 7. The voltage signals can be seen in Figures 4.2 (a) and (b) for both scenarios, whose root means square (RMS) value is 207 V (connection at bus 5) and 205 V (connection at bus 7). The resulting tiny difference happens due to the electrical line impedance that causes a voltage drop along the line. The three-phase current signals injected into the grid by the PV system connected to buses 5 and 7, respectively, are shown in Figures 4.2 (c) and (d). The RMS values of the currents shown in these figures and the curves demonstrate that this quantity is balanced, as the voltages, which was expected for the scenario presented here.

Figure 4.2 – Simulation results for balanced scenario and conventional strategy. (a) Three-phase voltages at bus 5. (b) Three-phase voltages at bus 7. (c) Injected currents into the grid by the PV system in bus 5. (d) Injected currents into the grid by the PV system in bus 7.

The results found for the input voltage and current of the PV array can be seen in Figures 4.3 (a) and (b), whose regulation is performed by a boost converter with the MPPT *P&O* technique. Both scenarios have the same behaviors, so only results for the PV system connected to bus five (5) are shown. The values shown in these figures are 203 V and 98 A for the voltage and current at the maximum power point. They are justified by the parallel association of 10 strings composed of 5 panels connected in series with individual values for voltage and current at the maximum power point are 40.7 V and 9.83 A, respectively. These values for current and voltage meet the rated power of the arrangement, which is 20 kW and indicates the adequate performance of the MPPT. In addition, the DC-link voltage at the input of the three-phase inverter can be seen in Figures 4.3 (c) and (d). Although the quantity (blue - V_{cc}) takes a while to stabilize at the desired reference value (red - V_{cc-ref}) of 1200 V when compared to the other strategies, the DC-link voltage control manages to operate correctly.

It is noteworthy that the voltage controller produces a signal with an electrical magnitude of current, which is the reference current for the d coordinate, and the current controller produces a signal with an electrical magnitude of voltage that is necessary for the inverter modulation. The current signal in the coordinate d and its reference calculated from the external DC voltage control loop can be seen in Figures 4.4 (a) and (b) for PV system connected at buses 5 and 7, respectively. Besides, the current signal at the q coordinate must be zero, as it represents the reactive component of the current and

Figure 4.3 – Simulation results for balanced scenario and convetional strategy. (a) PV array input voltage. (b) PV array input current. (c) DC-link voltage for PV system in bus 5. (d) DC-link voltage for PV system in bus 7.

the desire here is not the injection of reactive power. Thus, the current reference in the q coordinate of the current is set to zero, as shown in Figures 4.4 (c) and (d).

Figures 4.5 (a) and (b) show the active power delivered to the grid by the PV system connected to buses 5 and 7. The quantity doesn't show any deformations for both connection scenarios, which goes as expected. In addition, Figures 4.5 (c) and (d) exhibit the reactive power, which is zero because there is no injection of this electrical quantity.

4.3   UNBALANCED SCENARIO

The parameters used in the unbalanced scenario are similar to the previous one. One of the main changes is the load distribution among the phases, which is now irregular and provokes a small unbalance in the system. The irregular load distribution is done as follows: phases 1, 2, and 3 supply 38.16 kVA, 44.16 kVA, and 45.16 kVA with a power factor of 0.92, respectively, as can be seen in Table 4.4. The load distribution per bus is shown in Table 4.5. Besides, an alleged fault in phase 2 of the mains transformer caused the shutdown of that phase to create a greater unbalance.

In addition, the voltages of the three-phase electrical grid are also unbalanced to create a scenario of unbalance more suitable for the tests, allowing to verify the operation of the adopted control strategies and the control system in general. It was considered a hypothetical fault that would lead to a type D sag as shown in Table 4.6 (see Table 1.1 for all the sags). Also, the phasor selected for the pre-fault phasor is $\vec{E} = 13.8\angle 0°$ kV and

Figure 4.4 – Simulation results for balanced scenario and conventional strategy. (a) d component of the measured current and its reference (connection at bus 5). (b) d component of the measured current and its reference (connection at bus 7). (c) q component of the measured current and its reference (connection at bus 5). (d) q component of the measured current and its reference (connection bus 7).

Figure 4.5 – Simulation results for balanced scenario and conventional strategy. (a) Active power injected into the grid by the PV system (connection at bus 5). (b) Active power injected into the grid by the PV system (connection at bus 7). (c) Reactive power injected into the grid by the PV system (connection at bus 5). (d) Reactive power injected into the grid by the PV system (connection at bus 7).

Table 4.4 – Power grid parameters for unbalanced scenario

Parameter	Value
Line voltage	380 V
Phase voltage	220 V
Frequency	60 Hz
Phase 1 loads	38.16 kVA
Phase 2 loads	44.16 kVA
Phase 3 loads	45.16 kVA

Table 4.5 – Loads on the buses for unbalanced scenario

Bus	1ϕ	3ϕ
B1	-	-
B2	-	-
B3	2x7 kVA, 8.5 kVA	17 kVA
B4	5 kVA, 10 kVA, 12.5 kVA	-
B5	-	18 kVA
B6	6 kVA, 6 kVA, 7.5 kVA	-
B7	8 kVA, 8 kVA, 6 kVA	-

the voltage sag during the fault is $\vec{V} = 0.5\vec{E}$. The grid frequency during the fault is 60 Hz. Thus, the primary source input voltages during the voltage sag are given by

$$E_{g1} = V_1 = 6,9\angle 0° \tag{4.1}$$

$$E_{g2} = V_2 = 12,4391\angle{-106.1°} \tag{4.2}$$

$$E_{g3} = V_3 = 12,4391\angle 106.1° \tag{4.3}$$

Table 4.6 – Type D sag

Type	V_1	V_2	V_3
D	$\vec{V}$	$-\dfrac{1}{2}\vec{E} - j\sqrt{3}\dfrac{1}{2}\vec{V}$	$-\dfrac{1}{2}\vec{E} + j\sqrt{3}\dfrac{1}{2}\vec{V}$

It is possible to find the voltage unbalance factor n, which is an important index used to measure the unbalance degree in the electrical grid. This index is defined by the percentage ratio between the magnitudes of the negative (V^-) and positive (V^+) sequence components of the voltage (MIRET et al., 2012), i.e.,

$$n = \frac{V^-}{V^+} \tag{4.4}$$

Hence, from the phase voltages shown in expressions (4.1) - (4.3), the magnitudes

of the positive and negative elements are calculated using the Fortescue theorem, as follows

$$V^+ = \frac{1}{3}(V_1 + \alpha V_2 + \alpha^2 V_3) \tag{4.5}$$

$$V^- = \frac{1}{3}(V_1 + \alpha^2 V_2 + \alpha V_3) \tag{4.6}$$

where $\alpha = e^{j\frac{2\pi}{3}}$. Thus, it gives the following result for the unbalance factor

$$n = \frac{V^-}{V^+} = \frac{3,450.19}{10,349.89} = 0.333$$

The definition of voltage phasors for the primary power source of the grid close the unbalanced scenario for the simulations with all the strategies studied here. The grid source voltages are shown in Figure 4.6 and are used in all the simulations performd. The results found for the main electrical quantities for analysis are shown below.
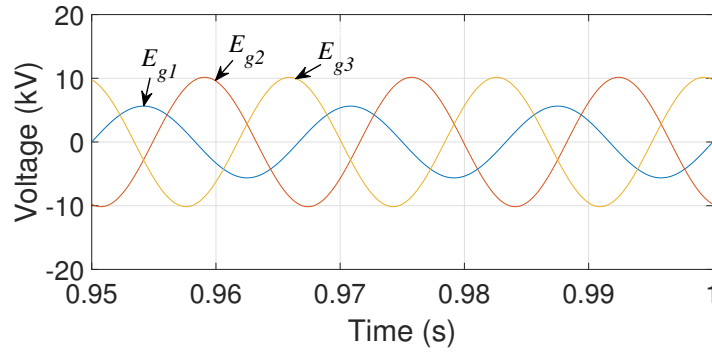
Figure 4.6 – Voltages for the primary power source of the grid under a type D sag

4.3.1 Conventional control strategy

The first results shown are for the conventional current control, and the only modification made is for the power grid voltages that are now unbalanced. Hence, the same parameters of the PV system are kept from the previous section for comparison. The three-phase voltage on the PV system connection in bus 5 and 7 are illustrated in Figure 4.7 (a) and (b) that indicate unbalanced voltages with divergent RMS values, as expected. In addition, Figure 4.7 (c) and (d) show the currents injected by the PV system into the grid with the respective RMS values. Note from this figure that the current is now totally unbalanced and unregulated due to the presence of negative sequence components that interfere with the action of the control system.

There were no changes in the PV system, so the PV input quantities remain in the same form. Figures 4.8 (a) and (b) show the results for the input voltage and current of the PV system, which remain the same, as there were no changes in the MPPT or any other parameter that directly influences the PV array. The DC-link voltage control works
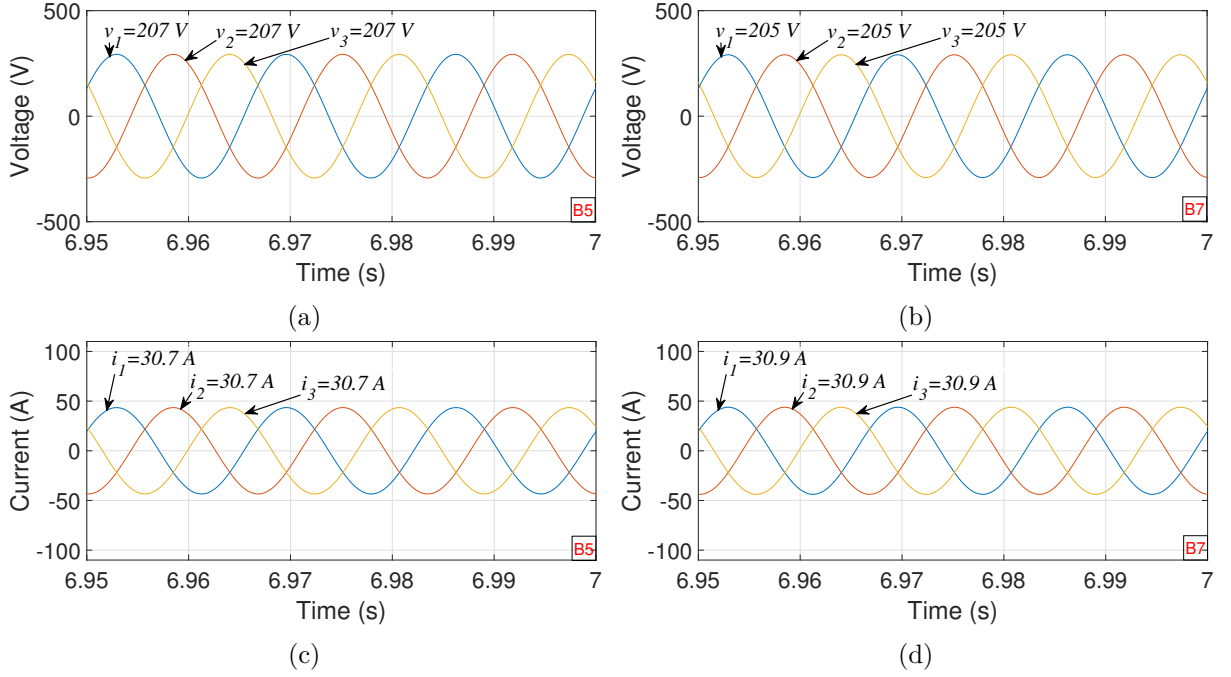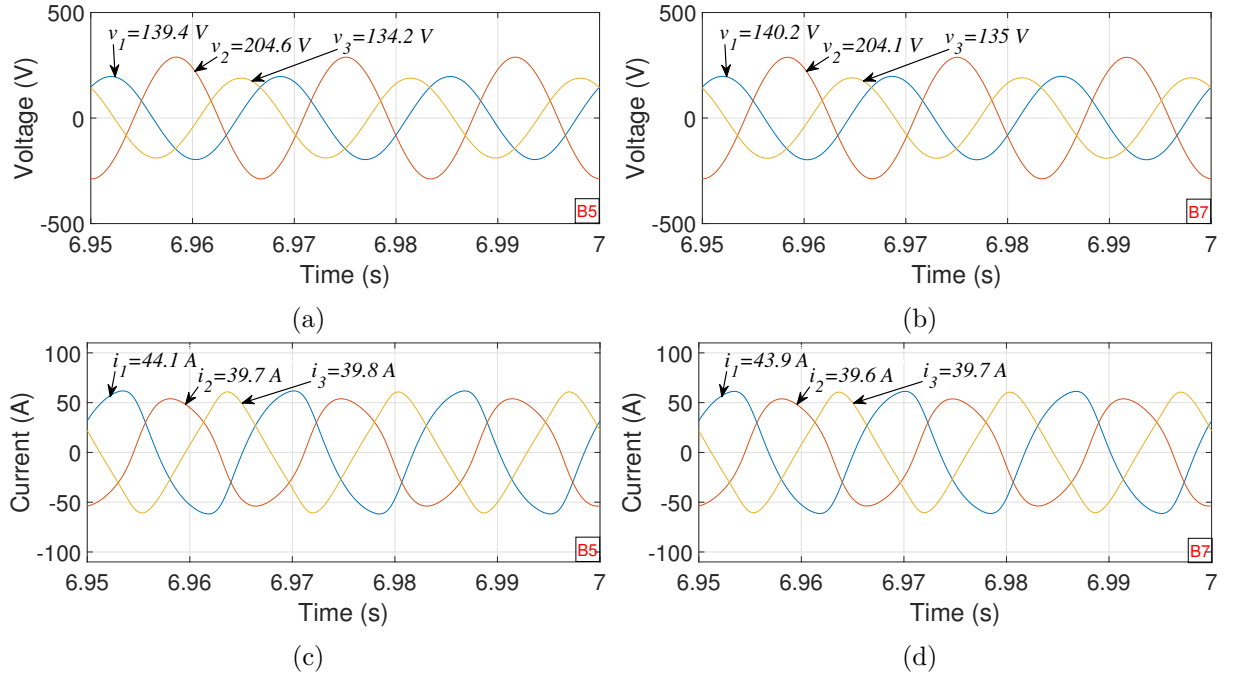
Figure 4.7 – Simulation results for unbalanced scenario and convetional strategy. (a) Three-phase voltages at bus 5. (b) Three-phase voltages at bus 7. (c) Injected currents into the grid by the PV system in bus 5. (d) Injected currents into the grid by the PV system in bus 7.
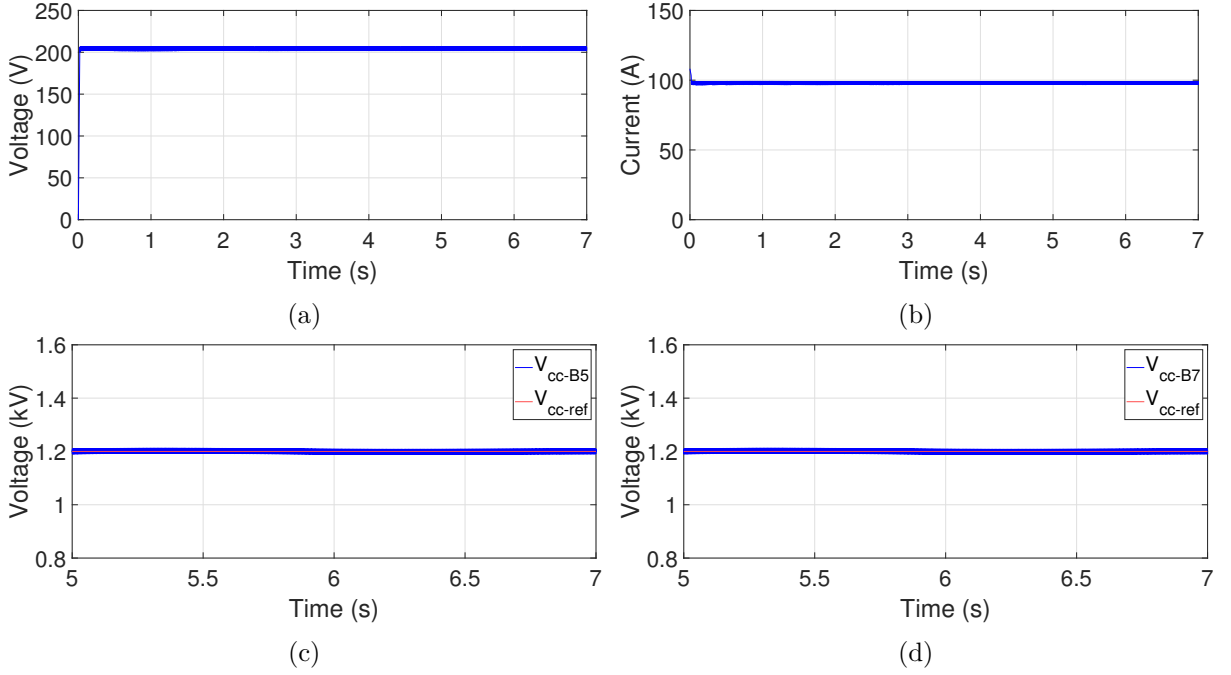

Figure 4.8 – Simulation results for unbalanced scenario and convetional strategy. (a) PV array input voltage. (b) PV array input current. (c) DC-link voltage for bus 5. (d) DC-link voltage for bus 7.

slowly, like for the balanced scenario, but it regulated the quantity, as shown in Figures 4.8 (c) and (d) for the PV connection in buses 5 and 7.

The controlled current signals (current injected into the grid) in the *dq* synchronous reference and their references can be seen in Figures 4.9 (a) and (c) for the PV system connected to bus 5 and Figures 4.10 (a) and (c) when it is at bus 7. These are the control signals of the current distorted due to the presence of the negative sequence components. Figures 4.9 (c) and (d), and 4.10 (c) and (d) detail the oscillations in the *dq* current due to the unbalance when buses 5 and 7 have the PV system connected to them.
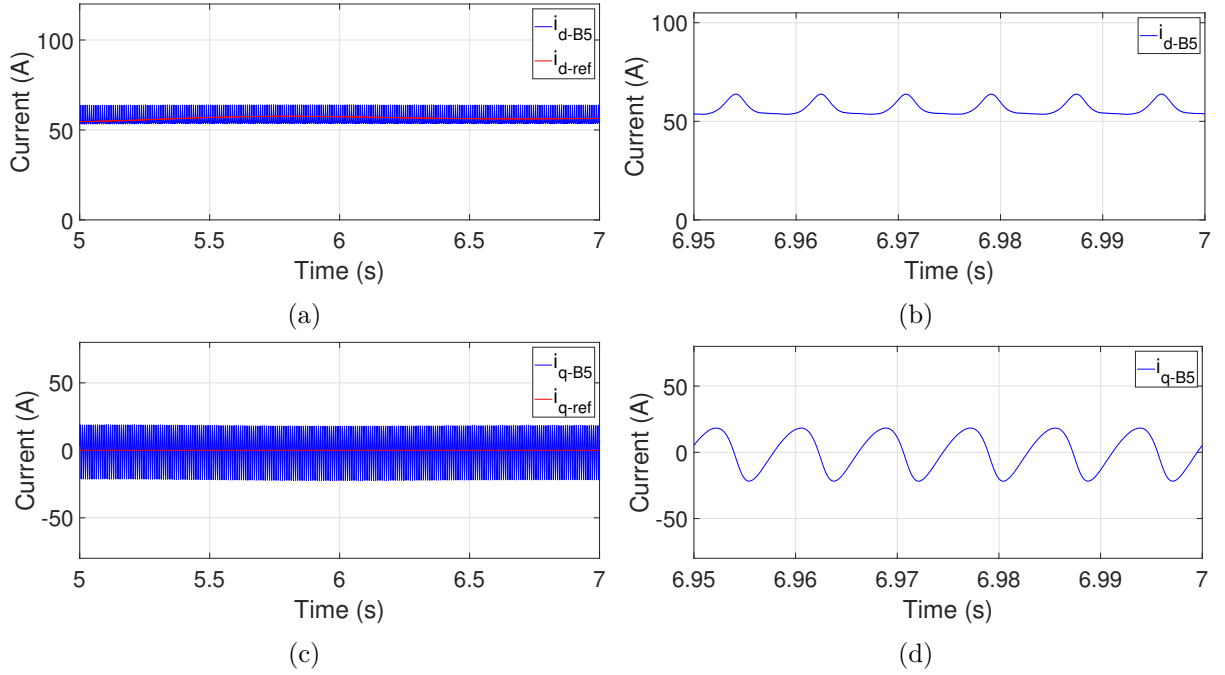
Figure 4.9 – Simulation results for unbalanced scenario and convetional strategy (bus 5). (a) *d* component of the measured current and its reference. (b) *d* component in smaller range to highlight oscillations. (c) *q* component of the measured current and its reference. (d) *q* component in smaller range to highlight oscillations.

Active and reactive powers also have oscillations in their wave shapes due to the negative sequence components, just like the *dq* current signals. Thus, these oscillations can be seen in Figures 4.11 (a) and (b) for the injected active power of the PV system connected to buses 5 and 7, respectively, and (c) and (d) for the reactive power of PV system for the same connection set.

4.3.2 Strategy 1

The objective of strategy 1 is to eliminate the negative components of the current originated from the unbalances in the grid. So, the first results are related to the PV system, where Figures 4.12 (a) and (b) show the input voltage and current of this system, which remain the same as before because of there's no change in the PV array.
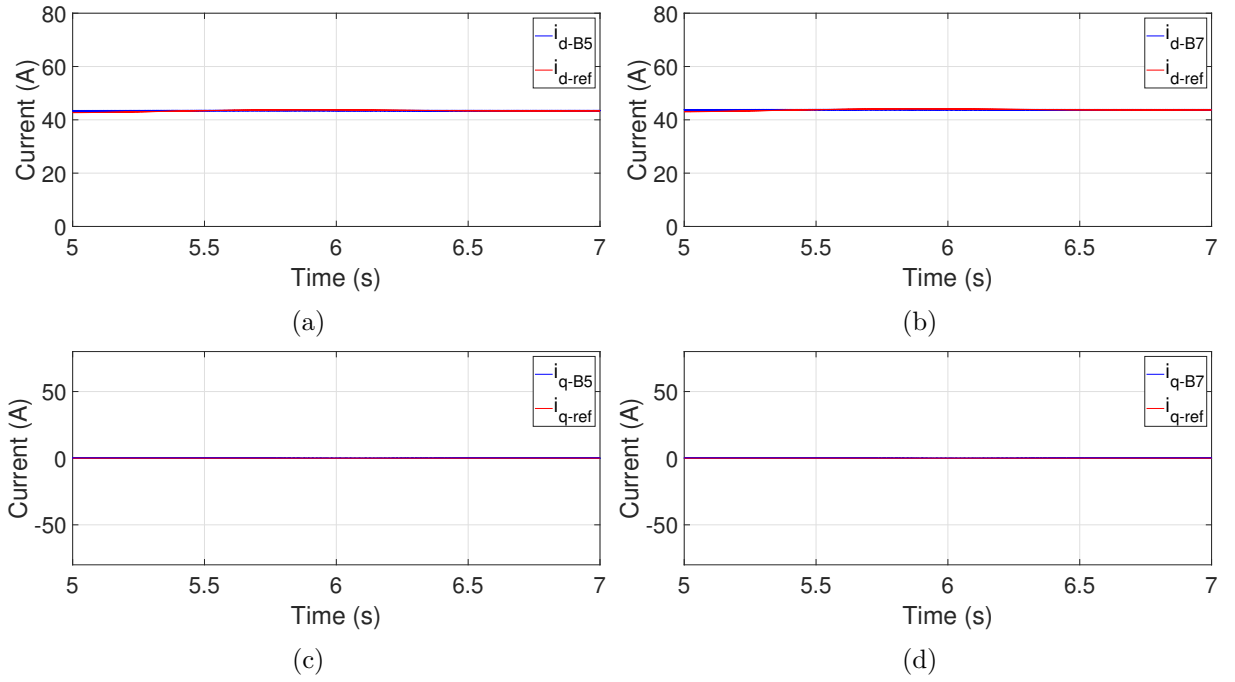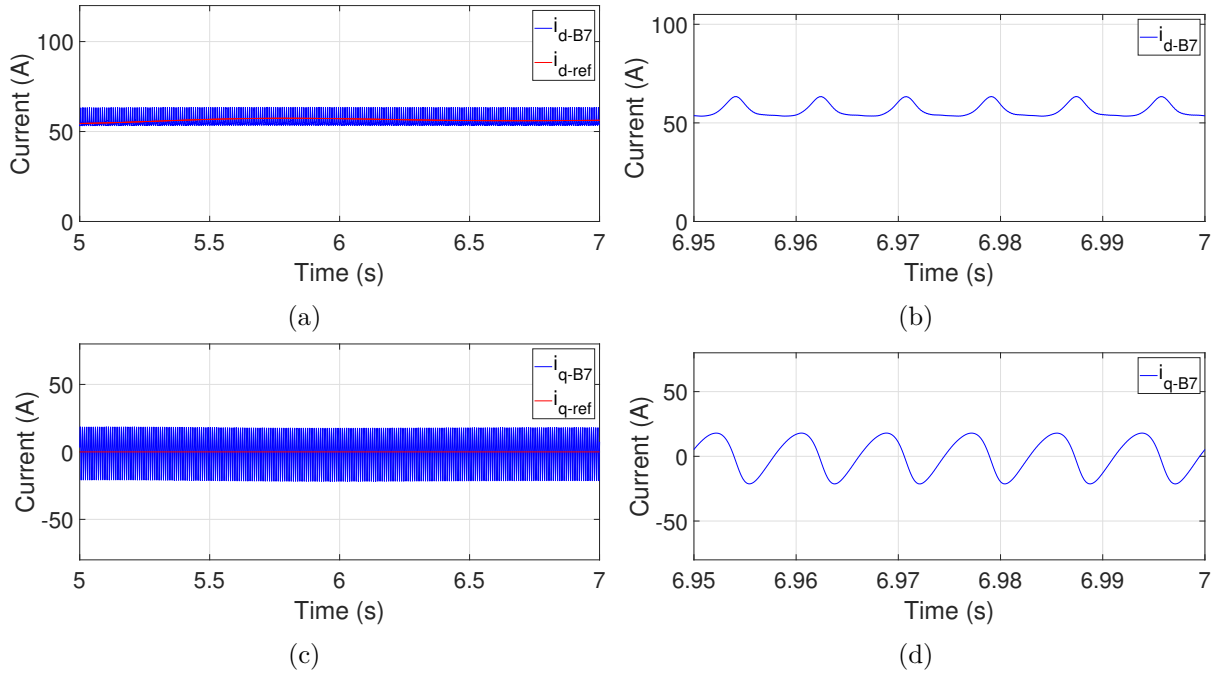
Figure 4.10 – Simulation results for unbalanced scenario and convetional strategy (bus 7). (a) d component of the measured current and its reference. (b) d component in smaller range to highlight oscillations. (c) q component of the measured current and its reference. (d) q component in smaller range to highlight oscillations.
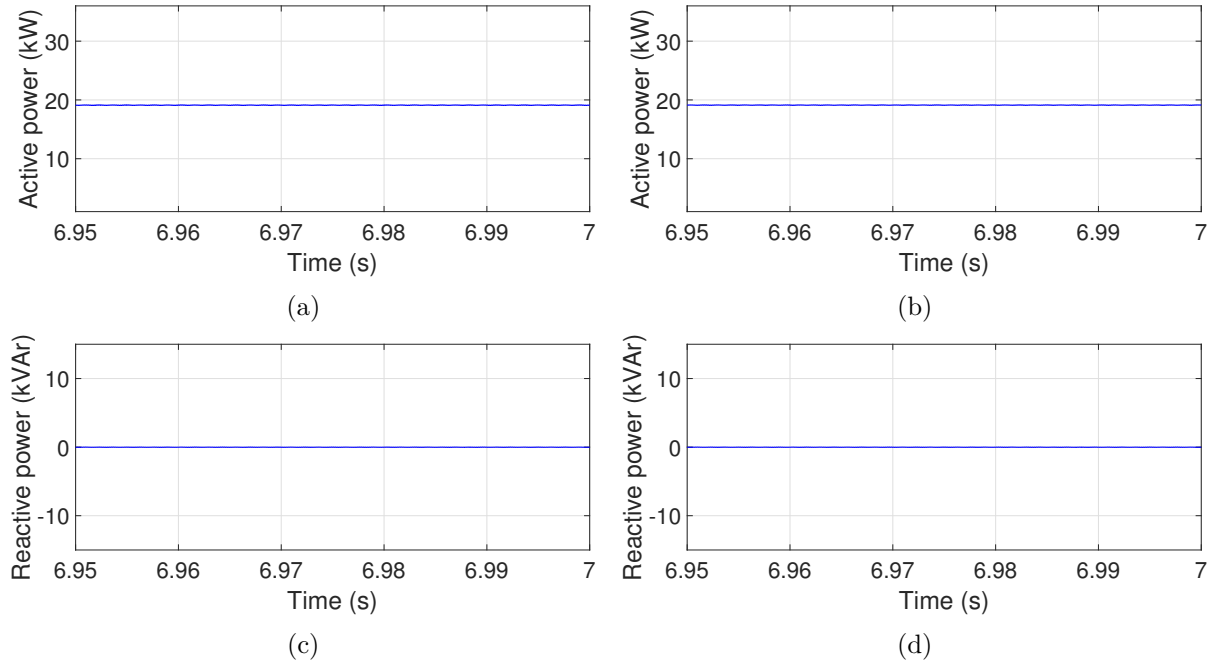

Figure 4.11 – Simulation results for unbalanced scenario and convetional strategy. (a) Active power injected into the grid by the PV system (bus 5). (b) Active power injected into the grid by the PV system (bus 7). (c) Reactive power injected into the grid by the PV system (bus 5). (d) Reactive power injected into the grid by the PV system (bus 7).
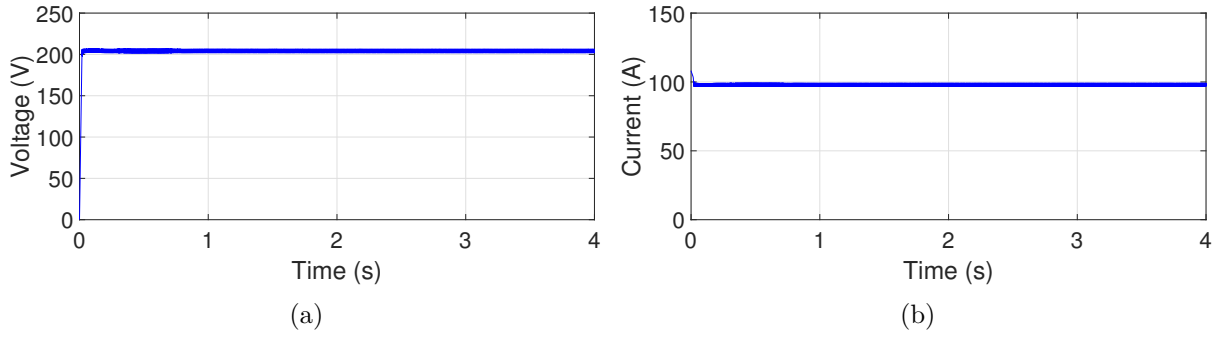
Figure 4.12 – Simulation results for unbalanced scenario and strategy 1. (a) PV array input voltage. (b) PV array input current.

The DC-link voltage for the PV system can be seen in Figure 4.13 (a) (connection at bus 5) and (b) (connection at bus 7), whose behaviors indicate that the control works perfectly, as 1200 V is the desired and reached value for the quantity. Besides, the current injected by the PV system is shown in Figures 4.13 (c) and (d) for the connection at buses 5 and 7. These figures suggest that the current is fully balanced, indicating that the main objective of strategy 1 has been achieved.
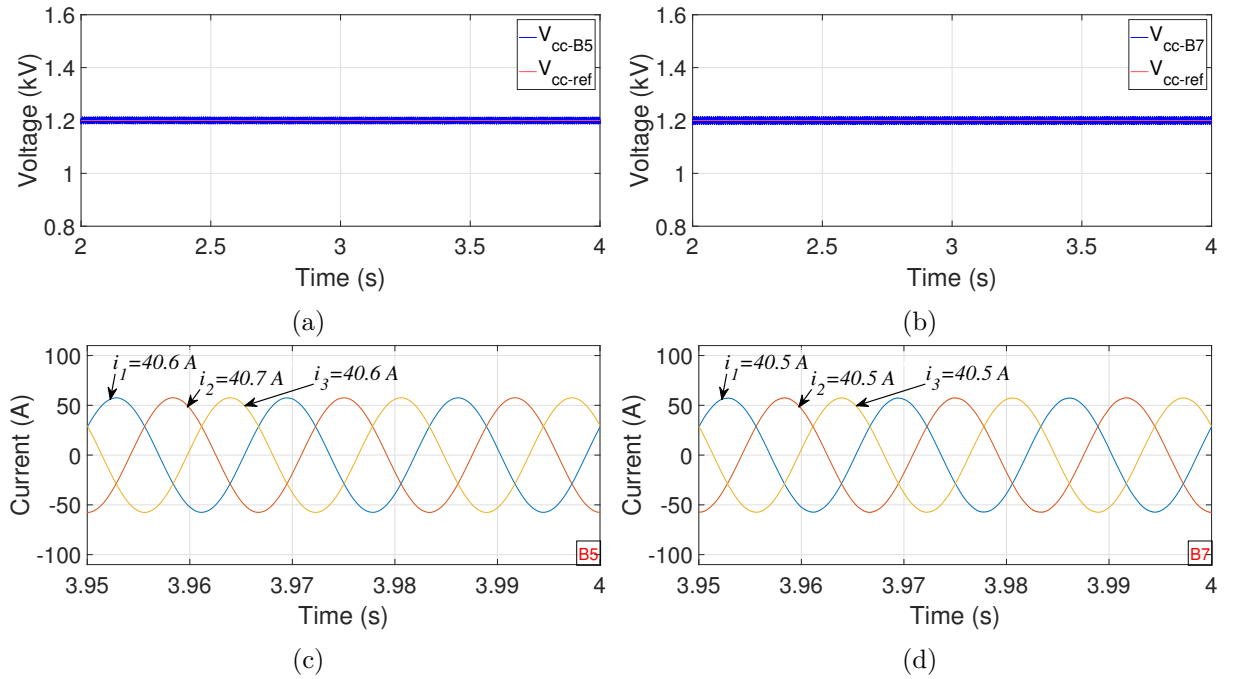
Figure 4.13 – Simulation results for unbalanced scenario and strategy 1. (a) DC-link voltage and its reference for PV system connected at bus 5. (b) DC-link voltage and its reference for PV system connected at bus 7. (c) Three-phase current injected into the grid by the PV system connected at bus 5. (d) Three-phase current injected into the grid by the PV system connected at bus 7.

The signals of the positive and negative components of the current are shown to observe the behavior of the inner current control based on DSRF. First, Figures 4.14 (a) and (b) for connection at bus 5, and 4.15 (a) and (b) for bus 7 show the positive components of the current in the synchronous reference frame of the grid voltage. These

figures point to a correct work of the control system as the controlled signals follow the imposed references. Also, the main focus of strategy 1 is to eliminate the negative components of the current so that the injected current is balanced, and as can be seen in Figures 4.14 (c) and (d) for connection at bus 5, and 4.15 (c) and (d) for connection at bus 7, these signals are regulated to zero, implying a good functioning of the control system and, consequently, of the proposed control strategy.

Figure 4.14 – Simulation results for unbalanced scenario and strategy 1 (connection at bus 5). (a) d positive-sequence component of the current. (b) q positive-sequence component of the current. (c) d negative sequence component of the current. (d) q negative sequence component of the current.

It is possible to observe the active power delivered to the grid by the PV system connected to buses 5 and 7, respectively, in Figures 4.16 (a) and (b). These figures suggest an increase in the oscillation in this quantity compared to the conventional strategy presented in the previous topic. Furthermore, the reactive power has almost the same behavior as the conventional control, as shown in Figures 4.16 (c) and (d) for PV system connection at bus 5 and 7, showing a similar pattern in the oscillations.

4.3.3 Strategy 2

The target of strategy 2 is the amortization of the active power oscillations. Starting with the results for the PV system, Figures 4.17 (a) and (b) display, respectively, the input voltage and current of the PV array for both buses and they keep the same as the previous ones since there's no change in the power source.

The DC-link voltage for PV connected to buses 5 and 7 is shown in Figures 4.18 (a) and (b). Note that the control operates correctly in this quantity since the magnitude

Figure 4.15 – Simulation results for unbalanced scenario and strategy 1 (connection at bus 7). (a) d positive-sequence component of the current. (b) q positive-sequence component of the current. (c) d negative sequence component of the current. (d) q negative sequence component of the current.

Figure 4.16 – Simulation results for unbalanced scenario and strategy 1. (a) Active power injected into the grid by the PV system for PV system connected at bus 5. (b) Active power injected into the grid by the PV system for PV system connected at bus 7. (c) Reactive power injected into the grid by the PV system for PV system connected at bus 5. (d) Reactive power injected into the grid by the PV system for PV system connected at bus 7.
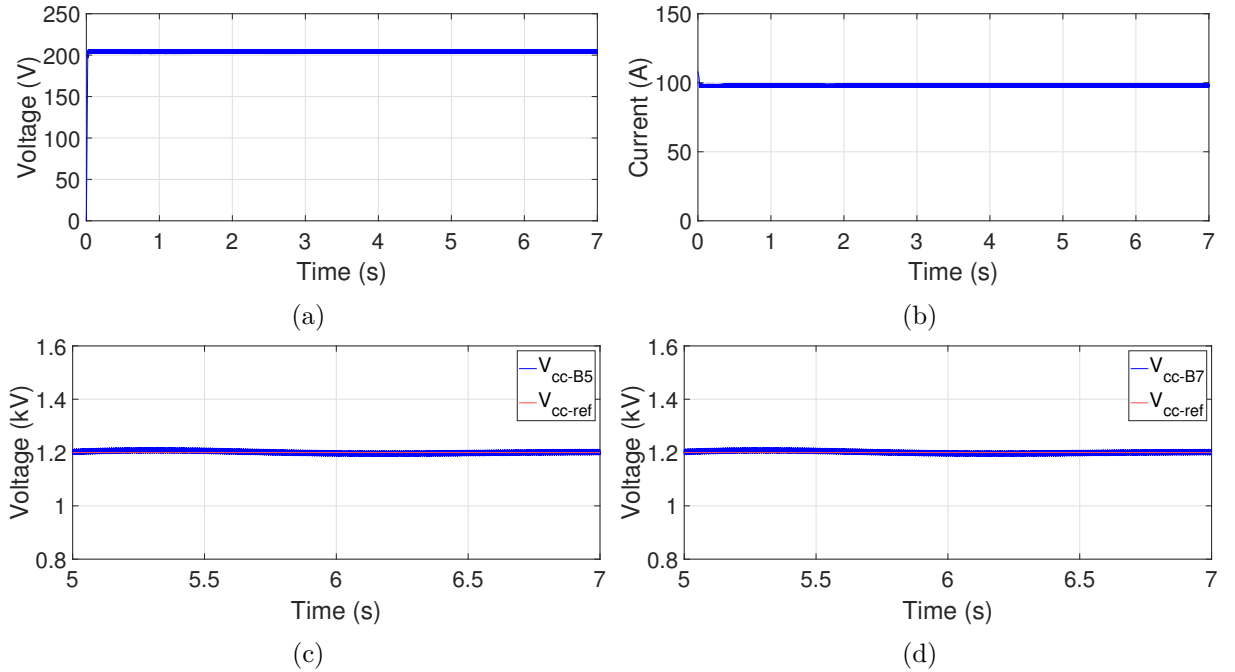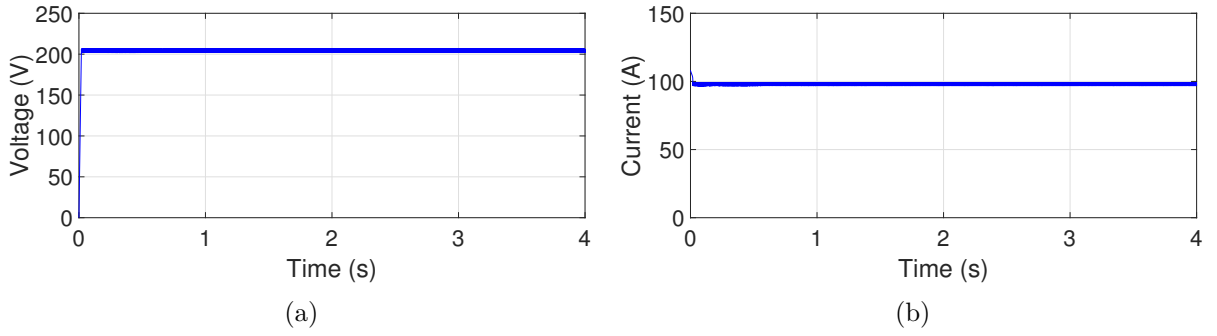
Figure 4.17 – Simulation results for unbalanced scenario and strategy 2. (a) PV array input voltage. (b) PV array input current.

voltage is 1200 V, whose value is the reference established at work. Besides, Figures 4.18 (c) and (d) display the three-phase current injected by the PV system connected to buses 5 and 7, which is the other controlled quantity. Despite keeping the clean sinusoidal shape shown in the figures, the currents have angular phase and magnitude divergences since the control objective is the active power.
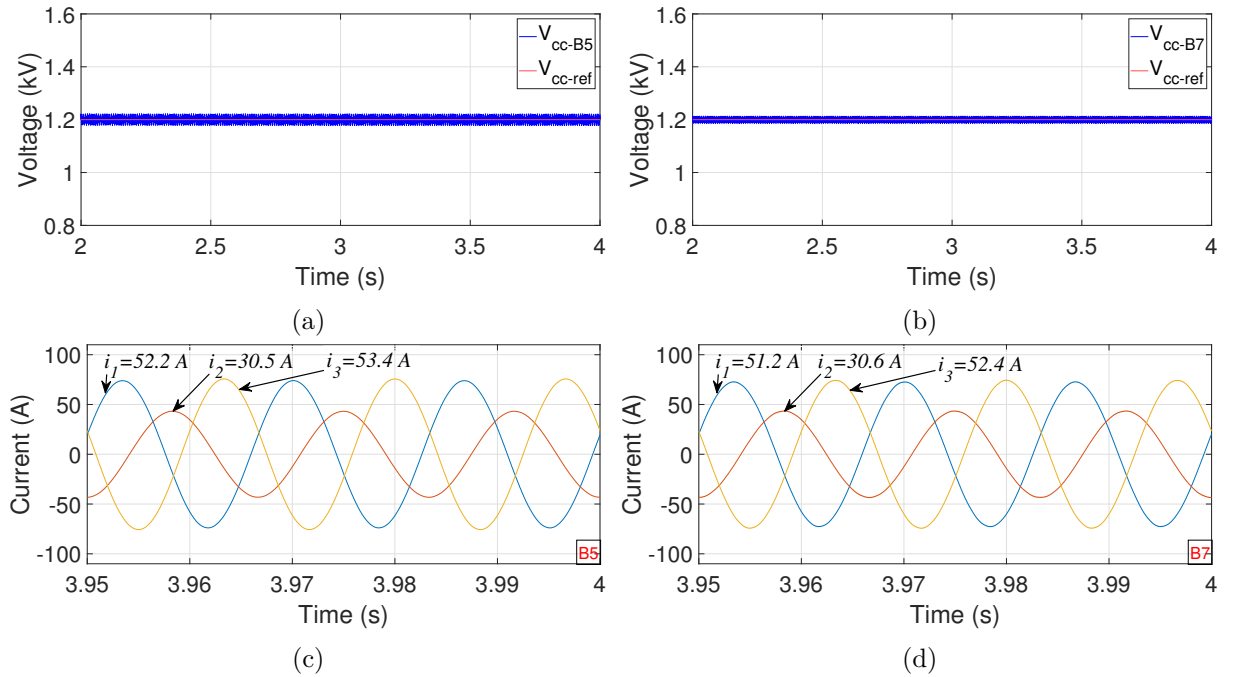
Figure 4.18 – Simulation results for unbalanced scenario and strategy 2. (a) DC-link voltage and its reference for PV system connected at bus 5. (b) DC-link voltage and its reference for PV system connected at bus 7. (c) Three-phase current injected into the grid by the PV system connected at bus 5. (d) Three-phase current injected into the grid by the PV system connected at bus 7.

The positive components of the current are shown in Figures 4.19 (a) and (b) for PV system connected to bus 5 and 4.20 (a) and (b) for PV system connected to bus 7, which show that the controllers were able to regulate these quantities according to the imposed references. Figures 4.19 (c) and (d), and 4.20 (c) and (d) show the negative components of the current, in which the controllers could regulate them according to the

imposed references. Besides, a notable difference between strategies 1 and 2 is that the negative components in the first are set to null since the objective is to eliminate them, while in the second they are different from zero, being adjusted according to the desire that is the reduction of active power oscillations.
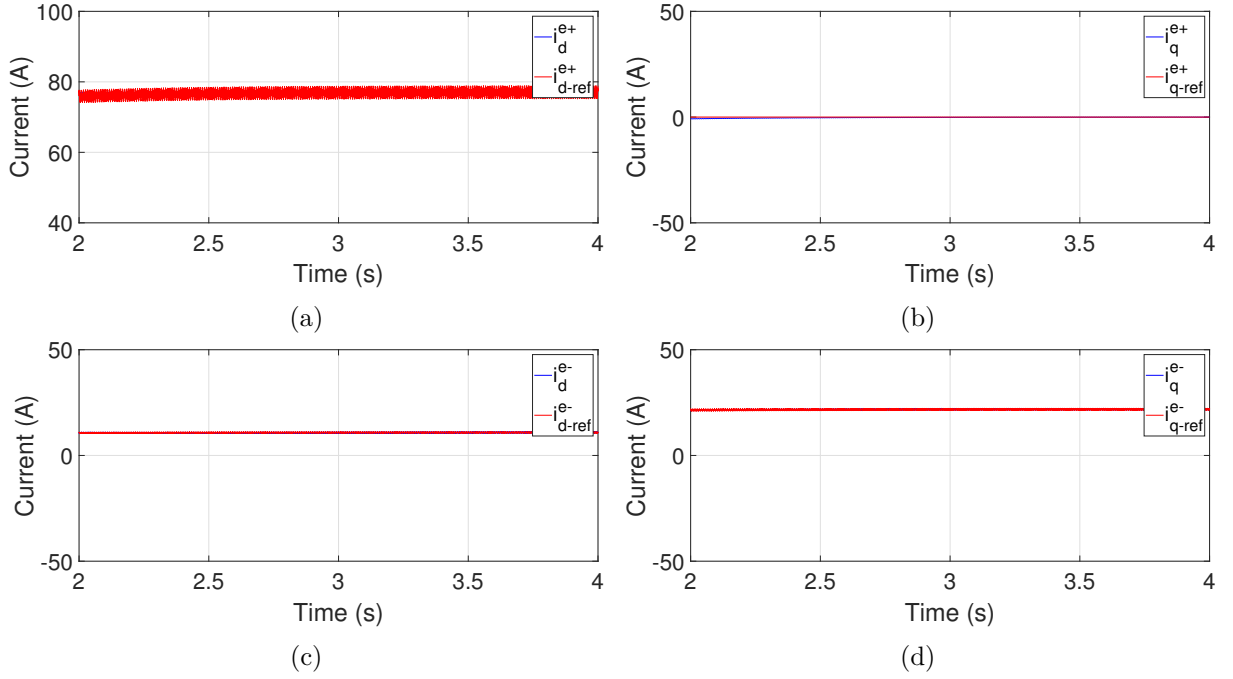
Figure 4.19 – Simulation results for unbalanced scenario and strategy 2 (connection at bus 5). (a) d positive-sequence component of the current. (b) q positive-sequence component of the current. (c) d negative sequence component of the current. (d) q negative sequence component of the current.

The active power delivered to the grid is the main target of control strategy 2 and it is displayed in Figures 4.21 (a) (connection at bus 5) and 4.21 (b) (connection at bus 7). From these figures, it is noted that the active power oscillations have dramatically decreased when compared to those results presented in the two strategies seen so far. And this is the expected comportment for this quantity since the focus of strategy 2 is to reduce these oscillations. On the other hand, the reactive power presents oscillations, as shown in Figures 4.21 (c) (bus 5) and 4.21 (d) (bus 7), once the control focus is not such a quantity.

4.3.4 Strategy 3

The same simulation conditions are maintained for strategy 3, whose target is the amortization of oscillations in reactive power. Figures 4.22 (a) and (b) show the results for the input voltage and current of the PV array, respectively. There's no changes in these quantities for strategy 3 because of the PV array characteristics were kept.

Figures 4.23 (a) and (b) display the DC-link voltage of the PV system connected to buses 5 and 7. The voltage control outer loop works solid according to those figures once the DC-link voltage is 1200 V which follows the imposed reference. Besides, the
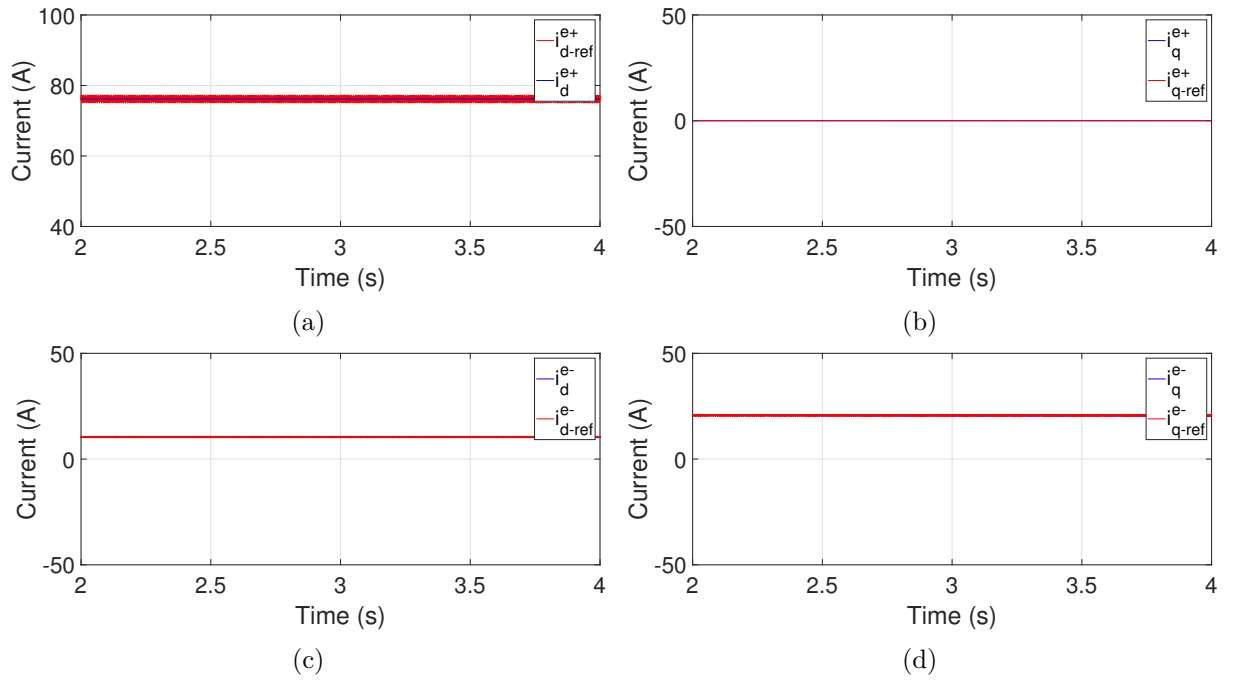
Figure 4.20 – Simulation results for unbalanced scenario and strategy 2 (connection at bus 7). (a) d positive-sequence component of the current. (b) q positive-sequence component of the current. (c) d negative sequence component of the current. (d) q negative sequence component of the current.
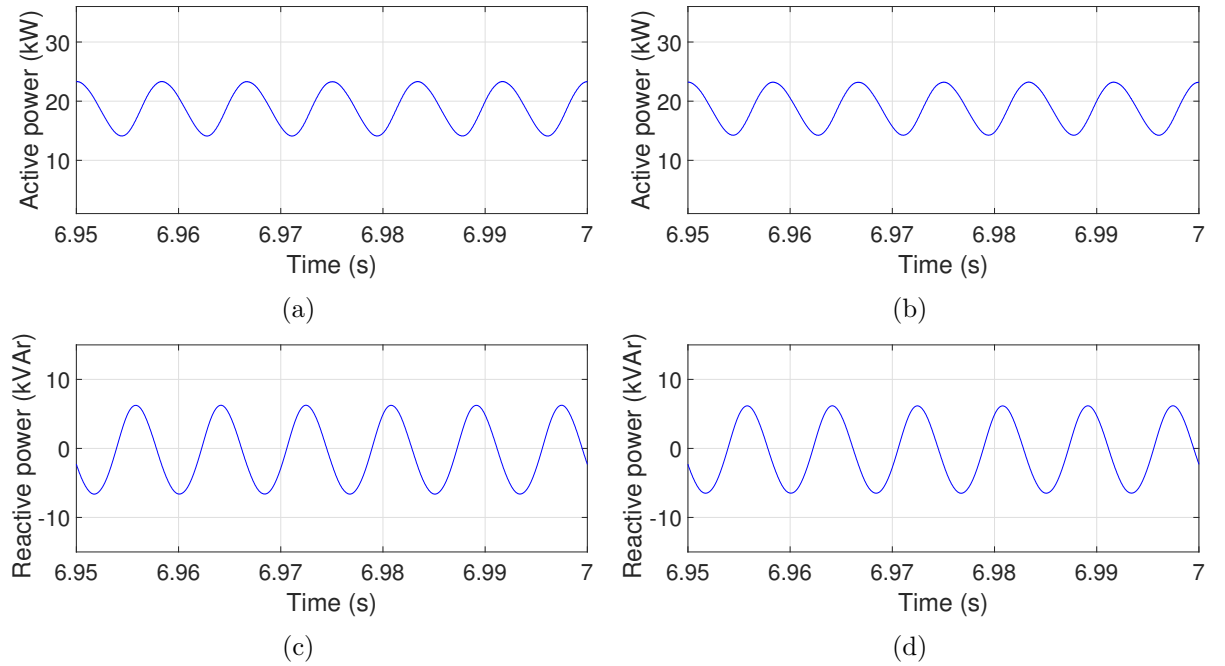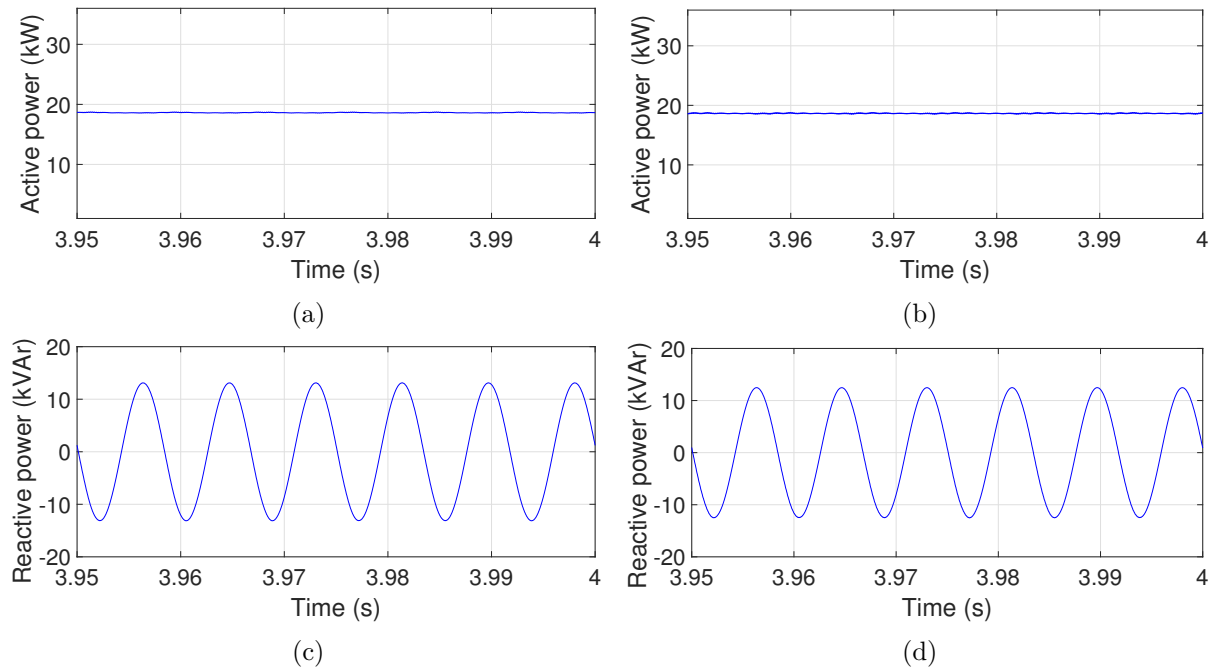

Figure 4.21 – Simulation results for unbalanced scenario and strategy 2. (a) Active power injected into the grid by the PV system for PV system connected at bus 5. (b) Active power injected into the grid by the PV system for PV system connected at bus 7. (c) Reactive power injected into the grid by the PV system for PV system connected at bus 5. (d) Reactive power injected into the grid by the PV system for PV system connected at bus 7.
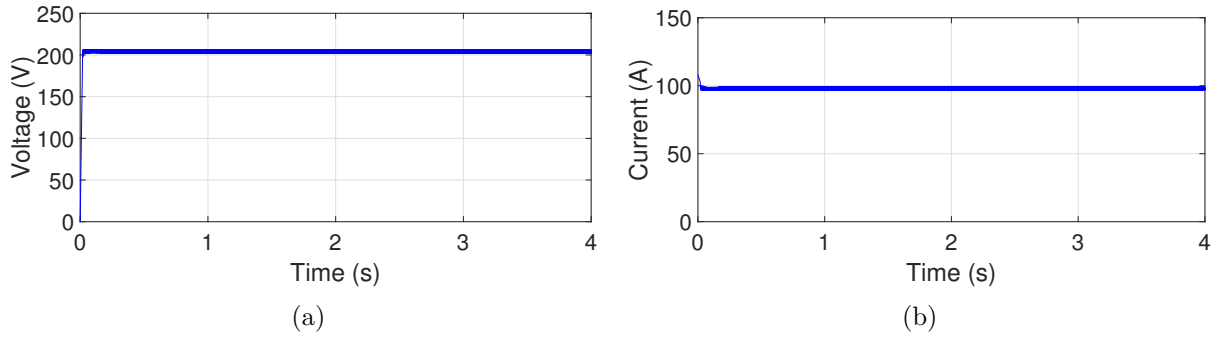
Figure 4.22 – Simulation results for unbalanced scenario and strategy 3. (a) PV array input voltage. (b) PV array input current.

three-phase current is shown in Figures 4.23 (c) and (d) for the PV system connected to buses 5 and 7, whose graphics present phase angular and magnitude differences. The focus of the inner current control here is not to make it balanced, despite having a well-defined sinusoidal shape.
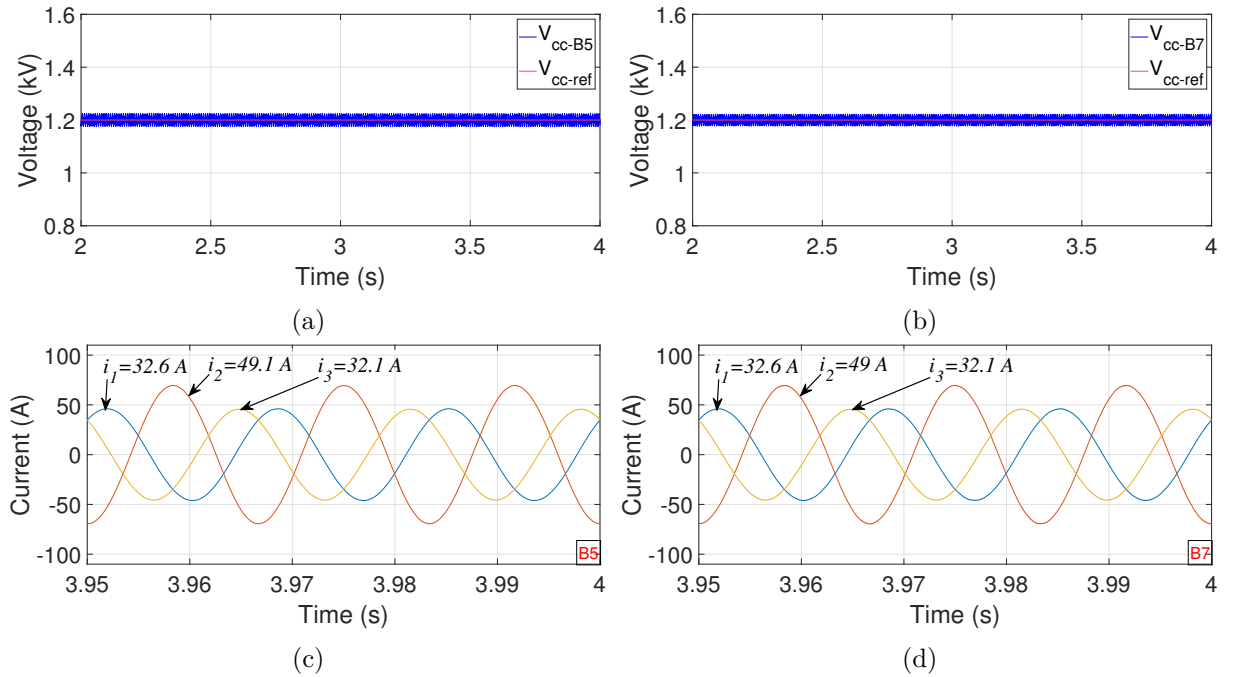
Figure 4.23 – Simulation results for unbalanced scenario and strategy 3. (a) DC-link voltage and its reference for bus 5. (b) Three-phase current injected into the grid by the PV system for bus 5. (c) DC-link voltage and its reference for bus 7. (d) Three-phase current injected into the grid by the PV system for bus 7.

The positive and negative sequence components of the three-phase current injected into the grid are controlled in the synchronous reference frame *dq* of the grid voltage, and this regulation is the main tool of the control strategies used here. That said, Figures 4.24 (a) and (b) show the positive components that indicate satisfactory control work since the *dq* signals are regulated according to their reference. Furthermore, the negative components were also satisfactorily regulated according to their references, as shown in Figures 4.24 (c) and (d), indicating the good performance of the current inner loop.
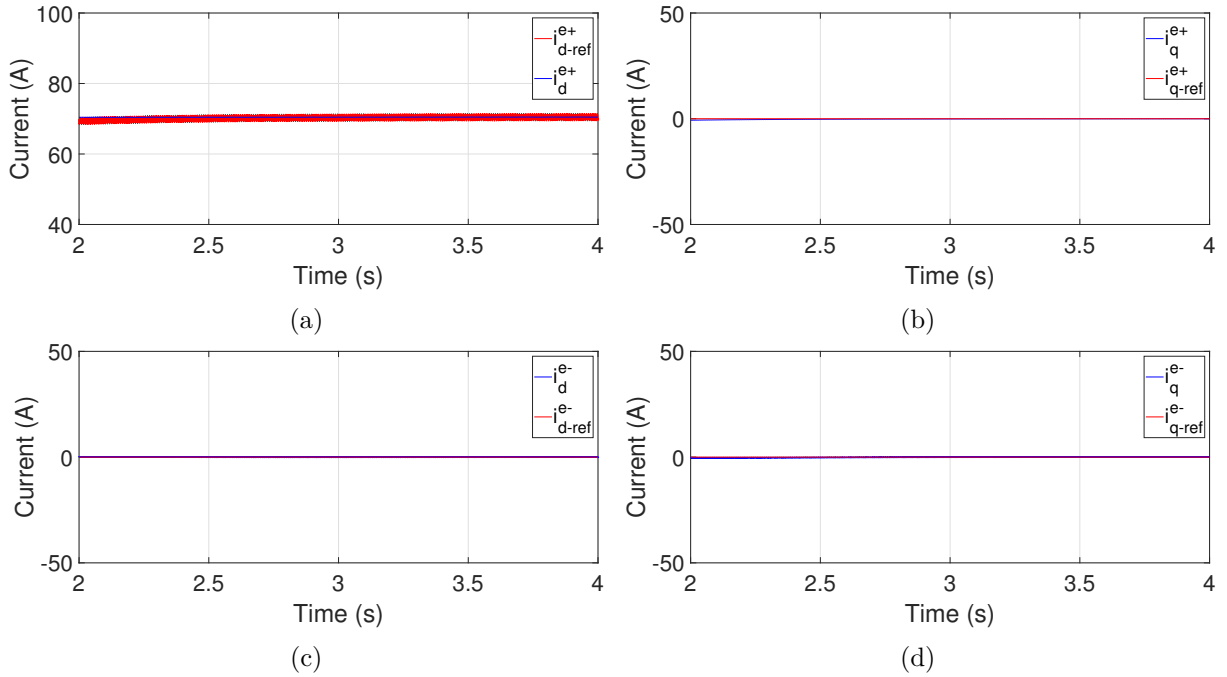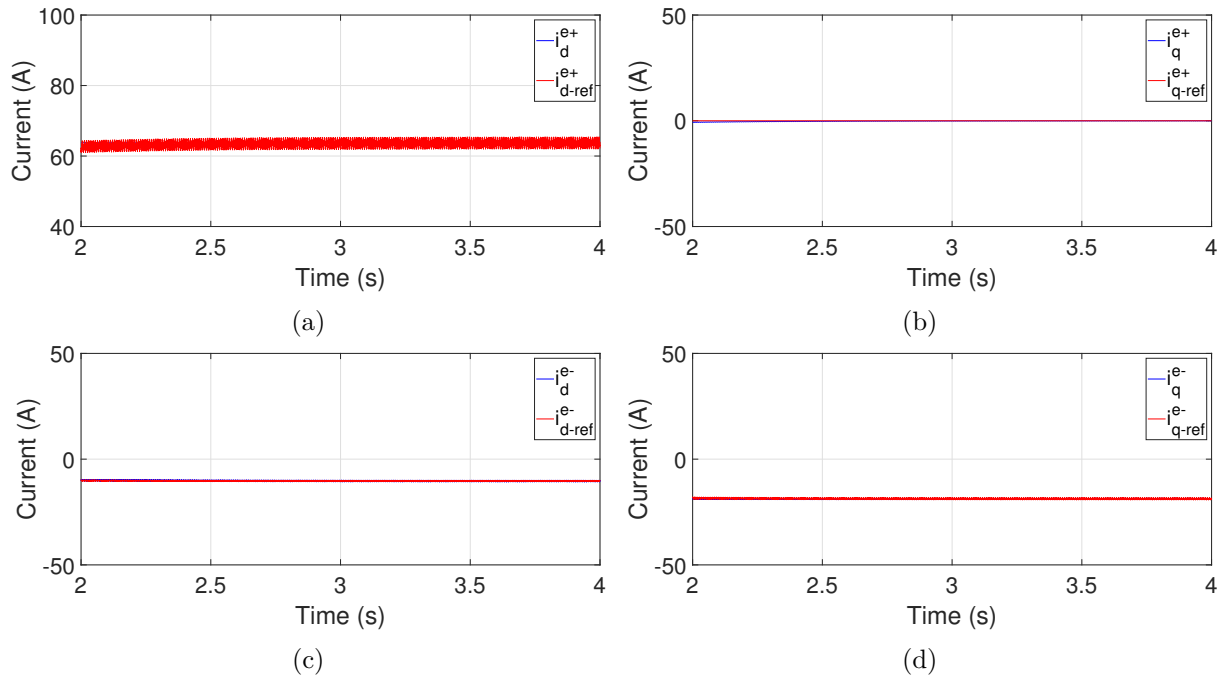
Figure 4.24 – Simulation results for unbalanced scenario and strategy 3 (connection at bus 5). (a) d positive-sequence component of the current. (b) q positive-sequence component of the current. (c) d negative sequence component of the current. (d) q negative sequence component of the current.
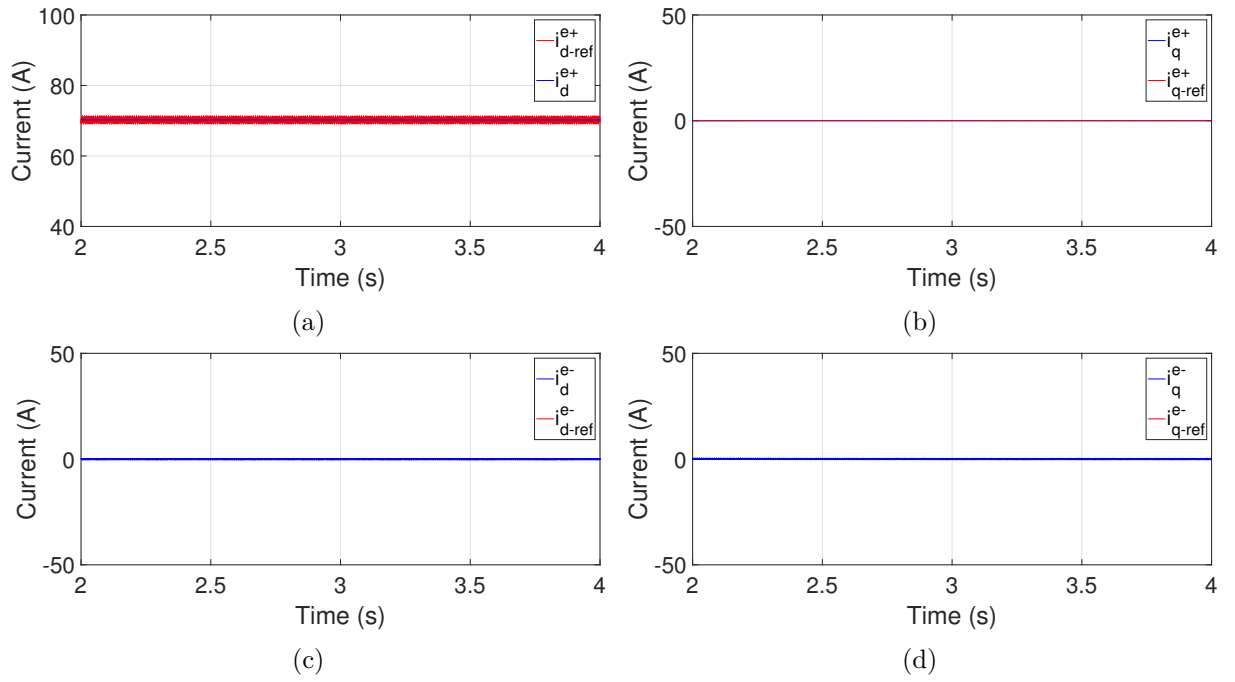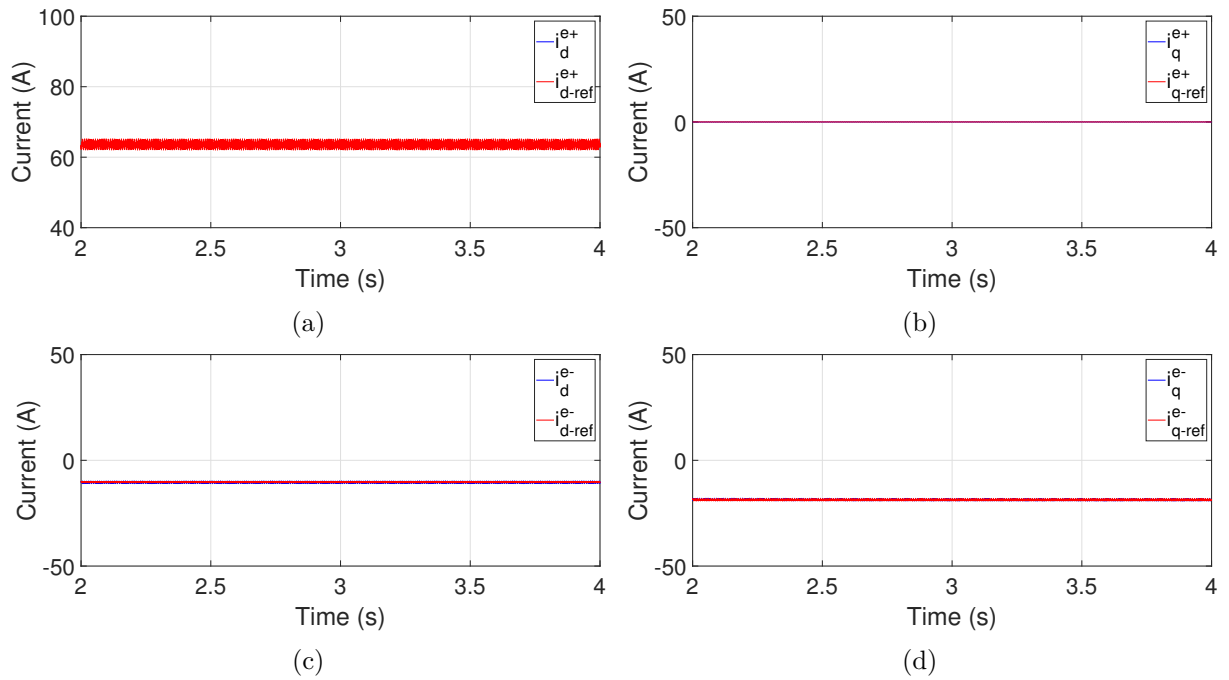

Figure 4.25 – Simulation results for unbalanced scenario and strategy 3 (connection at bus 7). (a) d positive-sequence component of the current. (b) q positive-sequence component of the current. (c) d negative sequence component of the current. (d) q negative sequence component of the current.

In strategy 3, the focus is the reactive power, so the oscillations in the active power keep happening, as shown in Figures 4.26 (a) and (b) for the PV system connected to bus 5 and bus 7. On the other hand, the reactive power has its oscillations reduced significantly, as shown in Figures 4.26 (c) and (d). This last results confirm the appropriate functioning of the strategy adopted for the PV system once the oscillations were reduced compared to the other strategies adopted in this work with the same simulation conditions.
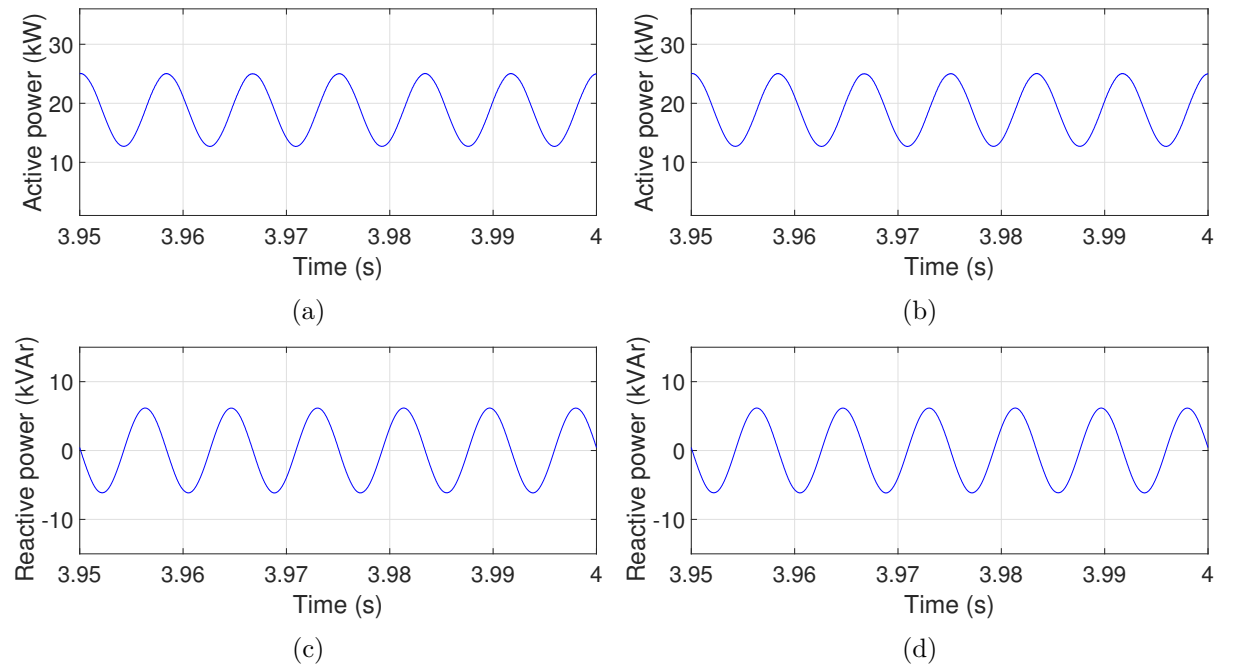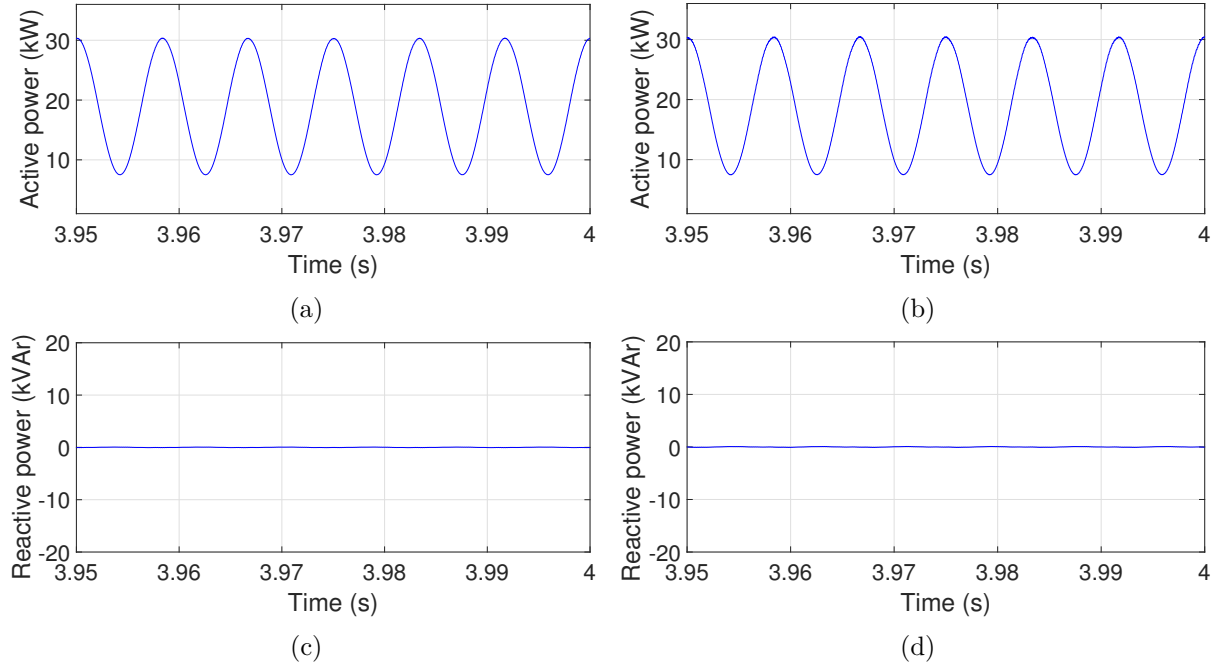

Figure 4.26 – Simulation results for unbalanced scenario and strategy 3. (a) Active power injected into the grid by the PV system for PV system connected at bus 5. (b) Active power injected into the grid by the PV system for PV system connected at bus 7. (c) Reactive power injected into the grid by the PV system for PV system connected at bus 5. (d) Reactive power injected into the grid by the PV system for PV system connected at bus 7.

4.4 RESULTS ANALYSIS

In the validation of the control system designed for balanced grids, the good operation of the control in the connection of the system between the electrical grid and the three-phase PV system was evident. The injected currents prove this, as they are balanced, as shown in Figure 4.2 (b) for bus 5 and 4.2 (d) for bus 7. Pratically, there are no differences between the PV system performance when it is connected to bus 5 or 7. All control structures were able to regulate their respective variables. Starting with the current control loop that managed to regulate the phase currents injected into the grid, which all remained with the same amplitude, at about 30 A RMS. The result obtained by the DC-link voltage outer loop is shown in Figures 4.8 (c) (bus 5) and 4.8 (d) (bus 7), where the bus voltage was regulated at about 1200 V, but it took too long. In addition, the work of the PLL in obtaining frequency/angle for synchronism performed well, as there

were no noticeable changes in the grid frequency or the lags of the voltage and current signals. And finally, the reactive and active power showed no oscillations, according to Figures 4.11 (a) and (b) for bus 5, and 4.11 (c) and (d) for bus 7, respectively.

Now moving on to the unbalanced electrical grid scenario, whose phase voltages were considered unbalanced due to a hypothetical grid fault. Thus, the performance of all control strategies is analyzed.

Concerging the conncetion at bus 5, the three-phase current injected into the grid by the PV system is the first quantity to be analyzed. In this way, when observing the results obtained for it by the four control strategies, the strategy 1 obtained the best performance, as it kept the currents balanced with RMS values of 40 A, as shown in Figure 4.13 (b). On the other hand, the conventional strategy failed and distorted them, as shown in Figure 4.7. Phases 1, 2, and 3 presented RMS values of 44 A, 39 A, and 39 A, respectively. Despite presented unbalances between the phases, Strategy 2 obtained sinusoidal currents as shown in Figure 4.18 (b), with RMS values of 52 A, 30 A and 53 A for phases 1, 2, and 3, respectively. Strategy 3 accomplish a similar performance, showing unbalances between the phases, as shown in Figure 4.23 (b), with RMS value of 32 A for phases 1 and 3, and 49 A for 2. Table 4.7 shows a summary of RMS values obtained for the three-phase current for PV connected to bus 5.

Table 4.7 – RMS values of the three-phase current injected into the grid for all the strategies (connection at bus 5)

Strategy	Phase 1	Phase 2	Phase 3
Conventional	44.1 A	39.7 A	39.8 A
1	40.6 A	40.7 A	40.6 A
2	52.2 A	30.5 A	53.4 A
3	32.6 A	49.1 A	32.1 A

The results for PV system connected to bus 7 are similar to those shown previously, in which the three-phase currents showed better behavior when strategy 1 was used. Table 4.8 shows the RMS results of the three-phase current for each strategy adopted in relation to the PV system connected at bus 7.

Table 4.8 – RMS values of the three-phase current injected into the grid for all the strategies (connection at bus 7)

Strategy	Phase 1	Phase 2	Phase 3
Conventional	43.9 A	39.6 A	39.7 A
1	40.5 A	40.5 A	40.5 A
2	51.2 A	30.6 A	52.4 A
3	32.6 A	49 A	32.1

Concerning the DC-link voltage, all strategies managed to stabilize it at 1200 V for PV system connected at bus 5, according to Figures 4.3 (c), 4.13 (a), 4.18 (a), and 4.23

(a) for conventional strategy and strategies 1, 2, and 3, respectively. The same occured for bus 7, as shown in Figures 4.3 (d), 4.13 (c), 4.18 (c), and 4.23 (c) for conventional strategy and strategies 1, 2, and 3, respectively.

Among all the strategies applied to the control structure of the PV system, the one that presented the lowest levels of oscillation in active power is strategy 2 (see Figure 4.21 (a)). This superiority is validated by observing Table 4.9 with the oscillation values for the injected active power on the grid by the PV system running all strategies. In this table, the peak-to-peak values and the percentage of oscillation that had as a calculation parameter the rated apparent power of the system, which is 20 kVA, are displayed. Thus, active power has a peak-to-peak ripple of 0.2 kW when strategy 2 is applied to the PV system, which represents a percentage of 1% ripple. In addition, the power has a 45% oscillation percentage with the conventional strategy running on PV (see Figure 4.11 (a)), being the second best in this regard with a peak-to-peak value of 9 kW. The PV system running strategy 1 (see Figure 4.16 (a)) has a peak-to-peak value of 12.4 kW, resulting in an oscillation percentage of 62%. And finally, the worst oscillations of this electrical quantity are observed when the PV runs strategy 3 (see Figure 4.26 (a)), as its peak-to-peak value of 22.8 kW is the highest and leads to an oscillation percentage of 114%.

Table 4.9 – Peak values of the active power for all strategies and PV system connected to bus 5

Strategy	Avarage	Peak-to-peak value	Oscillation percentage
Conventional	18.8 kW	9 kW	45%
1	18.8 kW	12.4 kW	62%
2	18.6 kW	0.2 kW	1%
3	18.9 kW	22.8 kW	114%

The active power oscillation also has the lowest level when the PV system runs strategy 2 and is connected to bus 7, which is a similar behavior to the previous one. Table 4.10 shows the summary of active power oscillation peak-to-peak and percentage values for all strategies for the PV system connected to bus 7.

Table 4.10 – Peak values of the active power for all strategies and PV system connected to bus 7

Strategy	Avarage	Peak-to-peak value	Oscillation percentage
Conventional	18.8 kW	8.8 kW	44%
1	18.8 kW	12.4 kW	62%
2	18.6 kW	0.2 kW	1%
3	18.9 kW	23.2 kW	116%

The reactive power is also a specific target of the control structure used in this work, especially in strategy 3 (see Figure 4.26 (c)), which presented the best results for this quantity with a peak-to-peak value of 0.14 kvar, leading to a percentage oscillation of only 0.7% for 20 kVA rated power as the parameter. The reactive power has a percentage oscillation of 60% when the PV system runs strategy 1 (see Figure 4.16 (c)), and the

peak-to-peak value is 12.2 kvar. This quantity has a peak-to-peak value of 13.2 kvar for a PV system running the conventional strategy (see Figure 4.11 (c)), which results in a percentage oscillation of 66%. Finally, the top oscillation peak-to-peak value is 26.2 kvar for the PV system running strategy 2 (see Figure 4.21 (c)), being the worst result with an oscillation percentage of 131%. Table 4.11 summarizes the commented results for the reactive power of the PV system for the connection at bus 5.

Table 4.11 – Peak-to-peak and percentage values of the reactive power for all strategies and PV system connected to bus 5

Strategy	Avarage	Peak-to-peak value	Oscillation percentage
Conventional	-0.3 kvar	13.2 kvar	66%
1	0 kvar	12.2 kvar	61%
2	0 kvar	26.2 kvar	131%
3	0 kvar	0.14 kvar	0.7%

As before, a behavior similar to the previous one is observed for PV system connected to bus 7 in relation to reactive power, in which strategy 3 presents the best results for this quantity. Table 4.12 shows the values related to reactive power for all strategies with the PV system connected to bus 7.

Table 4.12 – Peak-to-peak and percentage values of the reactive power for all strategies and PV system connected to bus 7

Strategy	Avarage	Peak-to-peak value	Oscillation percentage
Conventional	-0.3 kvar	13 kvar	65%
1	0 kvar	12 kvar	60%
2	0 kvar	24.8 kvar	124%
3	0 kvar	0.2 kvar	1%

4.5 CONCLUSION

In this chapter, the results of the four strategies were presented and the control structure was validated. It is noted that the conventional system presents good results when the grid is fully balanced, but the performance drops considerably when the grid is unbalanced. In addition, strategies 1, 2, and 3 that use a control structure for both positive and negative components, proved capable of accomplishing what was expected of them. Strategy 1 was the most effective in regulating the current injected into the electrical grid, showing better results than the conventional control. On the other hand, strategy 2 demonstrates to be more efficient in reducing active power oscillations, confirming the validation of its good performance. Finally, strategy 3 showed great efficiency in reducing reactive power oscillations compared to all the others.

5 SIMPLIFIED MODEL

5.1 INTRODUCTION

In this chapter, the simplified model for the photovoltaic system is presented to obtain more results and analysis of the proposed control strategies and is needed due to computational limitations. In this sense, this model reduces the computational demand and, hence, reduces the execution time of the simulations. The result analysis is related to the unbalanced factor and line losses.

5.2 MODIFICATIONS MADE TO THE PV SYSTEM

The approach here is to use the basic model of a connection between an AC grid and a system that needs a three-phase inverter (such as a PV system) in the simulations, as illustrated in Figure 5.1. The intention is to make the model simpler and for that, there is the replacement of the PV panels together with the boost converter for an ideal controlled current source, capable of injecting power according to the demand. Also, knowing the value of the input power of the PV system and the DC-link voltage, it is possible to determine the value of the current source, according to the following expression

$$i_{dc} = \frac{P_{in}}{v_{dc}} = \frac{20\,\text{kW}}{1200\,\text{V}} = 16.667\,\text{A} \tag{5.1}$$

where i_{dc} represents the current source, P_{in} is the PV input power, and v_{dc} is the DC-link voltage.
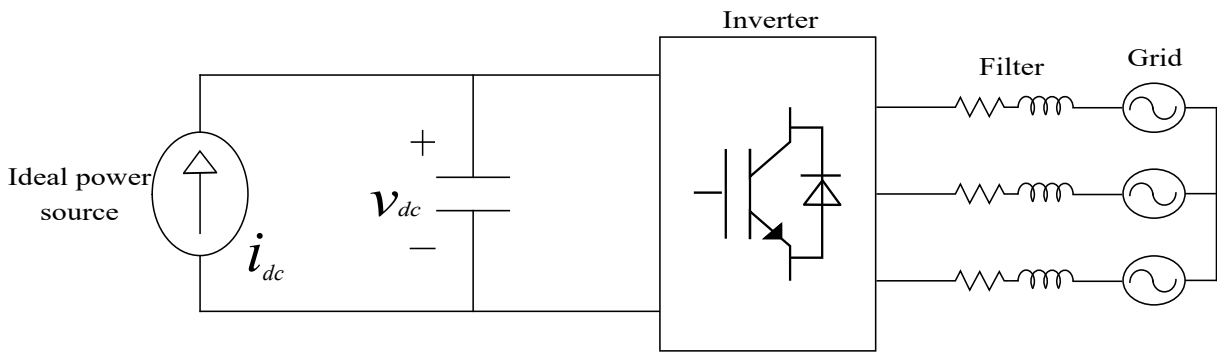
Figure 5.1 – System model with ideal power source

A part of the model implemented in MATLAB/SIMULINK® that consumes a lot of computational processing is the PWM technique used to activate the IGBTs switches of the three-phase inverter model. This modulation technique requires that the calculation step is small enough so that all calculations are performed satisfactorily during the simulation, otherwise, errors occur in the simulations that do not proceed as they should. Therefore, controlled voltage sources are used instead of inverter switches to make simulations faster

because they can be activated directly by the voltage reference signals provided by the current control loop. Previously, these signals would go to the PWM modulation that was in charge of sending the activation signals to the IGBTs switches. However, these reference signals are used directly to activate the controlled sources, as illustrated in Figure 5.2.

In addition to the presence of controlled voltage sources in Figure 5.2, there are two controlled sources of current, one of which represents the PV system power, and the other is related to the input current of the three-phase inverter. The value of the first current source has already been defined previously, and the second current source has its value calculated based on the power being delivered to the grid by the controlled voltage sources. This calculation leads to the power balance on the DC-link, and the consequent voltage regulation of the same is carried out according to the desired value and imposed by the control system responsible for it.
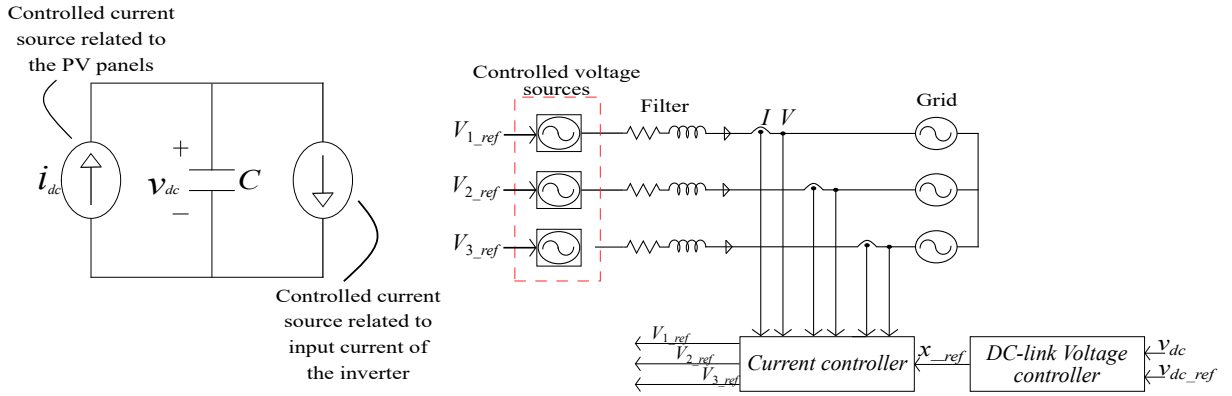
Figure 5.2 – System model with controlled current and voltage sources

With the system in Figure 5.2, it was possible to drastically reduce the simulation time of our electrical grid, which remained the same as described in the previous chapters, with seven buses and the primary power source. Nine simulations were performed for the results presented in the previous chapter, where the time average to complete each of those simulations was four hours. With the new simplified model for the PV system, it was possible to reduce the time to an average of 15 minutes per simulation. Besides, as will be seen further on, this simplification did not affect the quality and how the results were presenting themselves until now.

5.3 VALIDATION OF RESULTS FOR THE SIMPLIFIED SYSTEM

Initially, a comparison must be made between the results found with the simplified system and the results found for the complete PV system to validate the simulations with the simplified one. Therefore, a scenario was established for this comparison, in which both systems are connected to Bus 5 one at a time, injecting 100% of its active power capacity. Also, the power grid is unbalanced due to load distribution and the type-D fault. All three main strategies are applied to both systems, and some results are shown as follows.

It should be highlighted and remembered that the strategy 1 is related to injecting balanced currents into the electrical grid, by trying to eliminate the negative sequence components of this quantity. Strategies 2 and 3 are responsible for mitigating fluctuations in active and reactive power, respectively. In this way, all these strategies are used in the simulations to demonstrate that the simplified system works correctly.

As for the result with the complete photovoltaic system presented in Chapter 4, a hypothetical fault was considered that would lead to a type D unbalance (BOLLEN; ZHANG, 2003) in the electrical grid voltage. Again, the phasor chosen for the voltage during the sag is $\vec{V} = 0.5\vec{E}$, and $\vec{E} = 13.8\angle 0°$ kV is the pre-fault voltage phasor. Thus, the voltages of the electrical grid source during the unbalance are the same presented in (4.1) - (4.3) and can be seen in the following expressions

$$E_{g1} = V_1 = 6,9\angle 0° \tag{5.2}$$

$$E_{g2} = V_2 = 12,4391\angle -106.1° \tag{5.3}$$

$$E_{g3} = V_3 = 12,4391\angle 106.1° \tag{5.4}$$

The validation of the simplified model is then done with the scenario described so far, and the main electrical quantities are shown below for each strategy.

5.3.1 Strategy 1

Starting with the results found for PV system running the strategy 1, the first quantity shown here is the DC link voltage, which is crucial for the correct operating of the system connected to the electrical grid. These quantities for the simplified and complete models are shown in Figures 5.3 (a) and (b). It can be seen from these figures that the simplified system works correctly, as the voltage is stabilized at 1200 V, following the same behavior shown by this quantity for the complete system.
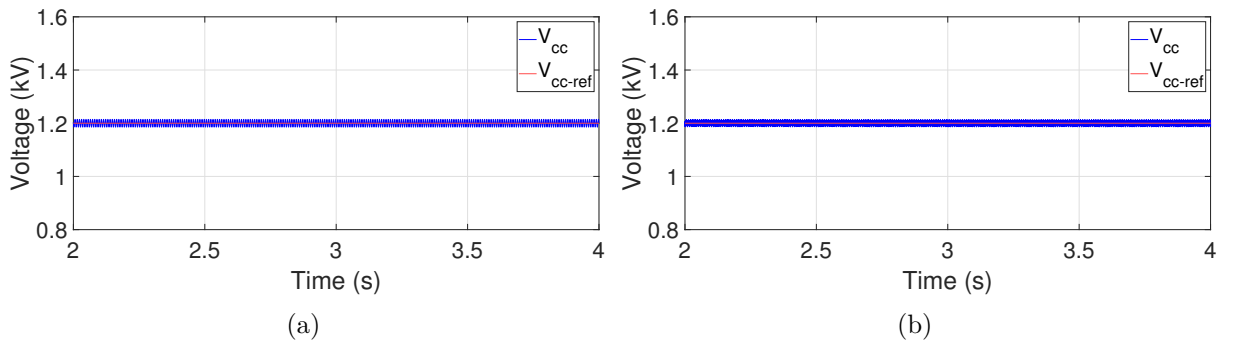
Figure 5.3 – Validation of the simplified model. DC-link voltage for PV system running strategy 1 with the (a) simplified and (b) complete models

The currents injected into the grid by the PV system (the simplified and complete) are the main quantities to verify how the simplified model works with strategy 1. Hence, these currents are shown in Figures 5.4 (a) and (b). The RMS values shown in Figure 5.4

(a) indicate that strategy 1 was well applied by the simplified PV system because they are very close to each other: 43.4 A, 42.8 A, and 42.8 A for phases 1, 2, and 3, respectively. Furthermore, although the curves in Figures 5.4 (a) and (b) are sinusoidally equal, there is a slight difference between the RMS values due to the presence of non-ideal IGBTs switches of the three-phase inverter in the complete model. The highest difference of 6.5% occurs in phase 1, the result of the difference between 43.4 A (simplified) and 40.6 A (complete). However, this does not mean a PV system malfunction, but only a difference because of non-ideal component model usage.

Figure 5.4 – Validation of the simplified model. Injected currents into the grid by (a) simplified and (b) complete models when stratey 1 is applied.

As a reflection of the differences between the currents shown in Figures 5.4 (a) and (b), the active and reactive powers also present divergences in their maximum peak values. The active powers shown in Figures 5.5 (a) and (b) have identical sinusoidal shapes and peak values of 26.58 kW and 25.06 kW, which means a tiny difference in the maximum values they reach. In addition, the reactive powers in Figures 23 (a) and (b) for the simplified and complete system present the same behavior, slightly differing in their maximum values of 6.56 kvar (complete model) and 6.18 kvar (simplified model).

5.3.2 Strategy 2

The DC link voltage is shown in Figures 5.6 (a) and (b) for the simplified and the complete models running strategy 2. As happened for strategy 1, these figures indicate that the simplified model works correctly, once the voltage for this model is regulated at 1200 V, as for the complete one. Besides, there are differences in the voltage curves explained by the extra components in the full model, such as IGBTs switches, inductances and capacitances.

Strategy 2 focuses on active power trying through the injection of currents to reduce the oscillations of this quantity. Hence, the three-phase electrical currents in Figures 5.7 (a) and (b) for the simplified and complete system have angle phase shifts but maintain their sinusoidal shapes. Analyzing phase by phase, the differences from the RMS values shown in Figures 22 and 33 are: phase 1 with values of 56.3 A (simplified) and 52.2 A
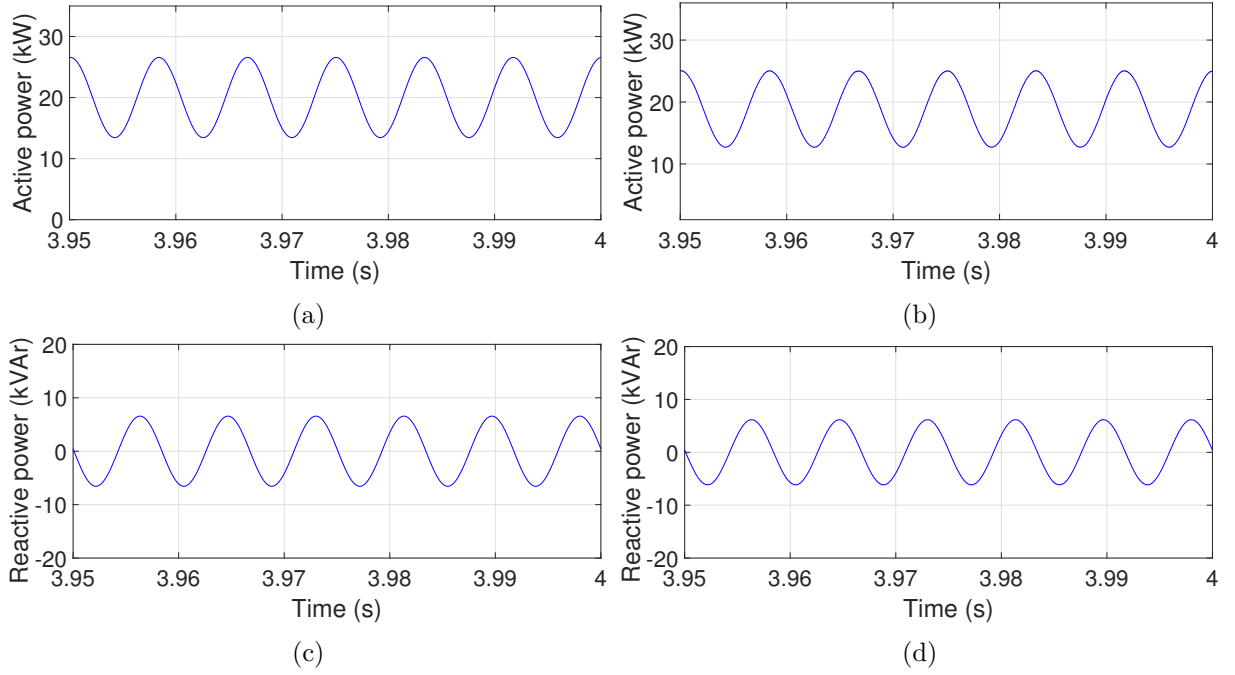
Figure 5.5 – Validation of the simplified model. Active power of the (a) simplified and (b) complete PV system running strategy 1; reactive powers for the (c) simplified and (d) complete PV system running strategy 1.
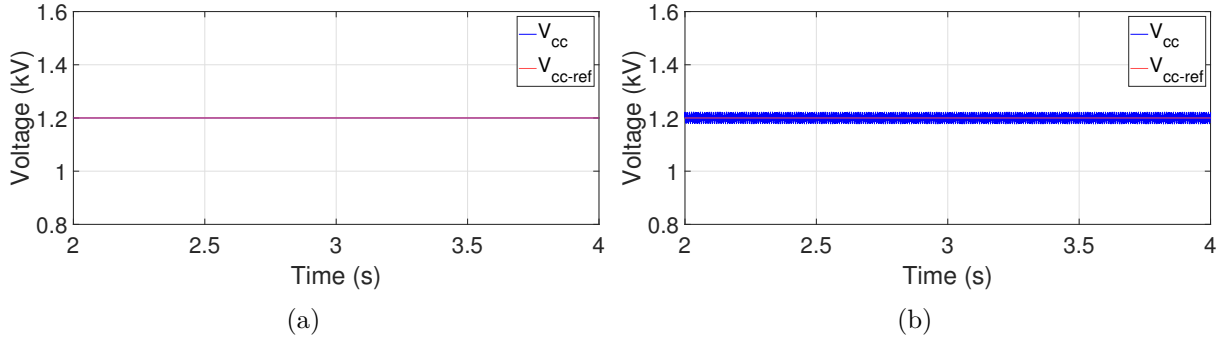
Figure 5.6 – Validation of the simplified model. DC-link voltage for the (a) simplified and (b) complete models running strategy 2.

(complete) has a difference of 7.2%; phase 2 with values of 32.5 A (simplified) and 30.5 A (complete) has a difference of 6.1%; and phase 3 with values of 57.2 A (simplified) and 53.4 A (complete) has a difference of 6.6%. This divergence pattern repeats in every simulation since the same nonideal IGBTs switches are used in the inverter.

Active power is the best parameter to assess whether the simplified model works as expected when strategy 2 is used. The peak value reached by this quantity for the simplified system in Figure 5.8 (a) is 20 kW, remaining at this value in the steady state, which means the complete elimination of its oscillations, and corroborates the proper functioning of the simplified model. The power of the complete model in Figure 5.8 (b) has a maximum value of 18.74 kW, with a modest oscillation of 0.12 kW compared to the average of 18.62 kW. Note that the complete one presents a performance slightly worse

(a)   (b)
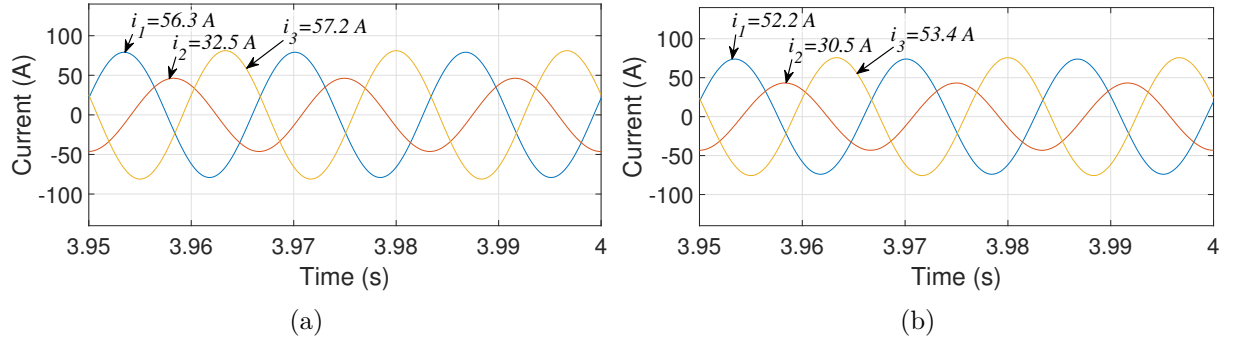
Figure 5.7 – Validation of the simplified model. Injected currents into the grid by (a) simplified and (b) complete models when stratey 2 is applied.

than the complete one concerning the damping of the oscillations because it has non-ideal elements, such as the boost converter and the three-phase inverter switches. Furthermore, the reactive power also presents a negligible difference for these reasons. This quantity for the simplified model, shown in Figure 5.8 (c), has a maximum value of 13.96 kvar, and for the complete model in Figure 5.8 (d) is 13.62 kvar, resulting in a difference of 2.4%.

(a)   (b)

(c)   (d)
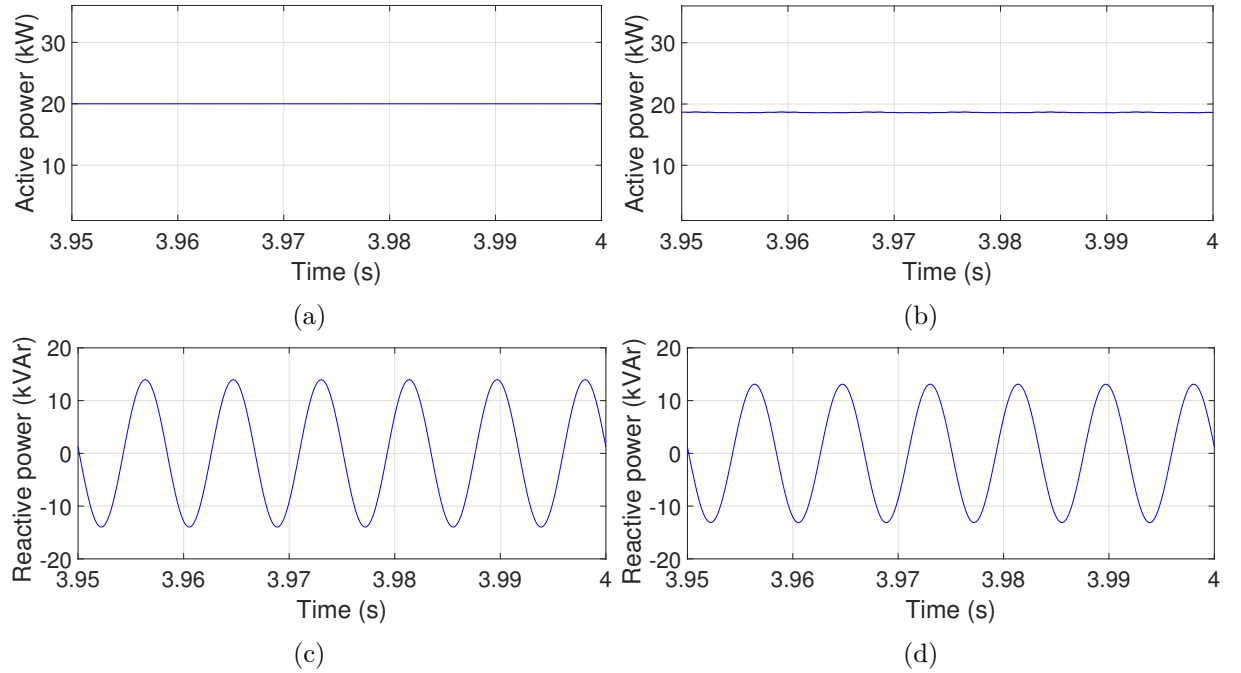
Figure 5.8 – Validation of the simplified model. Active power of the (a) simplified and (b) complete PV system running strategy 2; reactive powers for the (c) simplified and (d) complete PV system running strategy 2.

5.3.3 Strategy 3

To validate strategy 3 for the simplified model, the DC-link voltages for this model and the complete one are shown in Figures 5.9. In this sense, these voltage curves confirm the correct execution of the simplified model when strategy 3 is active, as this magnitude is set at 1200 V, as expected.
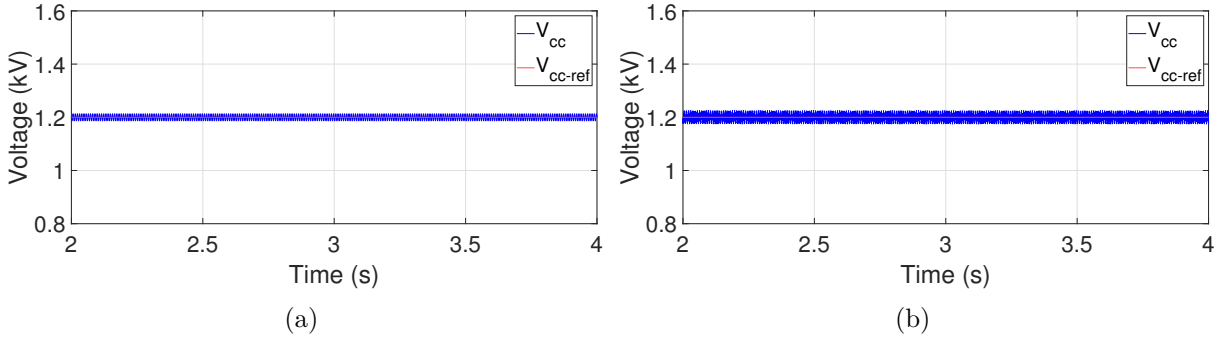
Figure 5.9 – Validation of the simplified model. DC-link voltage for the (a) simplified and (b) complete models running strategy 3.

The currents injected into the grid by the PV system running strategy three are displayed in Figures 5.10 (a) and (b) for the simplified and complete model. When comparing the three-phase currents of Figures 5.10 (a) with those of 5.10 (b), they present differences in the RMS values, but they remain with their sinusoidal shapes without distortions. In this way, the simplified one has RMS values of 34.7 A, 51.6 A, and 33.6 A, and the complete one has 32.6 A, 49.1 A, and 32.1 A for phases 1, 2, and 3, respectively. The differences are around 5%.
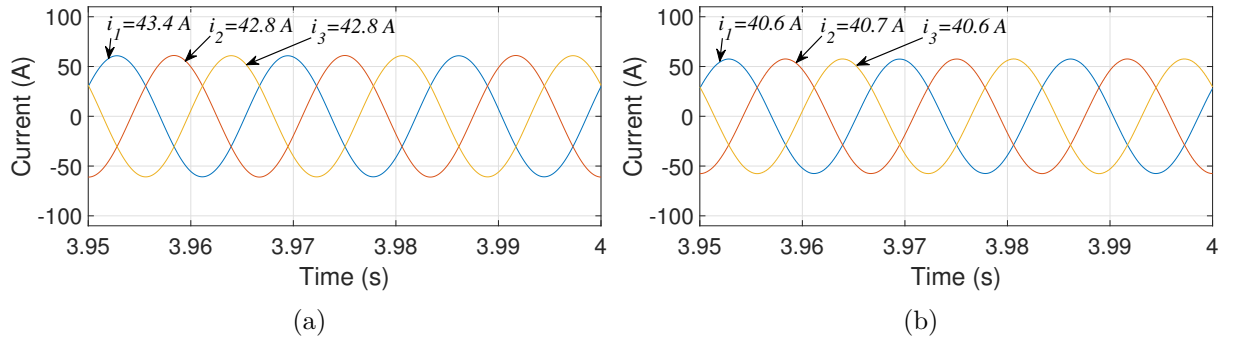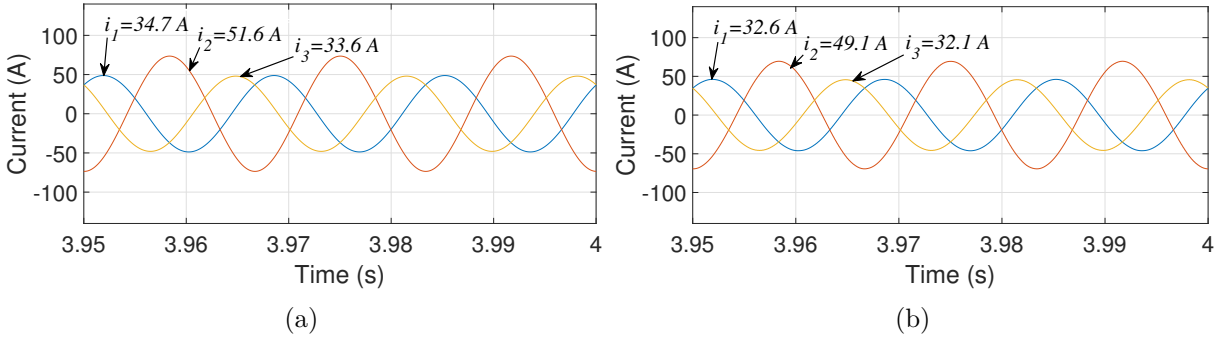

Figure 5.10 – Validation of the simplified model. Injected currents into the grid by (a) simplified and (b) complete models when the stratey 3 is applied.

However, the crucial parameter to validate the results for the simplified model running the strategy 3 is the reactive power, since this strategy aims to attenuate its oscillations. In Figures 5.11 (a) and (b), the reactive powers for the simplified and complete models are shown. The peak values for the simplified is 0.07 kvar and for the complete one is 0.04 kvar, i.e., there is a trivial difference between them. Also, the simplified one works when strategy 3 is applied in the current control, once the oscillations of the reactive power are practically null. However, the crucial parameter to validate the results for the simplified model running strategy 3 is the reactive power since this strategy aims to attenuate its oscillations. This electrical quantity for the simplified and complete models is shown in Figures 5.11 (a) and (b). The peak value for the simplified is 0.07 kvar and for the complete one is 0.04 kvar, i.e., there is a trivial difference between them. Thus, the simplified one works when strategy three is applied in the current control structure, once the oscillations

of the reactive power are practically null. The active powers displayed in Figures 5.11 (c) and (d) have considerable fluctuations, with peaks reaching 32.15 kW and 30.36 kW for the simplified and complete systems, respectively.

(a)

(b)

(c)

(d)
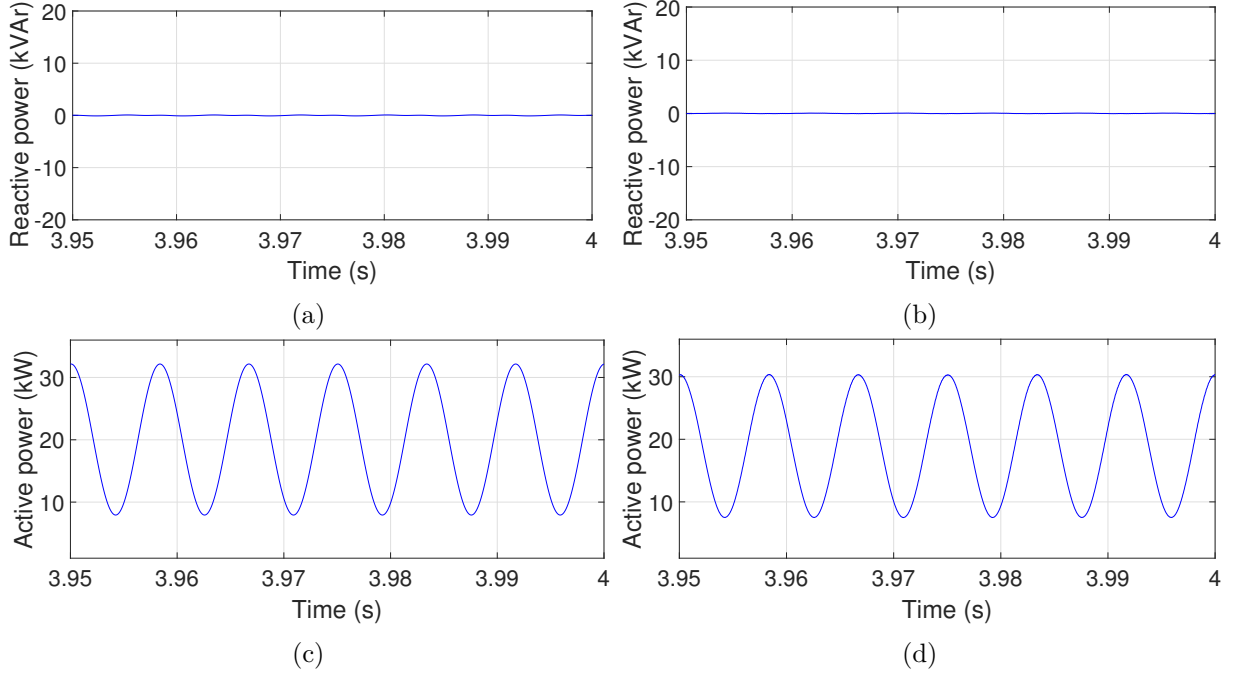
Figure 5.11 – Validation of the simplified model. Reactive power for (a) simplified and (b) complete models when the strategy 3 is applied.

In conclusion, all the results obtained here corroborate the excellent work of the simplified system designed to replace the model with the panels, boost, and three-phase inverter. In addition, the conventional strategy was also applied, showing the same pattern of results for the other ones. The system was also connected to bus 7 to verify how the simplified system performed in this situation. In this way, its performance running the strategies is identical to the system connected to bus 5, as the results are similar in both scenarios. Therefore, the analyzes and results shown below are supported by the results verified in this section.

5.4   UNBALANCE FACTOR ANALYSIS

The unbalance factor is an index that measures how unbalanced the voltages of an electrical grid are. As mentioned, this index is given by the relationship between the negative-sequence component of the voltage and its positive component, according to expression (4.4) (MIRET et al., 2012), and re-introduced below

$$n = \frac{V^-}{V^+} \tag{5.5}$$

The voltage unbalance factor of the primary power source of the electrical grid was calculated in (4.3), and its value is 0.333.

The simplified model of the PV system allows a large number of simulations, as its execution time is short compared to the complete model. Therefore, to carry out a detailed impact analysis of the PV system penetration in the grid, the input power of this system was varied, and the unbalance was observed in each bus. Furthermore, the simplified PV system was connected to buses 5 and 7, one at a time, in the same way as before.

The PV system is naturally intermittent in the power supply since its efficiency at it is influenced by temperature, solar irradiation, and shading conditions (ALAJMI et al., 2013; PATEL; AGARWAL, 2008). Therefore, a scenario was imagined in which the PV system suffered different variations in its input power, which would simulate this intermittence. Thus, with the system connected to the respective simulation bus, its input power was varied according to the following pattern: starting with the value of 2 kW and increasing in the same proportion until the rated capacity of the system is reached, which is 20 kW.

First, the simulations considered only the injection of active power into the grid by the PV system, but the control used here allows the injection of reactive power for the three main strategies. Therefore, the reactive power was also injected into the grid following the variation of the input power, according to the expression below

$$Q_{inj} = \sqrt{S_{in}^2 - P_{in}^2} \tag{5.6}$$

where Q_{inj} is the injected reactive power, S_{in} is the rated apparent power that maximum value is 20 kVA, and P_{in} is the input active power.

One by one, the control strategies were applied to the simplified PV system that was connected to bus 5 or 7, and there was an increase in input power. Therefore, four simulations were performed at each 2 kW increase of the PV system. Furthermore, the symmetrical components in the stationary frame were used to calculate the unbalance factors in bus 7, which is the last one in the system and was chosen for the analysis.

The results for the unbalance factors of bus 7 when the PV system is connected to bus 5 were gathered in Figure 5.12. This figure displays the unbalance curves concerning the system input power, for each of the strategies studied, with and without injection of reactive power. Briefly: Conventional is for the conventional one; P1, P2, and P3 represent strategies 1, 2, and 3, respectively, considering only the injection of active power by the PV system; and, finally, PQ1, PQ2, and PQ3 are for strategies 1, 2 and 3, respectively, with the injection of active and reactive power into the grid.

It can be seen from Figure 5.12 that the best results for the unbalance factors are for the PQ2 curve, i.e., when the PV system runs strategy 2 with reactive injection. In this scenario, the lowest value of this index is 0.3119 when the system injects 18 kW (active power) and 8,717 kvar (reactive power). The second best performance occurs with strategy 2 (P2 curve), whose lowest value observed is 0.3144 with 20 kW (rated capacity) active
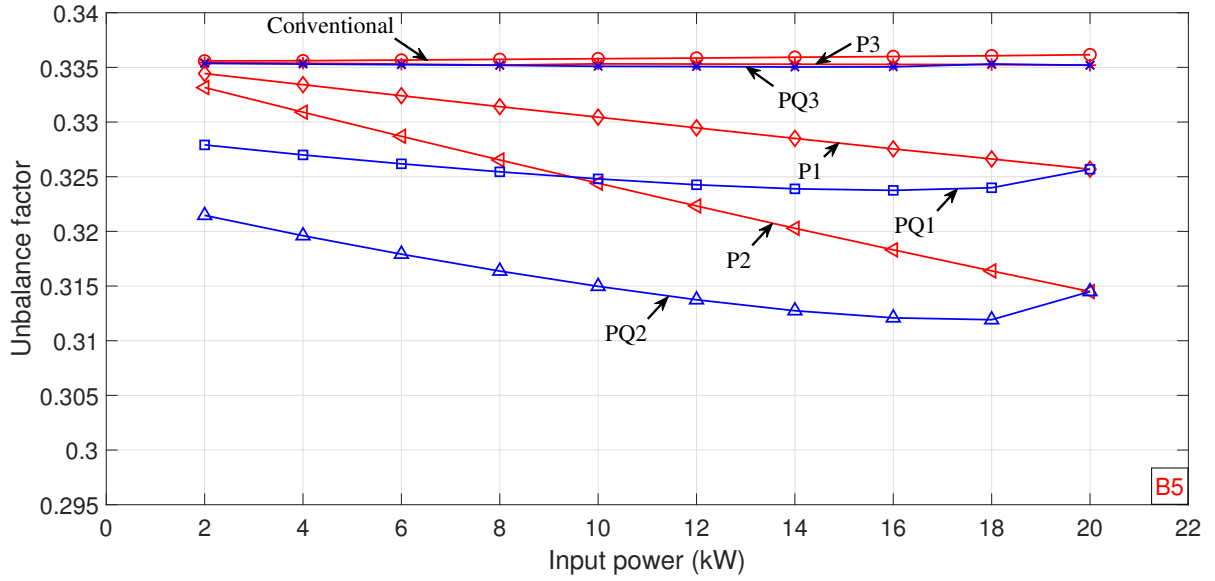
Figure 5.12 – Graphs for the unbalance factors at bus 7 when PV system is connected to bus 5. P1, P2, and P3 are graphs for strategies 1, 2, and 3 injecting only active power; PQ1, PQ2, and PQ3 are graphs for strategies 1, 2, and 3 injecting both active and reactive powers.

power injection. On the other hand, the conventional curve in the figure indicates that this strategy presented the worst result for the unbalance factors, whose highest value is 0.3361 with the injection of 20 kW, implying in a difference of 7.8% from the best one PQ2. Also, the PQ3 and P3 curves show very similar behavior with tiny variations in the values of the unbalance factors, which average is 0.3352.

Now the curves for the unbalance factors of bus 7 are shown in Figure 5.13 when the PV system is connected to bus 7.

Observing Figure 5.13, the same behavior occurs for its curves as well as those presented in Figure 5.12, in which the PQ2 curve is the one that shows the best results, and its lowest value for the unbalance factor is 0.3001 with the injection of 18 kW and 8,717 kvar. Curve P2 remains the second best option, with its minimum record at 0.3014. However, the conventional strategy is not the worst anymore, its highest value is 0.3348 (P = 20 kW), and the lowest is 0.3321 (P = 2 kW). The PQ3 and P3 curves are in the last place now, as their highest unbalance factor is 0.3355, but they remain practically static throughout the input power variation. Besides, making a comparison at the same point of the input power P = 18 kW, the PQ2 curve presents 11.62% less unbalance compared to the PQ3 and P3 curves, once its unbalance factor is 0.3001 at this point, and for the others, is 0.3351.

The voltage vectors in the double synchronous reference (positive and negative sequence) were observed to explain the reliable work of strategy 2 and the ineffectiveness of strategy 3 in correcting voltage unbalance factors. That said, Tables 5.1 and 5.2 summarize the values of the positive and negative sequence components of voltage at bus 5 for the
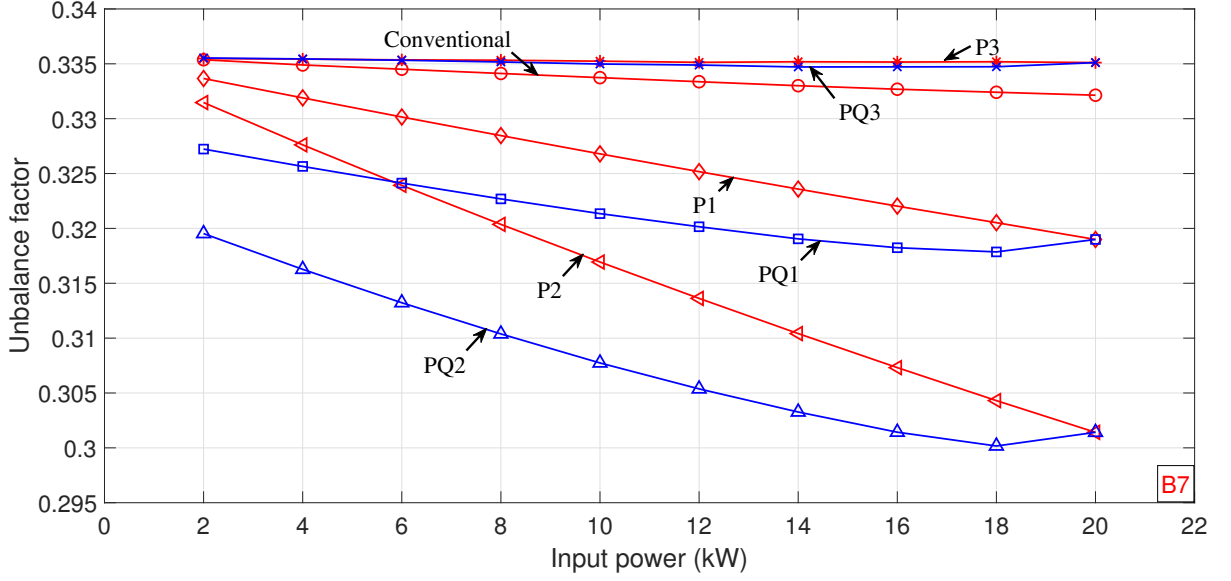
Figure 5.13 – Graphs for the unbalance factors at bus 7 when PV system is connected to bus 7. P1, P2, and P3 are graphs for strategies 1, 2, and 3 injecting only active power; PQ1, PQ2, and PQ3 are graphs for strategies 1, 2, and 3 injecting both active and reactive powers.

different scenarios and strategies. It can be seen from these tables that strategy 2 manages to reduce the negative sequence vectors of the voltage along it increases the positive sequence ones. Strategy 3 also achieves the feat of increasing the positive vectors, but also increases the negative ones, implying that it cannot effectively correct voltage unbalances. Furthermore, the conventional strategy follows the same profile as strategy 3, and strategy 1 behaves like 2, but with less effectiveness.

5.5   LINE LOSS ANALYSIS

According to Prodist's module (ANEEL, 2021), there are technical and non-technical losses, the first being characterized by the difference between the energy generated and the energy delivered to the distribution grid, including losses on the line. The second would be those losses arising from the difference between the total measured and the technical losses. Thus, as the electrical grid simulated here is small and decoupled (for simplification), in addition to accessing the values of current and resistance of the line, the Joule effect losses in the distribution line are computed for the loss analysis. For this purpose, the characteristics of the distribution line in Table 5.3 are used. And the Joule effect losses are calculated following expression (5.7).

$$P_{losses} = R_\Omega i^2 \tag{5.7}$$

where R_Ω is the line resistance, and i is the RMS current value.

The input power variation of the simplified PV system is varied as in the unbalance factor section. Thus, it is increased in a step of 2 kW until reaching the power rate of 20

Table 5.1 – Voltage vectors for bus 5 in the double synchronous reference frame (system connected to bus 5)

Input power	Strategy	v_d^+	v_q^+	v_d^-	v_q^-
2 kW	Conventional	260.9826	-0.0114	-41.9753	-76.8955
	1	261.0043	-4.5418e-04	-41.9223	-76.6019
	2	261.1048	0.0024	-41.5819	-76.4400
	3	260.9206	-0.0017	-42.2007	-76.7308
10 kW	Conventional	264.1035	-3.2818e-04	-41.8215	-77.6332
	1	264.1919	0.0107	-41.2945	-76.9676
	2	264.6588	-3.7569e-04	-39.6798	-76.1714
	3	263.7935	0.0011	-42.6814	-77.5852
20 kW	Conventional	267.8721	-0.0057	-41.6127	-78.5431
	1	268.0498	8.3589e-04	-40.5302	-77.4013
	2	268.8906	-3.6787e-04	-37.5062	-75.8299
	3	267.2738	6.7121e-04	-43.2487	-78.6337
2 kW (Q injection)	1	266.1534	9.6020e-04	-44.1818	-75.2907
	2	265.7802	-7.3929e-04	-44.8198	-72.7575
	3	266.6989	0.0167	-43.0602	-78.4341
10 kW (Q injection)	1	268.6480	0.0101	-43.2701	-75.8536
	2	268.6875	-0.0039	-42.5687	-73.1563
	3	268.8043	0.0163	-43.4219	-79.0740
18 kW (Q injection)	1	269.5454	0.0094	-41.6948	-76.7685
	2	270.0915	-0.0036	-39.4356	-74.4682
	3	269.1333	0.0049	-43.5525	-79.1669

kW, and the simulation results are recorded for each power point. The simplified system ran with each of the strategies studied, including the conventional one that does not consider the negative components, in addition to considering the injection of reactive power. Furthermore, by using expression (5.7) for losses and the data presented in Table 5.3, it is possible to compute the losses for the entire electrical distribution grid by adding the values obtained for each distribution line.

The losses were organized in graphs displayed in Figure 5.14. These graphs represent the power dissipated in all electrical lines for each of the studied strategies by varying the input power and injecting reactive power when possible. Those results are for the simplified system connected to bus 5.

The lower the power dissipated in the electrical grid, the better the result for this quantity. In this sense, the electrical grid presented lower global losses when strategy 3 runs in the PV system injecting active and reactive power (PQ3 graph), as shown in Figure 5.14. The lowest value recorded is 2.214 kW for an injection of 18 kW and 8.717 kvar. Taking the conventional strategy as a parameter and the same input power point, that is,

Table 5.2 – Voltage vectors for bus 5 in the double synchronous reference frame (system connected to bus 7)

Input power	Strategy	v_d^+	v_q^+	v_d^-	v_q^-
2 kW	Conventional	260.9748	1.5445e-05	-41.9783	-76.8896
	1	260.9938	-6.2383e-04	-41.9204	-76.6042
	2	261.0935	-6.3053e-04	-41.5800	-76.4482
	3	260.9128	-6.2095e-04	-42.2002	-76.7273
10 kW	Conventional	264.0328	-2.9337e-05	-41.8194	-77.6234
	1	264.1129	-6.8272e-04	-41.2899	-76.9697
	2	264.5439	0.0103	-39.7268	-76.2220
	3	263.7265	-0.0098	-42.6790	-77.5580
20 kW	Conventional	267.6606	8.5138e-04	-41.5959	-78.5161
	1	267.8208	-1.6865e-04	-40.5343	-77.3946
	2	268.5486	-0.0115	-37.7062	-75.9705
	3	267.0840	-0.0111	-43.2313	-78.5534
2 kW (Q injection)	1	266.0713	-4.0188e-04	-44.2020	-75.2839
	2	265.7236	2.8606e-04	-44.7395	-72.7442
	3	266.5825	7.2776e-04	43.0550	-78.4058
10 kW (Q injection)	1	268.5355	6.7769e-04	-43.2785	-75.8517
	2	268.5745	-6.0111e-04	-42.5279	-73.2535
	3	268.6806	-4.8530e-04	-43.4133	-79.0376
18 kW (Q injection)	1	269.3702	-5.8445e-04	-41.6961	-76.7657
	2	269.8428	-5.8905e-04	-39.5417	-74.6385
	3	268.9798	-0.0016	-43.5662	-79.1095

Table 5.3 – Cable parameters

| AWG cable 3x1	
Resistance (Ω/km @55°C)	0.975
Frequency	60 Hz
Line length	40 m
R/X ratio	100
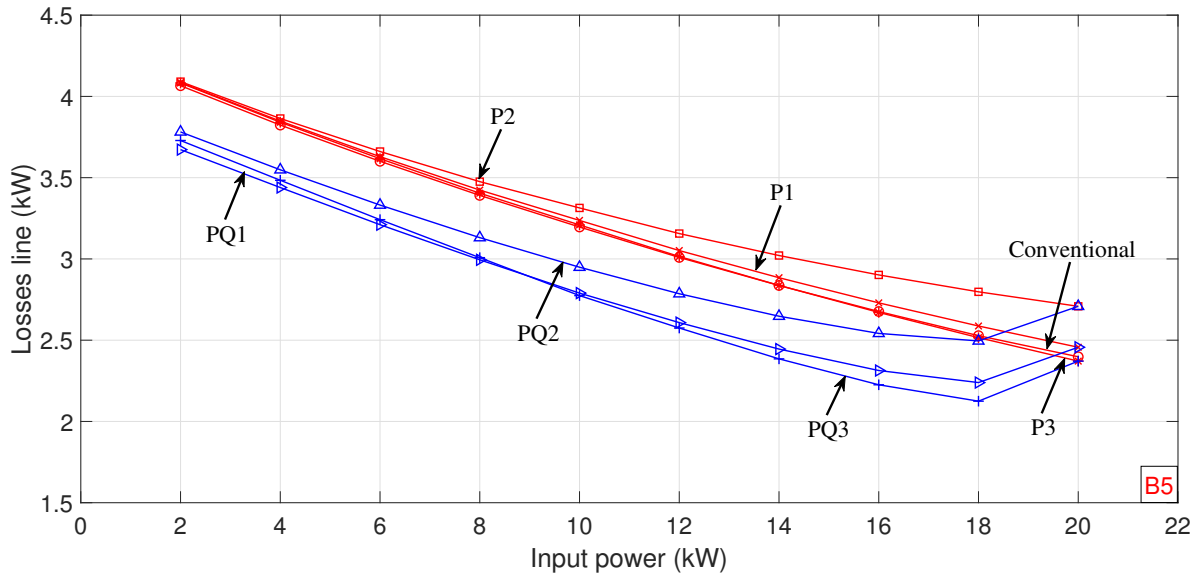
Figure 5.14 – Graphs for the power losses along the grid when PV system is connected to bus 5. P1, P2, and P3 are graphs for strategies 1, 2, and 3 injecting only active power; PQ1, PQ2, and PQ3 are graphs for strategies 1, 2, and 3 injecting both active and reactive powers.

18 kW, it is concluded that strategy 3 has 15.94% fewer losses, considering that the value for the conventional one is 2.527 kW. Strategy 1 (PQ1 graph) has the second-best mark with a value of 2.239 kW, having an advantage of 11.41% over the conventional strategy. Strategy 2 (PQ2) has the highest value of losses among those that present reactive power injection, with a value of 2.495 kW but remains 1.28% lower than the conventional value.

Besides, considering the graphs in Figure 5.14 that represent a scenario without the reactive power injection, strategy 3 (P3) is the only one with a lower value than the conventional one, with a difference of 0.48% given by 2.515 kW of losses. The highest overall losses, considering with and without reactive power injection, occur with strategy 2, which has 10.67% more than the conventional one with a value of 2.797 kW. And strategy 1 has 2.35% more losses with a value of 2.587 kW.

On the other hand, imagining a scenario of more shading and, consequently, lower input power, the strategy that proved to be better is 1 with the injection of reactive power (graph PQ1 in Figure 5.14). This situation remains until the input power reaches 10 kW, which is when strategy 3 becomes the best, according to graph PQ3 in Figure 5.14.

Now, graphs are shown in Figure 5.15 for the electrical losses in the whole grid when the PV connection is made at bus 7. The intention here is to validate and compare the PV system efficacy when it is connected to bus 5 or 7. Hence, the simulation scenarios made for the system connection on bus 5 were repeated.

The behavior of the graphs presented in Figure 5.15 is very similar to those in Figure 5.14, which is expected once the simulations performed for both situations have
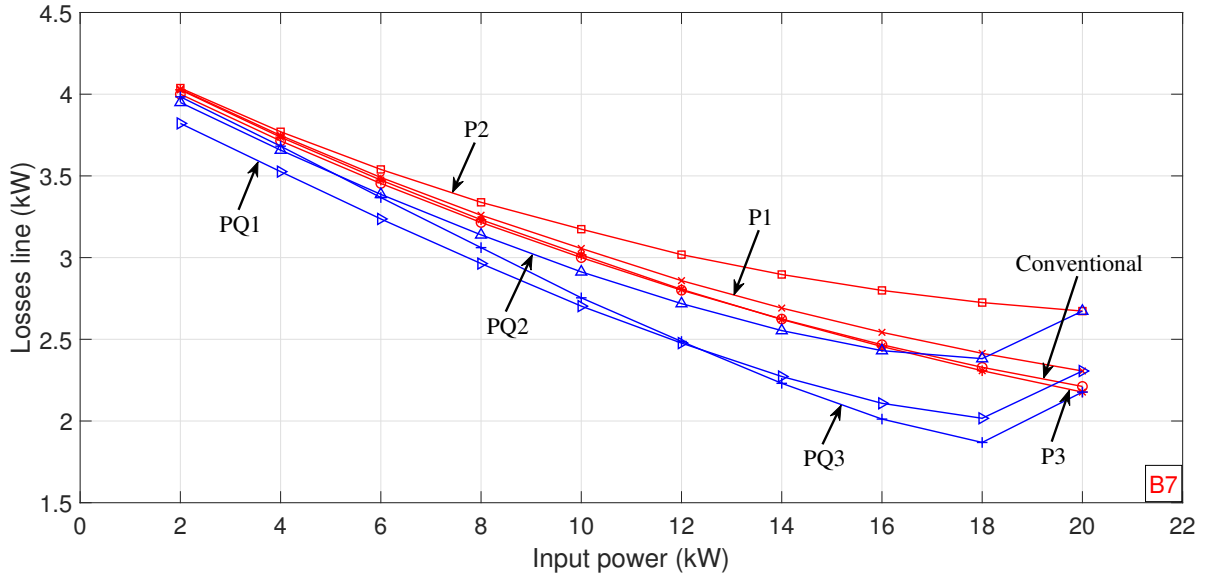
Figure 5.15 – Graphs for the power losses along the grid when PV system is connected to bus 7. P1, P2, and P3 are graphs for strategies 1, 2, and 3 injecting only active power; PQ1, PQ2, and PQ3 are graphs for strategies 1, 2, and 3 injecting both active and reactive powers.

the same parameters and grid settings. Hence, strategy 3 with reactive power injection (graph PQ3) continues to have the lowest overall value for losses at the 18 kW (with 8.717 kvar reactive injection) operating point, which is 1.8 kW. The PV system running strategy one (1) at the same operating point has the second lowest loss value, 2.1 kW. Among the simulations with reactive injection, the worst global result was strategy 2 (graph PQ2) with the value of 2.4 kW, behind strategy three (3) without reactive injection (graph P3) with 2.3 kW losses at the point of 18 kW operation, which is the same regarding the input power. Considering loss graphs when there is no reactivation injection, strategies three (3) and conventional have the lowest values, 2.3 kW and 2.35 kW, respectively. When the system operates with strategy 1, the grid has 2.5 kW of losses which is the third best global mark, ahead of strategy 1 with 2.6 kW.

Also, considering the loss graphs of Figure 5.15 when there is no reactive injection, strategy 3 has the lowest value of 2.3077 kW, which is $0,9\%$ lower than the conventional value of 2.3286 kW. When the system operates with strategy 1, the grid has 2.4141 kW of losses which is $3,67\%$ greater than the conventional one, but still ahead of strategy 2, whose value of 2.7248 kW is $17,01\%$ greater.

Still observing Figure 5.15 and concerning the operation in non-ideal conditions, that is, with the lower input power due to the phenomena inherent to the PV system, the strategy that appears to be the best option for reducing losses is 1 with injection of reactive power. This strategy presents the lowest values of losses up to the point of 12 kW, approximately. From that point on, the best option is strategy 3, also with reactive injection.

5.6   CONCLUSIONS OF THE STUDIES

Voltage unbalances in the studied electrical grid bus are smaller when strategy 2 is applied to the PV system, as shown in Figures 5.12 and 5.13. And this occurs when there is or is not a reactive power injection. Furthermore, strategy 3 and conventional one does not present significant changes in these unbalance factors, as their index keeps static throughout the input power variation.

Regarding losses, the positioning is inverted, and strategy 3 is the top one, as shown in Figures 5.14 and 5.15. Also, the injection of reactive power into the grid improves the power factor, so an improvement in electrical losses is observed when the PV system performs such an injection. Hence, all strategies have the lowest losses in this situation. The one with the highest loss values is strategy 2. Differently from what happens with the unbalance factors, strategy 2 is the one that has the highest losses.

Another conclusion from voltage unbalances and losses refers to the connection of the PV system to the electrical grid studied. For the specific studied scenario, the best connection point for the PV system is at the end of the grid, i.e., at bus 7. This deduction is based on the unbalance values presented in Table 5.4 for when the PV system is connected to Bus 5 (column B5 in the table) and Bus 7 (column B7 in the table). The values refer to the operating point of 18 kW of PV system input power. Column B7 of Table 22 presents values lower than column B5, hence connecting the PV system to Bus 7 implies lower voltage unbalances in the electrical grid. For example, the unbalance value for strategy 2 for B7 is 4% lower than for B5.

Table 5.4 – Unbalance factors when the PV system is connect to bus 5 and 7

Strategy	Unbalace factor	
	B5	B7
Conventional	0.3360	0.3324
1	0.3266	0.3205
2	0.3163	0.3043
3	0.3352	0.3351
1 (Q injection)	0.3239	0.3178
2 (Q injection)	0.3119	0.3001
3 (Q injection)	0.3353	0.3347

Furthermore, Table 5.5 displays the values for losses at the 18 kW operating point of the PV system when it is connected to bus 5 and bus 7. For this table, all values in column B5 are greater than those in the B7. And the strategy that presents the utmost difference is 3 with reactive injection, whose loss value when the system is at bus 7 is 13.7% lower than when it is at bus 5. Therefore, the results for losses also corroborate with the deduction that the PV system connected further from the primary source, i.e., at bus 7 of the studied grid, causes improvements in the measured indices.

Table 5.5 – Losses when the PV system is connect to bus 5 and 7 (operating point 18 kW)

Strategy	Line losses	
	B5	B7
Conventional	2.527 kW	2.328 kW
1	2.587 kW	2.414 kW
2	2.797 kW	2.724 kW
3	2.515 kW	2.307 kW
1 (Q injection)	2.239 kW	2.016 kW
2 (Q injection)	2.495 kW	2.381 kW
3 (Q injection)	2.124 kW	1.868 kW

5.7 TYPE C FAULT

Different types of electrical faults cause different voltage sag reactions in the grid (BOLLEN; ZHANG, 2003). Selecting these faults with distinct characteristics is a way to verify if there are differences in the performance of the controls developed here in the face of voltage sag variation. In this sense, the fault chosen was the one that leads to a type C sag that has phase voltages with sags different from that of type D, in addition to not having zero sequence elements. Also, the voltages of each phase were computed taking into account the same characteristics for the pre-fault ($\vec{E} = 13.8\angle0°$ kV) and during-fault ($\vec{V} = 0.5\vec{E}$) voltage vectors used for the D fault, following Table 5. Hence, the primary source input voltages during the voltage sag are given by

$$E_{g1} = V_1 = 13,8\angle0° \tag{5.8}$$

$$E_{g2} = V_2 = 9,1278420\angle-139.106° \tag{5.9}$$

$$E_{g3} = V_3 = 9,1278420\angle139.106° \tag{5.10}$$

Table 5.6 – Type C sag

Type	V_1	V_2	V_3
C	$\vec{E}$	$-\dfrac{1}{2}\vec{V} - j\sqrt{3}\dfrac{1}{2}\vec{E}$	$-\dfrac{1}{2}\vec{V} + j\sqrt{3}\dfrac{1}{2}\vec{E}$

The voltage phasors represented in expressions 1, 2, and 3 are introduced in the primary power source of the electrical grid with 7 bars to carry out the simulations and gather the results. The form of these voltages can be seen in Figure 5.16.

Next, some results of electrical quantities are shown related to the simplified PV system running the control strategies and the type C sag applied to the primary source. As the intention is to validate the system operation, the results are only for the scenario with 100% of active power injected into the grid. Furthermore, a comparison is made between
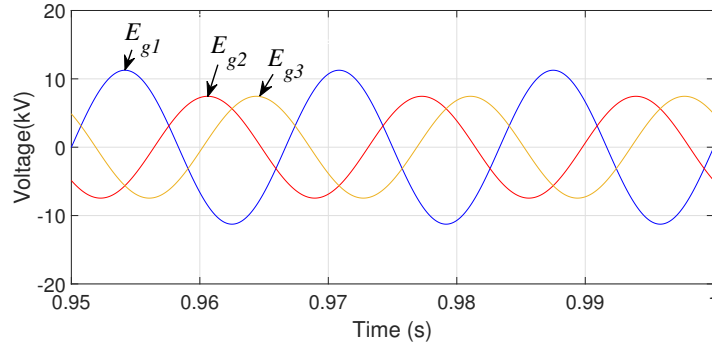
Figure 5.16 – Voltages for the primary power source of the grid with type C sag

these results and those obtained for type D fault to verify if there are differences in the performance of the simplified system.

5.7.1 Strategy 1

Figures 5.17 (a) and (b) show the voltage curves of the DC link of the simplified system running strategy 1. It can be seen from these images that the system with strategy 1 works correctly when a sag with type C characteristics is applied to the electrical grid since the desired value of 1200 V for the voltage is established, and there are no differences between the curves.

(a)   (b)
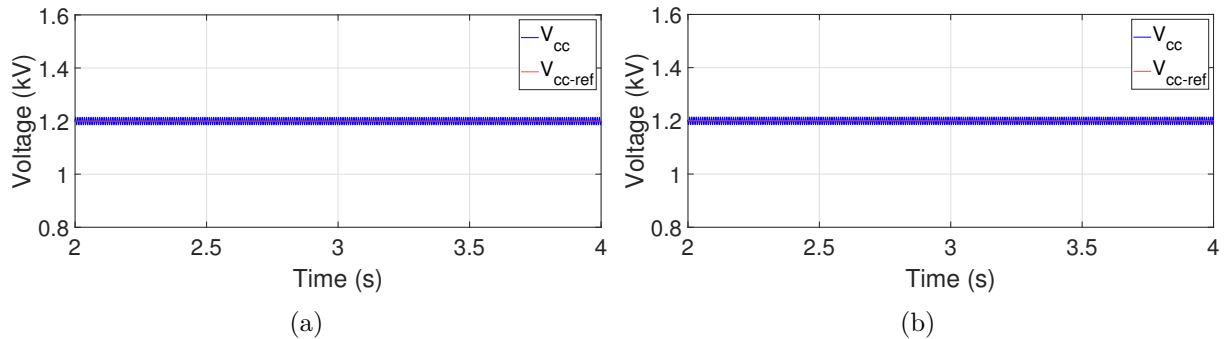
Figure 5.17 – DC-link voltage for strategy 1 and type (a) C and (b) D sags

The currents injected into the grid are the targets for strategy 1, which aims to make them fully balanced. Therefore, these currents can be observed in Figures 5.18 (a) and (b) for type C and D sags. All the current curves in these figures are sinusoidally identical, but there are slight differences in the RMS values. For example, phase 1 of the current for type C sag has 44.7 A of RMS value, and the same phase has 43.4 a for type D, which generates a difference of only 3%.

The active powers shown in Figures 5.19 (a) and (b) present differences in their oscillation curves restricted only to their phase, as they have the same peak value of 26.5 kW. In addition, the reactive powers of Figures 5.19 (c) and (d) also show this pattern, as they differ in phase angle but have the same peak value of 6.5 kvar. The explanation for this phase difference lies in the voltage phasors that are different for type C and D sags.

Figure 5.18 – Injected currents into the grid by the simplified PV system for type (a) C and (b) D sags.

Figure 5.19 – Active power for type (a) C and (b) D sags; reactive powers for type (c) C and (d) D sags.

5.7.2 Strategy 2

The voltages for the DC link of the three-phase inverter can be seen in Figures 5.20 (a) and (b). These voltages refer to the scenarios in which the simulations ran with type C and D sags, additionally the application of strategy 2 in the simplified system. The voltages reached the value of 1200 V established by the control system, which shows the good functioning of the simplified PV system for the type C fault.

For different sag types, it is expected that changes in the responses of the PV system would occur when dealing with these sags. In this way, the currents injected by the simplified PV system when dealing with type C and D sags are contrasting in phase and RMS values, as seen in Figures 5.21 (a) and (b). The RMS values for phase 1 are 42.6 A (type C) and 56.3 A (type D), which generates a difference of 32%, for phase 2 are 61.8 A (type C) and 32.5 A (type D), whose difference is 90%, and for phase 3 are 41.3 A
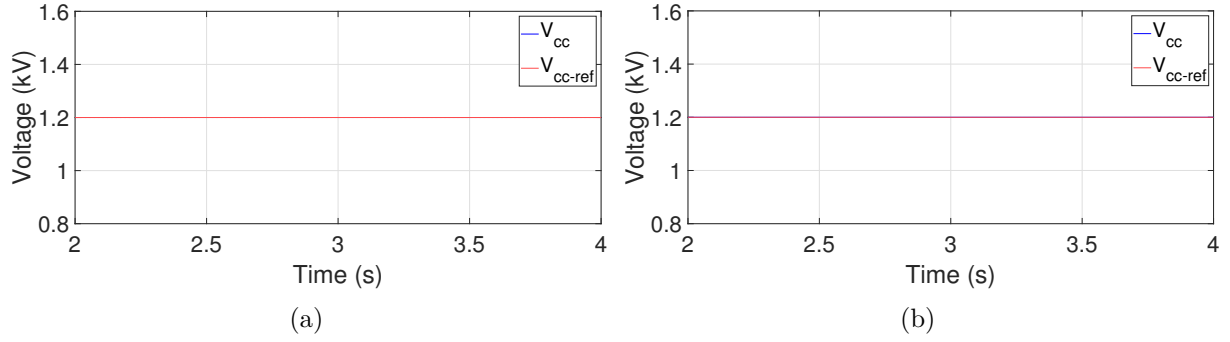
Figure 5.20 – DC-link voltage for strategy 2 and type (a) C and (b) D sags

(type C) and 57.2 A (type D), resulting in a difference of 38.5%. Again, these divergences happen due to the distinctive voltage phasors for each type of sag that influence how the control system modifies the currents injected into the grid. Also, these currents change according to the applied strategies that depend on these voltages at the connection point.
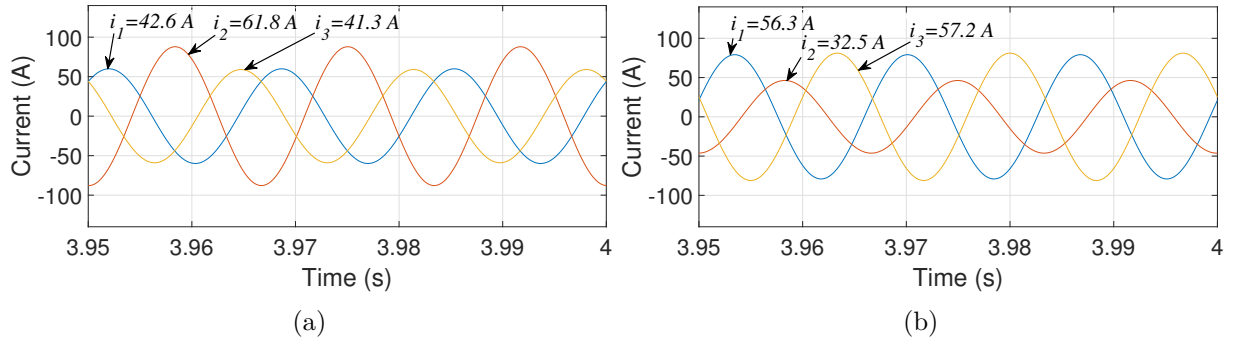
Figure 5.21 – Injected currents into the grid by the simplified PV system for type (a) C and (b) D sags.

As strategy 2 aims to reduce active power oscillations, this quantity must be shown to verify whether or not the control is reaching its established objective. Therefore, Figures 5.22 (a) and (b) show the active powers for type C and D sag, respectively. Note that both simulations act as expected, as their active power is at 20 kW with almost zero oscillations. And for the reactive power, there are differences only in the phase due to the divergent three-phase currents and voltages, but the peak value is 13.9 kvar for both, as shown in Figure 5.22 (c) and (d).

5.7.3 Strategy 3

The DC-link voltages of the simplified system running strategy 3 are displayed in Figures 2 and 3 for the types C and D sags, respectively. The 1200 V value for the quantities demonstrates that the PV system works well with the type C sag same as the D sag.

The sinusoidal currents have distinct RMS and phase values, as shown in Figures 5.24 (a) and (b) for sag C and D, respectively. In this sense, phase 1 has a percentage
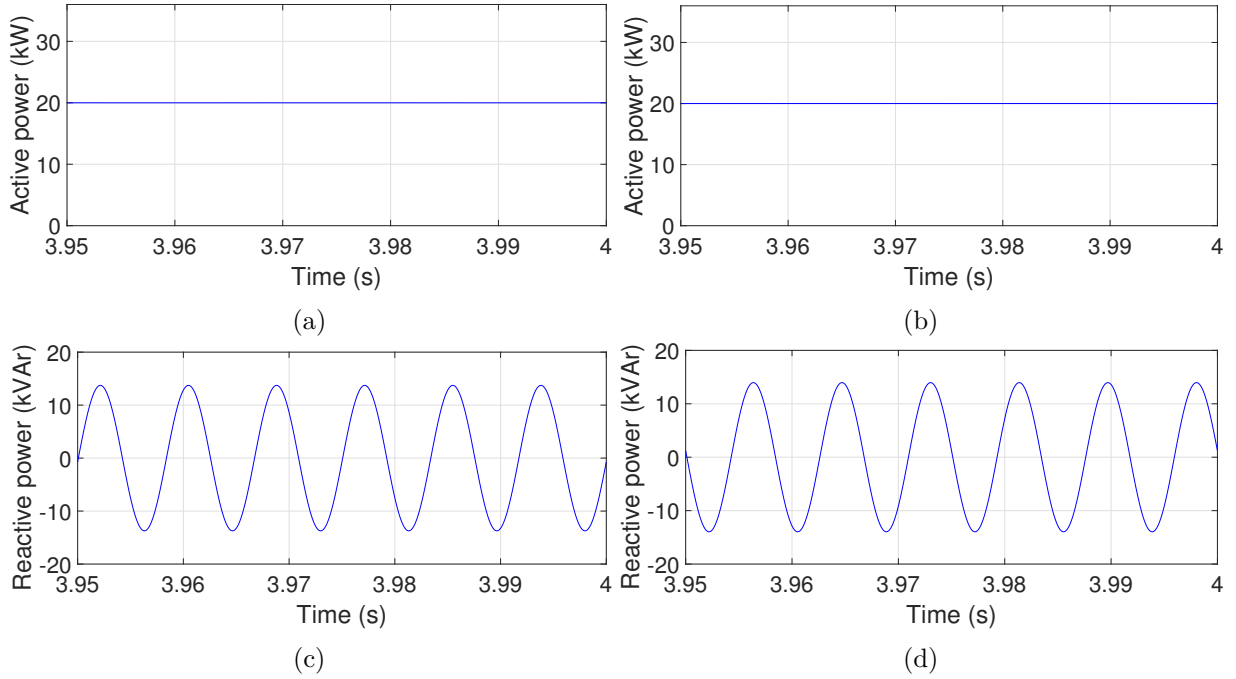
Figure 5.22 – Active power for (a) simplified and (b) complete models when the strategy 2 is applied.
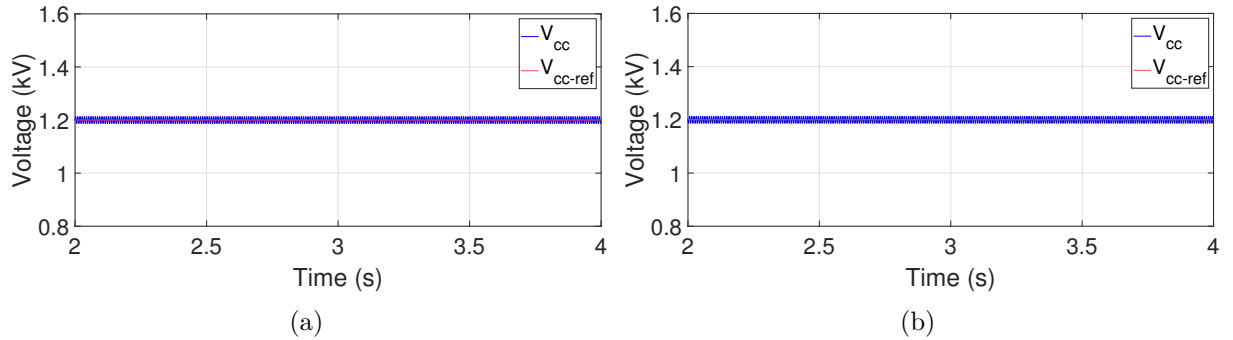
Figure 5.23 – DC-link voltage for strategy 3 and type (a) C and (b) D sags

difference of 36%, phase 2 has 100%, and phase 3 has 37.8%.

The active power injected into the grid by the simplified system running strategy 3 has angular phase differences when the grid is under a C or D sag, as shown in Figures 5.25 (a) and (b), but the peak values of 32.1 kW are the same. Also, the reactive powers shown in Figures 5.25 (c) and (d) confirm the proper performance of the simplified system running strategy 3 for type C sag. These figures prove that the strategic objective of reducing reactive power oscillations is achieved.

5.7.4 Unbalance factor curves for type C sag

As a starting point, the unbalance caused by the type C sag is determined using the unbalance factor expression given by 4.4. Thus, the unbalance factor for this type of
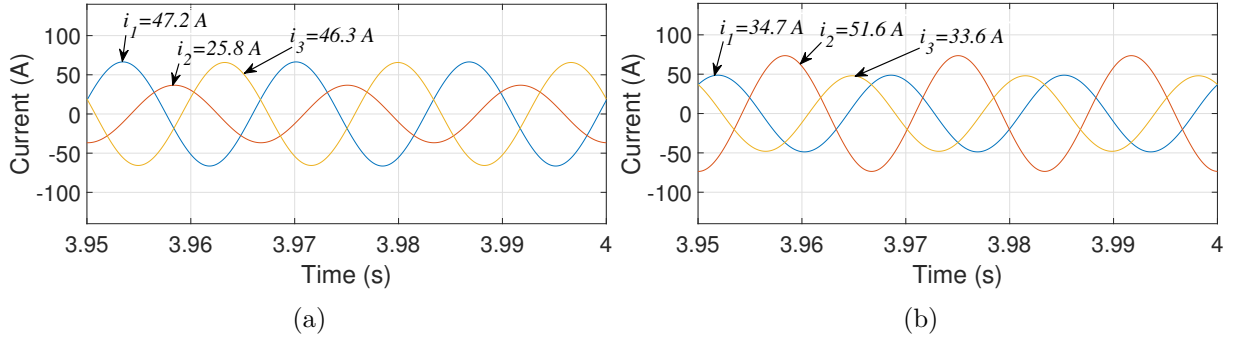
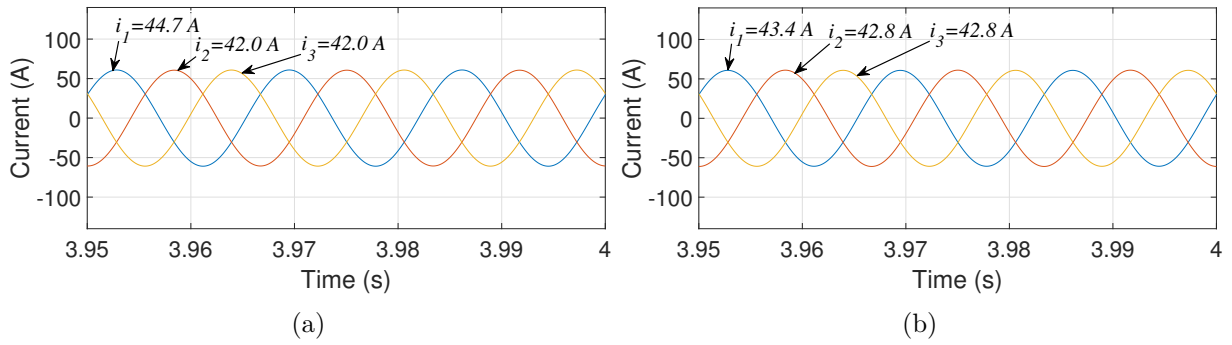Figure 5.24 – Injected currents into the grid by the simplified PV system for type (a) C and (b) D sags.

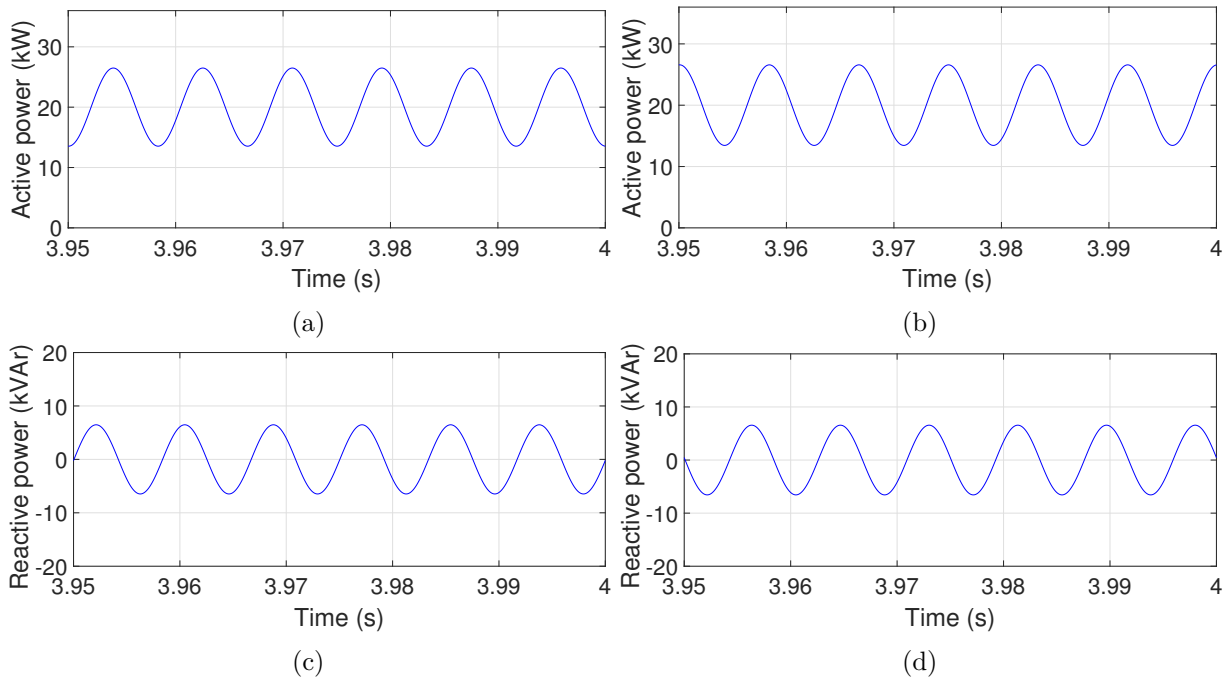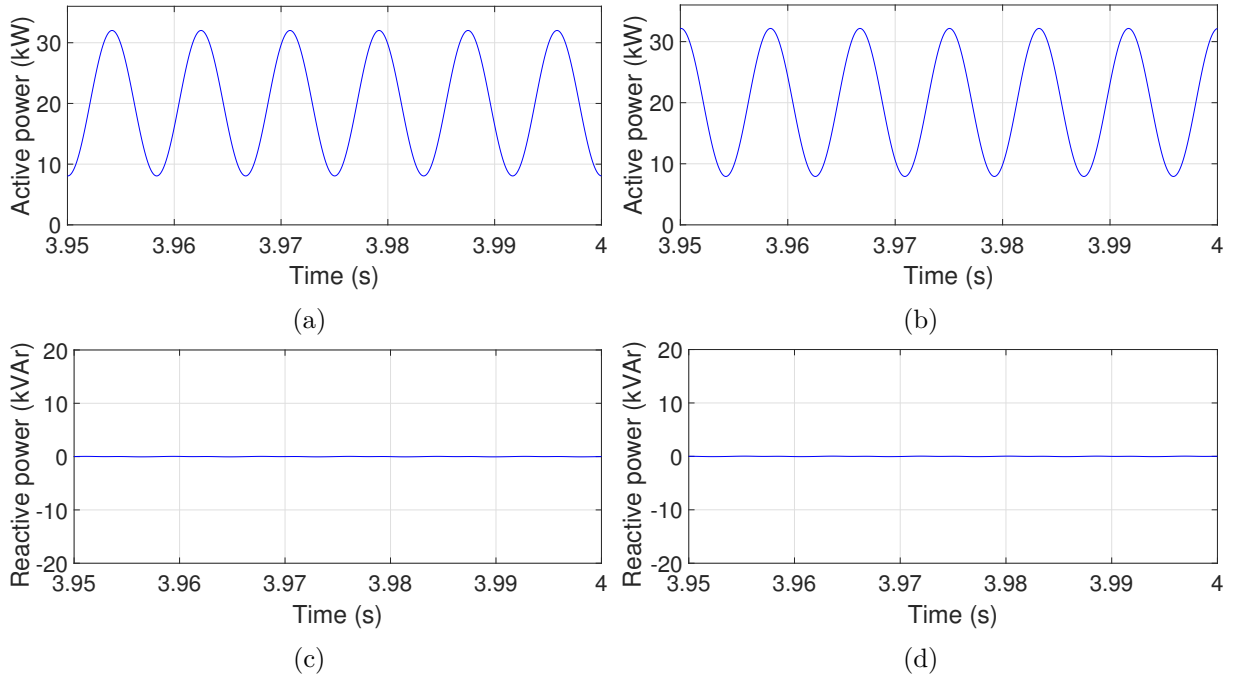Figure 5.25 – Reactive power for (a) C and (b) D sags when strategy 3 is applied to the simplified system.

fault is

$$n = \frac{V^-}{V^+} = \frac{3,449.93}{10,350.02} = 0.333 \tag{5.11}$$

The simulations carried out for the analysis of unbalance factors for type D sag were made for type C. Thus, the input power of the PV system was varied, considering the injection of reactive power, in addition to the change of the bus in which the PV system is connected. Also, the analyzes were made for the last bar of the system, which is 7, as was done previously.

All results for the unbalance factors of bus 7 obtained through simulations with type C sag can be seen in Figure 22, and these results are for the situation of connection of the PV system at bus 5. The curves are plotted for the unbalance factors as a function of the PV system input power, and all strategies were considered.
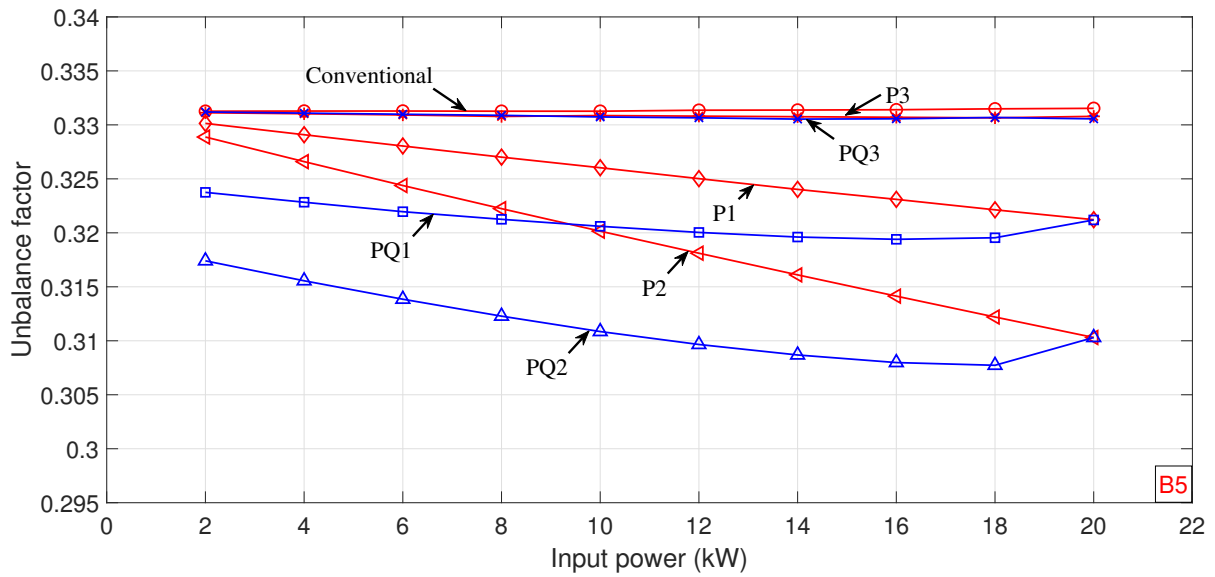
Figure 5.26 – Graphs for the unbalance factors at bus 7 when PV system is connected to bus 5 and the grid is under a type C sag. P1, P2, and P3 are graphs for strategies 1, 2, and 3 injecting only active power; PQ1, PQ2, and PQ3 are graphs for strategies 1, 2, and 3 injecting both active and reactive powers.

As with type D sag, the results presented in Figure 5.26 for sag C indicate that the strategy that best acts in the amortization of unbalances continues to be strategy 2, more than that, it is when the reactive injection (PQ2 curve) occurs that it appears in its best form. The value of 0.3077 is the best for the unbalance factor of the PQ2 curve at the point 18 kW (active) and 8.517 kvar (reactive). The second best is the curve P2 with 0.3122 at the same point. Besides, the worst performance belongs to conventional with a unbalance factor of 0.3315. Strategy 3 remains with its curves constant with or without reactive injection (PQ3 and P3 curves), as happened to D sag, and their values are close to those presented by the conventional strategy.

The curves displayed in Figure 5.27 are the results gathered for the unbalance factors when the PV system is connected to bus 7.

As with the connection at bus 5, the curves in Figure 5.27 demonstrate that strategy 2 with reactive injection (PQ2) presents the best result for the factor analyzed along the power variation, as the best global value with 0.2962 at point 18 kW and 8,517 kvar. The rest of the curves also behave similarly to those in Figure 5.26, only changing the global values for the factor that are smaller. Strategy 2 without reactive injection keeps as the second best option for unbalances, with the lowest value of 0.3003. On the other hand, there is a tiny difference regarding the curve of the conventional strategy, which slightly improves compared to that shown for D sag, but the curves P3 and PQ3 are still very similar to it, and they are the ones with the highest value for unbalances.

In summary, the figures shown here for the unbalance factors indicate that there are no major differences between the performance of the control system when the electrical
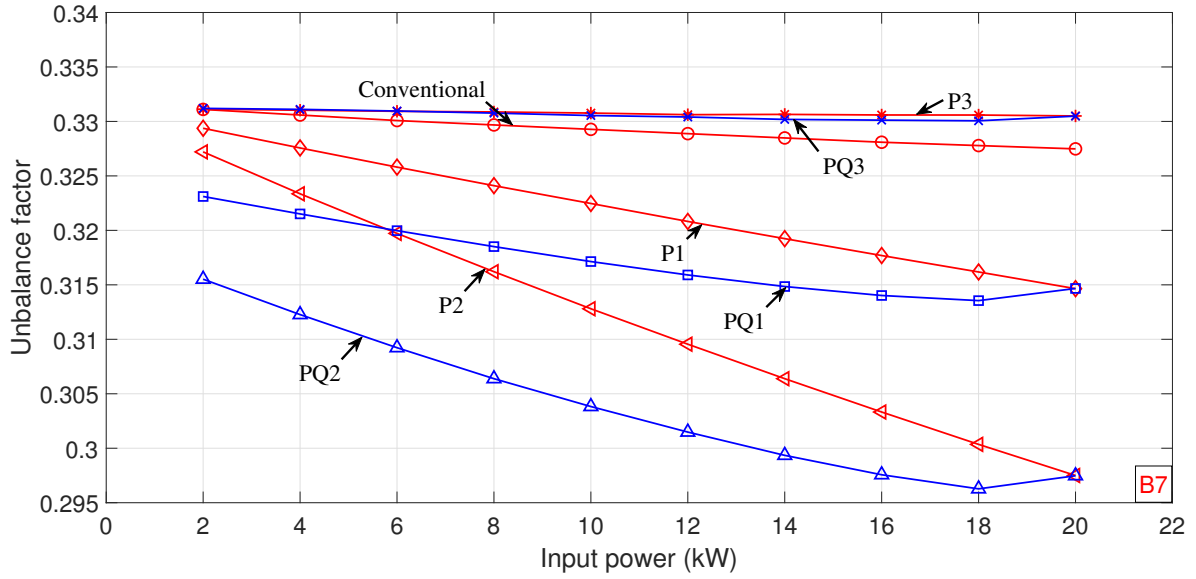
Figure 5.27 – Graphs for the unbalance factors at bus 7 when PV system is connected to bus 7 and the grid is under a type C sag. P1, P2, and P3 are graphs for strategies 1, 2, and 3 injecting only active power; PQ1, PQ2, and PQ3 are graphs for strategies 1, 2, and 3 injecting both active and reactive powers.

grid is under different types of sags. Type C and D present differences between their characteristics, and it was through these differences that it was possible to infer that the control strategies can act satisfactorily.

5.7.5 Line loss analisys for type C sag

All the characteristics and considerations taken for the D sag simulations were also used to gather the results of the electrical losses in the grid when it is under the effect of C sag.

The losses were gathered in curve graphs shown in Figure 5.28, and each one refers to a specific simulation setting. These graphs represent the power dissipated along the grid for each of the studied strategies by varying the input power and injecting reactive power when possible. Those curves concern the simplified system connected to bus 5.

From figure 5.28, it is possible to infer that the same curve behaviors of figure 5.14 repeat here. It is noted that strategy 3 with reactive injection maintains the best performance for losses, as it presents the lowest values for this quantity. The smallest value of the PQ3 curve is 2.064 kW at point 18 kW with 8.517 kvar injection. All strategies with reactive power injection had better results than those without injection. On the other hand, strategy 2 was the one that presented the worst result of all, with the value of 2.54 kW being the highest among the lowest values.

With the PV system connected to bus 7, the results for the line losses are organized in graphs that can be seen in Figure 5.29.
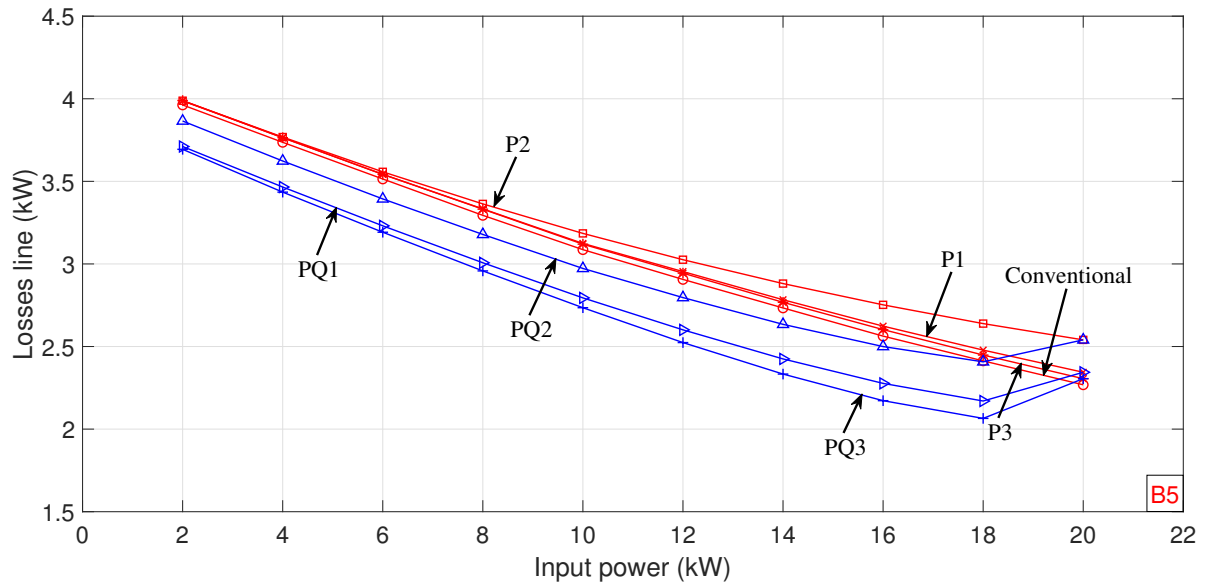
Figure 5.28 – Graphs for the power losses along the grid when PV system is connected to bus 5 and C sag. P1, P2, and P3 are graphs for strategies 1, 2, and 3 injecting only active power; PQ1, PQ2, and PQ3 are graphs for strategies 1, 2, and 3 injecting both active and reactive powers.
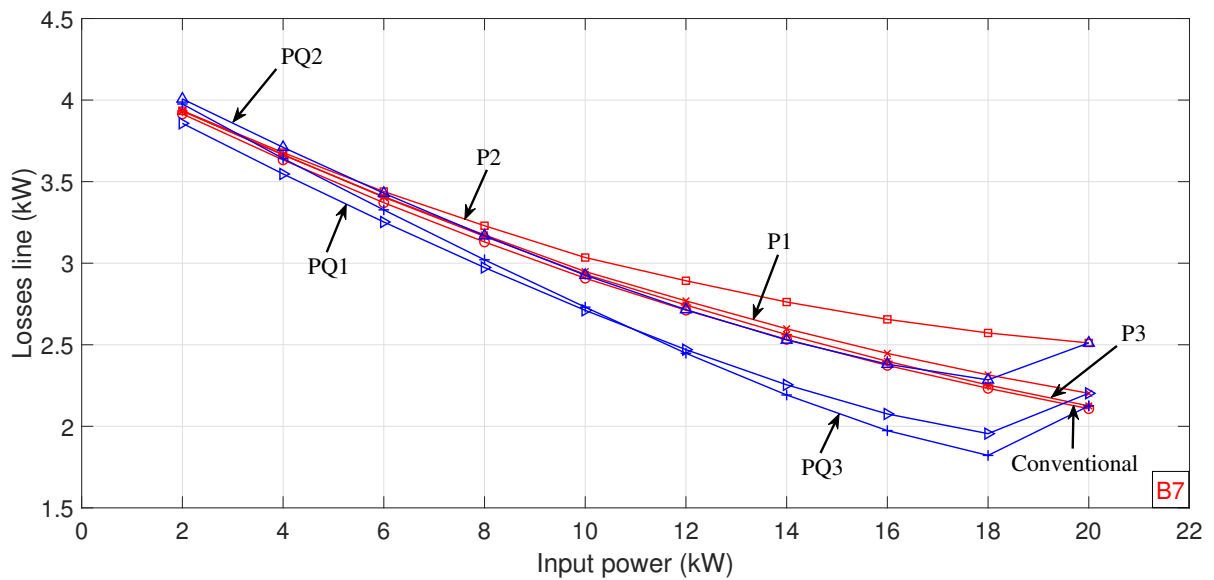
Figure 5.29 – Graphs for the power losses along the grid when PV system is connected to bus 7 and C sag. P1, P2, and P3 are graphs for strategies 1, 2, and 3 injecting only active power; PQ1, PQ2, and PQ3 are graphs for strategies 1, 2, and 3 injecting both active and reactive powers.

Strategy 3 with reactive power injection remains the best option for losses, as shown in Figure 5.27 since the lowest recorded value (1.821 kW) among all scenarios belongs to it. All curves showed similar behavior, except for PQ1, which has the second-best mark of 1.955 kW, and P2 has the worst overall result of 2.51 kW.

5.7.6   Analysis conclusion for type C sag

As for D sag, the unbalance factors reduce when strategy 3 is applied to the PV system, especially with reactive power injection. And as for losses, strategy 2 is the one that cuts down those undesired but inevitable electrical quantities that can be mitigated.

The unbalance factors for C sag are gathered in Table 5.7, and refer to the simulation results when the PV system at 18 kW input power is connected to bus 5 and bus 7. The B7 column values are tinner when compared to the B5 column, thus indicating that the connection in bus 7 is the best option to reduce the unbalances in the grid. Furthermore, the losses were also gathered in Table 5.8, and the same behavior is observed, as the values of column B7 are smaller than column B5. Therefore, the best connection point of the PV system is at the end of the electrical grid, at bus 7, as was the case for sag D.

Table 5.7 – Unbalance factors when the PV system is connect to bus 5 and 7

Strategy	Unbalace factor	
	B5	B7
Conventional	0.3314	0.3277
1	0.3221	0.3161
2	0.3122	0.3003
3	0,3306	0.3305
1 (Q injection)	0.3195	0.3135
2 (Q injection)	0.3077	0.2962
3 (Q injection)	0.3306	0.3300

Table 5.8 – Losses when the PV system is connect to bus 5 and 7 (operating point 18 kW)

Strategy	Line losses	
	B5	B7
Conventional	2.413 kW	2.2328 kW
1	2.478 kW	2.315 kW
2	2.638 kW	2.572 kW
3	2.448 kW	2.253 kW
1 (Q injection)	2.170 kW	1.955 kW
2 (Q injection)	2.407 kW	2.284 kW
3 (Q injection)	2.064 kW	1.821 kW

It is possible to conclude that the control system is robust enough to deal with two types of voltage sags caused by electrical faults through the results obtained for

voltage losses and unbalances for C and D sags. Furthermore, the control strategies worked following their proposals, as the PV system could inject power into the grid according to the commands by the control structure.

5.8   CONCLUSION

In this section, the results for the simplified PV system were presented, which is faster and made it possible to obtain more results for the analysis completed. This simplified system has ideal controlled voltage sources that replaced the boost converter and the non-ideal IGBTs switches of the three-phase inverter, providing higher processing speed. Besides, all the strategies 1, 2, and 3 studied in this work were tested in this simplified system.

It is concluded through the analysis of the graphs that strategy 2 is the one that best deals with voltage unbalances, as it presents the lowest values for this analyzed index. In this way, the chosen comparison parameter value for unbalance factor is 0.3324 when the PV system runs the conventional strategy. This value was recorded when the PV system operates at the 18 kW point and is connected to bus 7 of the grid under a type D voltage sag. Therefore, the unbalance factor at bus 7 of 0.3001 is 9.7% smaller when the PV system runs strategy 2 with reactive power injection. Without this injection, the unbalance factor value is 0.3043, which represents a decrease of 8.45%. The unbalance at bar 7 when the system runs strategy 1 is 0.3178 (with Q injection) and 0.3205, representing a decrease of 4.78% and 3.58%, respectively. Finally, the unbalance factor is 0.3347 (with Q injection) and 0.3351 for the PV system running strategy 3, indicating a negligible increase of 0.7% and 0.83%. Therefore, this last strategy is the one that presents the worst results for the unbalance factors.

The grid has the lowest line losses when strategy 3 is applied to the PV system. To verify the advantage of this strategy for losses, the conventional strategy is also taken as a benchmark at the 18 kW operating point for the PV system connected to bus 7, and the loss value recorded in this situation is 2.328 kW. The electrical grid presents losses of 1.868 kW when strategy 3 is applied, and the reactive power injection is performed, which represents a decrease in this electrical quantity of 19.75%. In addition, it presents a 0.9% loss reduction for the same strategy, but without Q injection. The second best record is 2.016 kW, as there is a reduction of 13.4%, which happens for the PV system running strategy 1 and injecting reactive power. Without the Q injection, the losses are 2.414 kW, representing an increase of 3.67%. The PV system running strategy 2 and injecting reactive power increased losses by 2.27% with a value of 2.381 kW. Finally, the worst scenario is due to strategy 2 applied to the PV system without the injection of reagents, with a 17% increase in losses, which are 2.724 kW.

A general conclusion points out that the PV system running strategy 1 presents

the most balanced results for the analyzed indices, i.e., line losses and unbalance factors. This strategy is chosen the best because it has the most consistent results, positioning itself as the second best in the analyzed indices. Finally, the analysis concluded that the best connection point for the PV system is at the end of the electrical grid, in this case, at bus 7, since it was at this location that the values of losses and unbalances were lower than the values when the connection is in the bar 5.

6 CONCLUSIONS

In this work, three control strategies to make the connection between a PV system with a three-phase inverter and an electrical grid that presents unbalanced voltages were proposed and implemented with the aid of the computer simulation software Matlab/Simulink®. Cascade control has enough notoriety in inverter applications, being one of the most used and consists of a DC-link voltage outer loop with slower dynamics, and an internal control loop of the currents injected into the grid that has faster dynamics. Furthermore, PI-type controllers were selected for regulating both current and voltage control systems. As these controllers have better performance when working with constant signals, the Park Transform was applied to change from the natural reference 123 (sinusoidal) to the synchronous reference of the grid voltage (constant).

The mathematical model of the grid was presented for the balanced and unbalanced case, which facilitated the control analyses that needed to be done. The model served as a basis for elaborating the PV system control strategies for unbalanced grids, providing the essential current expressions for the elaboration. The three control strategies were based on a set of expressions obtained through the analysis of the grid in an unbalance scenario, and each one has different targets. Then, strategy 1 targets to eliminate the negative sequence components of the current injected into the grid, which arises due to unbalance, and their elimination makes such a quantity balanced. The second strategy aims to eliminate the active power oscillations that emerge for the same reason. Finally, the objective of strategy 3 is to eliminate reactive power oscillations.

Once the control strategies were established, the design of the control loops for an inverter connected to a balanced electrical grid was done. the conventional control was performed using the synchronous grid voltage reference frame, which allowed the proper use of PI controllers. Besides, steps involving the modeling of the control system for a three-phase inverter were seen, as determining the gains of the controllers of the current inner loop and voltage outer loop, as well as the PI gains of the PLL.

The main change between the control systems was the replacement of the internal current control loop with SRF by the double synchronous reference system (DSRF), which takes into account the appearance of the negative sequence component. The DSRF uses two structures almost identical to the one used in the current control loop for the balanced case, one to control the positive sequence component of the current and the other to control the negative sequence component. However, there is a difference in the cross decoupling terms of the negative sequence structure, which have opposite signs, as the axes in the synchronous frame of the negative sequence rotate in the opposite direction. Moreover, strategies 1, 2, and 3 were used together with this DSRF structure, and it was possible to see the performance of each one in the electrical quantities.

The simulated electrical grid has a total of 7 buses and an ideal primary source of power. The first simulations were performed using the complete PV system, i.e., with the panels, boost converter, and three-phase inverter, whose rated power is 20 kVA. Besides, the comparison between the control strategies took into account the same grid conditions, in which a hypothetical fault causes type D sag with specific voltage phasors. And these voltage phasors were inserted into the grid primary source to simulate voltage sag conditions. Then, the PV system was connected to bus 5 of the grid to observe the electrical quantities and impacts caused on the unbalanced grid by this connection. And to validate the functionality of the system and compare the results, this system was also connected to bus 7.

For both the connection at buses 5 and 7, the four strategies showed a good performance in regulating the DC-link voltage, presenting modest differences between them. Regarding the current injected into the grid, strategy 1 granted the best results by injecting a fully balanced current. Regarding active power, the one that presented the basal oscillations in this quantity was strategy 2. And concerning reactive power, strategy 3 showed a better performance with this electrical quantity by considerably decreasing its oscillations. Therefore, the three main strategies worked as expected in achieving their respective proposals.

The complete PV system was replaced by a simplified one composed of controlled voltage sources, leading to a substantial drop in simulation time and, consequently, a greater variety of simulations. In this sense, the simplified system was also connected to buses 5 and 7, as its input power was varied, reproducing the effects that physical systems suffer from variations in solar irradiance, temperature, and shading, for example. After the mentioned replacement, the voltages of the primary source were changed following the characteristic phasors of type C and D sags, because it was possible to visualize the performance of the simplified system for two types with different characteristics.

The input power variation, in addition to the possibility of injecting reactive power into the grid by the PV system, allowed two analyzes to be carried out on voltage unbalance factors and line losses in the electrical grid. Regarding the first analysis, the unbalance factors collected were from bus 7, which is the furthest from the primary source, being the weakest. The graphs assembled from the simulation results showed that the PV system can correct voltage unbalances when running strategy 2 and injecting reactive power. On the other hand, strategy 3 is the most ineffective in this regard along with the conventional one. These results were observed for both the system connected to buses 5 and 7. Furthermore, the roles are reversed regarding losses, and the PV system becomes more efficient in reducing them when running with strategy 3 together with reactive power injection. In the same sense, strategy 2 becomes the least effective concerning this matter.

A comparison was also made for the best connection point of the PV system along

the unbalanced electrical grid, and it was found that, between positioning on bus 5 or 7, the best option is the latter. It is because all the values observed for the losses and unbalance factors are smaller when the PV system is connected to this bus, evidencing that the best place to connect it is at bus 7.

The results obtained in the simulations prove and reinforce the accuracy of the proposed modeling methodology, showing that the assembled control structure can handle two different types of sag. And it was observed that the control model based on DSRF among the three control strategies correctly attenuates the negative-sequence components of the injected currents into the grid, and reduces the oscillations of active and reactive powers, which are harmful to the operation of the electrical grid. Furthermore, depending on the chosen strategy, there is a possibility to reduce line losses or voltage unbalances in the buses.

6.1 FUTURE WORKS

It is suggested for future works:

- Connect simultaneously more PV systems to the electrical grid;

- Apply the control strategies to the PV systems connected to the grid, diversifying the scenarios through alternating these strategies and analyzing the impacts caused on the electricity grid;

- Increase the size of the adopted electrical grid model, and a suggestion would be the IEEE 13-bus electrical grid;

- Couple an energy storage system to the PV system and apply the control strategies;

- Analyze the four-wire inverter by applying the strategies to see the differences between it and the three-wire in performance.

REFERENCES

AAMRI, F. E. et al. A new strategy to control the active and reactive power for single phase grid-connected PV inverter. *3rd International Renewable and Sustainable Energy Conference (IRSEC)*, 2015.

ABRADEE. A distribuição de energia. *Associação Brasileira de Distribuição de Energia Elétrica. Disponível em:< https://www.abradee.org.br/setor-de-distribuicao/a-distribuicao-de-energia/*, 2021.

AGENCY, I. E. *Data and statistics.* 2022. Disponível em: <https://www.iea.org/data-and-statistics/data-tables/?country=WORLDenergy=Electricity>.

ALAJMI, B. N. et al. A maximum power point tracking technique for partially shaded photovoltaic systems in microgrids. *IEEE Transactions on Industrial Electronics*, v. 60, n. 4, p. 1596–1606, 2013.

ALEXANDER, C. K.; SADIKU, M. N. *Fundamentos de circuitos elétricos.* [S.l.]: AMGH Editora, 2013.

ANEEL. *Energia solar.* Disponível em: <http://www2.aneel.gov.br/aplicacoes/atlas/energia_solar/3_2.htm>.

ANEEL, A. N. D. E. E. . Modulo 7 – cálculo de perdas na distribuição. *Procedimentos de Distribuição de Energia Elétrica no Sistema Elétrico Nacional – PRODIST*, 2021.

ANWARI, M.; HIENDRO, A. New unbalance factor for estimating performance of a three-phase induction motor with under-and overvoltage unbalance. *IEEE Transactions on energy conversion*, IEEE, v. 25, n. 3, p. 619–625, 2010.

BAGHER, A. M.; VAHID, M. M. A.; MOHSEN, M. Types of solar cells and application. *American Journal of optics and Photonics*, Science Publishing Group, v. 3, n. 5, p. 94–113, 2015.

BIRICIK, S. et al. Protection of sensitive loads using sliding mode controlled three-phase dvr with adaptive notch filter. *IEEE Transactions on Industrial Electronics*, v. 66, n. 7, p. 5465–5475, 2019.

BLAABJERG, F. et al. Overview of control and grid synchronization for distributed power generation systems. *IEEE Transactions on Industrial Electronics*, v. 53, n. 5, p. 1398–1409, 2006.

BOLLEN, M. H.; OLGUIN, G.; MARTINS, M. Voltage dips at the terminals of wind power installations. *Wind energy*, Wiley Online Library, v. 8, n. 3, p. 307–318, 2005.

BOLLEN, M. H.; ZHANG, L. Different methods for classification of three-phase unbalanced voltage dips due to faults. *Electric power systems research*, Elsevier, v. 66, n. 1, p. 59–69, 2003.

BRASIL, A. d. E. E. do. Agência nacional de energia elétrica. *Brasília: Aneel*, 2008.

BRITO, M. A. G. D. et al. Evaluation of the main mppt techniques for photovoltaic applications. *IEEE transactions on industrial electronics*, IEEE, v. 60, n. 3, p. 1156–1167, 2012.

CASTILLA, M. et al. Grid-fault control scheme for three-phase photovoltaic inverters with adjustable power quality characteristics. *IEEE Transactions on Power Electronics*, v. 25, n. 12, p. 2930–2940, 2010.

CHOI, H. et al. Performance of medium-voltage dc-bus pv system architecture utilizing high-gain dc–dc converter. *IEEE Transactions on Sustainable Energy*, v. 6, n. 2, p. 464–473, 2015.

CHOUBEY, P.; OUDHIA, A.; DEWANGAN, R. A review: Solar cell current scenario and future trends. *Recent Research in Science and Technology*, v. 4, n. 8, 2012.

CHOWDHURY, B. H.; SAWAB, A. W. Evaluating the value of distributed photovoltaic generations in radial distribution systems. *IEEE Transactions on Energy Conversion*, v. 11, p. 595–600, Sept. 1996.

CRESESB. *Tutorial de Energia Solar Fotovoltaica: Radiação Solar*. 2008. Disponível em: <https://www.cresesb.cepel.br/index.php?section=com_content&lang=pt&cid=301>.

DAI, X.; CHAO, Q. The research of photovoltaic grid-connected inverter based on adaptive current hysteresis band control scheme. In: IEEE. *2009 International Conference on Sustainable Power Generation and Supply*. [S.l.], 2009. p. 1–8.

ELAVARASAN, R. M. et al. Investigations on performance enhancement measures of the bidirectional converter in pv–wind interconnected microgrid system. *Energies*, Multidisciplinary Digital Publishing Institute, v. 12, n. 14, p. 2672, 2019.

EPE, E. d. P. E. Anuário estatístico de energia elétrica 2022: Ano base 2021. *Empresa de Pesquisa Energética*, 2022.

EPE, N. T. Análise da inserção da geração solar na matriz elétrica brasileira. *Nota Técnica da EPE, Rio de Janeiro*, p. 25, 2012.

ESRAM, T.; CHAPMAN, P. L. Comparison of photovoltaic array maximum power point tracking techniques. *IEEE Transactions on energy conversion*, IEEE, v. 22, n. 2, p. 439–449, 2007.

FEMIA, N. et al. Optimization of perturb and observe maximum power point tracking method. *IEEE transactions on power electronics*, IEEE, v. 20, n. 4, p. 963–973, 2005.

FILHO, F. D. et al. *Análise de técnicas de controle de Conversores conectados a redes Elétricas*. Dissertação (Mestrado) — Universidade Federal de Pernambuco, 2009.

Günther, K.; Bendrat, F.; Sourkounis, C. Analysis of optimization strategies for grid-side converter control during grid faults using DSRF control. p. 1–6, 2019.

GOMES, C. P. Energia solar: Utilização como fonte de energia alternativa. *Bolsista de Valor: Revista de divulgação do Projeto Universidade Petrobras e IF Fluminense*, v. 2, n. 1, p. 159–163, 2012.

GREEN, M. A. Silicon photovoltaic modules: a brief history of the first 50 years. *Progress in Photovoltaics: Research and applications*, Wiley Online Library, v. 13, n. 5, p. 447–455, 2005.

HACHIM, B.; DAHLIOUI, D.; BARHDADI, A. Electrification of rural and arid areas by solar energy applications. p. 1–4, 2018.

HASHMI, M. U. et al. Arbitrage with power factor correction using energy storage. *IEEE Transactions on Power Systems*, v. 35, n. 4, p. 2693–2703, 2020.

HUA, C.; SHEN, C. Comparative study of peak power tracking techniques for solar storage system. In: IEEE. *APEC'98 Thirteenth Annual Applied Power Electronics Conference and Exposition.* [S.l.], 1998. v. 2, p. 679–685.

JAIN, C.; SINGH, B. An adjustable dc link voltage-based control of multifunctional grid interfaced solar pv system. *IEEE Journal of Emerging and Selected Topics in Power Electronics*, v. 5, n. 2, p. 651–660, 2017.

JIA, L. et al. A perspective on solar energy-powered road and rail transportation in china. *CSEE Journal of Power and Energy Systems*, v. 6, n. 4, p. 760–771, 2020.

Kandpal, M.; Hussain, I.; Singh, B. Grid integration of solar PV generating system using three-level voltage source converter. p. 1–6, 2015.

KANG, B.-J.; LIAW, C.-M. A robust hysteresis current-controlled pwm inverter for linear pmsm driven magnetic suspended positioning system. *IEEE Transactions on Industrial Electronics*, v. 48, n. 5, p. 956–967, 2001.

KATIRAEI, F.; IRAVANI, M. R.; LEHN, P. W. Micro-grid autonomous operation during and subsequent to islanding process. *IEEE Transactions on power delivery*, IEEE, v. 20, n. 1, p. 248–257, 2005.

Khan, H. et al. An integrated controller to perform LVRT operation in PV systems connected to a LV grid during balanced and unbalanced faults. p. 2002–2007, 2017.

KHAN, H. et al. Reliable and effective ride-through controller operation for smart pv systems connected to lv distribution grid under abnormal voltages. *IEEE Journal of Emerging and Selected Topics in Power Electronics*, v. 8, n. 3, p. 2371–2384, 2020.

KJAER, S. B.; PEDERSEN, J. K.; BLAABJERG, F. Power inverter topologies for photovoltaic modules-a review. In: IEEE. *Conference Record of the 2002 IEEE Industry Applications Conference. 37th IAS Annual Meeting (Cat. No. 02CH37344).* [S.l.], 2002. v. 2, p. 782–788.

KOURO, S. et al. Npc multilevel multistring topology for large scale grid connected photovoltaic systems. In: *The 2nd International Symposium on Power Electronics for Distributed Generation Systems.* [S.l.: s.n.], 2010. p. 400–405.

_____. Model predictive control—a simple and powerful method to control power converters. *IEEE Transactions on Industrial Electronics*, v. 56, n. 6, p. 1826–1838, 2009.

KUCEVIC, D. et al. Standard battery energy storage system profiles: Analysis of various applications for stationary energy storage systems using a holistic simulation framework. *Journal of Energy Storage*, Elsevier, v. 28, p. 101077, 2020.

Li-Jun, J. et al. Unbalanced control of grid-side converter based on dsogi-pll. p. 1145–1149, 2015.

Lin, X. et al. Low-voltage ride-through techniques for two-stage photovoltaic system under unbalanced grid voltage sag conditions. p. 1–8, 2018.

LIU, X.; WANG, P.; LOH, P. C. A hybrid ac/dc microgrid and its coordination control. *IEEE Transactions on smart grid*, IEEE, v. 2, n. 2, p. 278–286, 2011.

MALINOWSKI, M.; JASINSKI, M.; KAZMIERKOWSKI, M. Simple direct power control of three-phase pwm rectifier using space-vector modulation (dpc-svm). *IEEE Transactions on Industrial Electronics*, v. 51, n. 2, p. 447–454, 2004.

MALVINO, A.; BATES, D. J. *Eletrônica*. 8th. ed. [S.l.]: AMGH, 2016. v. 1st.

MARQUES, A. E. B.; CRUZ, E. C. A.; JÚNIOR, S. C. *Dispositivos semicondutores: diodos e transistores*. 13th. ed. Sao Paulo: Érica, 2012.

MARTINS, F. R. et al. Atlas brasileiro de energia solar. INPE, São José dos Campos, n. 2, 2017.

MERAI, M. et al. Fpga-based fault-tolerant space vector-hysteresis current control for three-phase grid-connected converter. *IEEE Transactions on Industrial Electronics*, v. 63, n. 11, p. 7008–7017, 2016.

MIRET, J. et al. Control scheme for photovoltaic three-phase inverters to minimize peak currents during unbalanced grid-voltage sags. *IEEE Transactions on Power Electronics*, v. 27, n. 10, p. 4262–4271, 2012.

MUKUND, P. *Wind and solar power systems*. 1999.

NAHVI, M.; EDMINISTER, J. A. *Circuitos Elétricos-5*. [S.l.]: Bookman Editora, 2014.

NILSSON, J. W.; RIEDEL, S. A. *Electric Circuits*. 8th edition. ed. [S.l.]: Pearson Prentice Hall, 2008.

NOGUCHI, T. et al. Direct power control of pwm converter without power-source voltage sensors. *IEEE Transactions on Industry Applications*, v. 34, n. 3, p. 473–479, 1998.

NREL, N. R. E. L. *Best Research-Cell Efficiency Chart*. 2022. Urlhttps://www.nrel.gov/pv/cell-efficiency.html.

OLIVEIRA, P. A. d. *Controle preditivo baseado em modelo aplicado a conversor multinível ponte-h em cascata com estabilização das tensões nos barramentos cc*. 76 p. Dissertação (Mestrado) — Universidade Federal de Itajubá, Itajubá, 2019.

PARVEZ, M. et al. Current control techniques for three-phase grid interconnection of renewable power generation systems: A review. *Solar Energy*, Elsevier, v. 135, p. 29–42, 2016.

PATEL, H.; AGARWAL, V. Matlab-based modeling to study the effects of partial shading on pv array characteristics. *IEEE Transactions on Energy Conversion*, v. 23, n. 1, p. 302–310, 2008.

PEREIRA, G. M. d. S. *Alocação de bancos de capacitores e reguladores de tensão em redes elétricas inteligentes desbalanceadas*. Dissertação (Mestrado) — Universidade Federal do Paraná, 2015.

PERLIN, J. *Silicon solar cell turns 50*. [S.l.], 2004.

PINHO, J. T.; GALDINO, M. A. et al. Manual de engenharia para sistemas fotovoltaicos. *CRESESB*, Rio de Janeiro, v. 1, 2014.

RAHIM, N. A.; SELVARAJ, J.; KRISMADINATA. Hysteresis current control and sensorless mppt for grid-connected photovoltaic systems. In: *2007 IEEE International Symposium on Industrial Electronics*. [S.l.: s.n.], 2007. p. 572–577.

RAUSCHENBACH, H. *Solar cell array design handbook*. Pasadena, California: [s.n.], 1980. v. 1.

REN21. Renewables 2020 global status report. *Paris: REN21 Secretariat*, 2020.

ROCHA, T. d. O. A. Contribuições para estratégia de controle aplicada à geração fotovoltaica interconectada à rede elétrica. Universidade Federal do Rio Grande do Norte, 2015.

RODRíGUEZ, P. et al. A stationary reference frame grid synchronization system for three-phase grid-connected power converters under adverse grid conditions. *IEEE Transactions on Power Electronics*, v. 27, n. 1, p. 99–112, 2012.

RODRIGUEZ, J. et al. Predictive current control of a voltage source inverter. In: *2004 IEEE 35th Annual Power Electronics Specialists Conference (IEEE Cat. No.04CH37551)*. [S.l.: s.n.], 2004. v. 3, p. 2192–2196 Vol.3.

RODRÍGUEZ, P. et al. Decoupled double synchronous reference frame pll for power converters control. *IEEE Transactions on Power Electronics*, IEEE, v. 22, n. 2, p. 584–592, 2007.

RODRIGUEZ, P. et al. New positive-sequence voltage detector for grid synchronization of power converters under faulty grid conditions. In: IEEE. *2006 37th IEEE Power Electronics Specialists Conference*. [S.l.], 2006. p. 1–7.

SAMPAIO, P. G. V.; GONZÁLEZ, M. O. A. Photovoltaic solar energy: Conceptual framework. *Renewable and Sustainable Energy Reviews*, Elsevier, v. 74, p. 590–601, 2017.

SEDRA, A. S.; SMITH, K. C. *Microelectronic Circuits*. 7th. ed. [S.l.]: Oxford University Press, 2015.

SEN, B.; SHARMA, D.; BABU, B. C. Dsrf and sogi based pll-two viable scheme for grid synchronization of dg systems during grid abnormalities. In: *2012 Students Conference on Engineering and Systems*. [S.l.: s.n.], 2012. p. 1–6.

SILVEIRA, S. de C. et al. Modelos não lineares ajustados à produção acumulada de biogás provenientes de camas sobrepostas de suínos. *Revista Agrogeoambiental*, v. 10, n. 3, 2018.

SOLAR, E. Princípios e aplicações. *Centro de Referencia para Energia Solar e Eólica Sergio de Salvo Brito–CRESESB, Rio de Janeiro. Disponível em:< http://www. cresesb. cepel. br/tutorial/tutorial_solar_2006. pdf*, v. 4, 2006.

SONG, H.-S.; NAM, K. Dual current control scheme for pwm converter under unbalanced input voltage conditions. *IEEE Transactions on Industrial Electronics*, v. 46, n. 5, p. 953–959, 1999.

SUBUDHI, B.; PRADHAN, R. A comparative study on maximum power point tracking techniques for photovoltaic power systems. *IEEE transactions on Sustainable Energy*, IEEE, v. 4, n. 1, p. 89–98, 2012.

SUUL, J. A. et al. Synchronous reference frame hysteresis current control for grid converter applications. *IEEE Transactions on Industry Applications*, v. 47, n. 5, p. 2183–2194, 2011.

TEODORESCU, R.; LISERRE, M.; RODRIGUEZ, P. *Grid converters for photovoltaic and wind power systems.* [S.l.]: John Wiley & Sons, 2011. v. 29.

TEODORO, R. G. *Metodologia para compensação de desequilíbrio em redes elétricas.* Dissertação (Mestrado) — Faculdade de Engenharia de Ilha Solteira, Universidade Estadual Paulista, 2005.

TIMBUS, A. et al. Synchronization methods for three phase distributed power generation systems - an overview and evaluation. In: *2005 IEEE 36th Power Electronics Specialists Conference.* [S.l.: s.n.], 2005. p. 2474–2481.

VALLÊRA, A. M.; BRITO, M. C. Meio século de história fotovoltaica. *Gazeta de Física*, v. 1, n. 2, p. 17, 2006.

VAZQUEZ, S. et al. Model predictive control for power converters and drives: Advances and trends. *IEEE Transactions on Industrial Electronics*, v. 64, n. 2, p. 935–947, 2017.

VERMA, D. et al. Maximum power point tracking (mppt) techniques: Recapitulation in solar photovoltaic systems. *Renewable and Sustainable Energy Reviews*, Elsevier, v. 54, p. 1018–1034, 2016.

Villalva, M. G.; Gazoli, J. R.; Filho, E. R. Comprehensive approach to modeling and simulation of photovoltaic arrays. *IEEE Transactions on Power Electronics*, v. 24, n. 5, p. 1198–1208, 2009.

WIJNHOVEN, T.; DECONINCK, G. Flexible fault current contribution with inverter interfaced distributed generation. In: *2013 IEEE Power & Energy Society General Meeting.* [S.l.: s.n.], 2013. p. 1–5.

XIAO, W.; DUNFORD, W. G.; CAPEL, A. A novel modeling method for photovoltaic cells. In: IEEE. *2004 IEEE 35th Annual Power Electronics Specialists Conference (IEEE Cat. No. 04CH37551).* [S.l.], 2004. v. 3, p. 1950–1956.

YANG, Y. et al. A hybrid power control concept for pv inverters with reduced thermal loading. *IEEE Transactions on Power Electronics*, v. 29, n. 12, p. 6271–6275, 2014.

YU, Y.; HU, X. Active disturbance rejection control strategy for grid-connected photovoltaic inverter based on virtual synchronous generator. *IEEE Access*, v. 7, p. 17328–17336, 2019.

ZANCHETTA, P. et al. Finite states model predictive control for shunt active filters. In: *IECON 2011 - 37th Annual Conference of the IEEE Industrial Electronics Society.* [S.l.: s.n.], 2011. p. 581–586.

ZAPATA, J. W. et al. Analysis of partial power dc–dc converters for two-stage photovoltaic systems. *IEEE Journal of Emerging and Selected Topics in Power Electronics*, v. 7, n. 1, p. 591–603, 2019.

ZILLES, R. et al. *Sistemas fotovoltaicos conectados à rede elétrica.* São Paulo: Oficina de textos, 2012.